Optimized Variable Flip Angle Methods for Single Pool MRI Relaxometry

Azeredo Gomes Teixeira, Rui Pedro

Awarding institution:
King's College London

Optimized Variable Flip Angle Methods for Single Pool MRI Relaxometry

Rui Pedro A. G. Teixeira

A thesis submitted in partial fulfilment of the requirement for the degree of
Doctor of Philosophy of **King's College London**

August 2017

Department of Biomedical Engineering
King's College London

KING'S College LONDON

Abstract

Magnetic Resonance Imaging (MRI) is routinely used as a highly, soft-tissue sensitive qualitative modality. Thus, although widely used as a first line of investigation for both radiological diagnosis and treatment monitoring of neurological disease, almost all assessments are based on images presented in arbitrary units. With this in mind, there is a growing interest in quantitative MRI as a potential route to less subjective diagnosis and to allow cross site comparison studies. Key MR parameters are the proton density M0 and relaxation times T1 and T2 which are strongly associated with tissue integrity. This absolute tissue specific measurements, are expected to overcome inter-site bias in multi-centre studies as opposed to conventional M0, T1 and T2 weighted images whose use is still controversial.

Unfortunately, gold standard methods for estimating relaxation times are two dimensional acquisitions based on spin-echo processes which require long acquisition times. On the contrary, many gradient echo techniques, such as Variable Flip Angle (VFA), Driven Equilibrium Single Pulse Observation of T1/2 (DESPOT), Muti-Parametric Mapping(MPM), etc, have been developed to infer tissue MR properties in clinically feasible times. However, a consensus regarding the accuracy of each method has still to be found. One possible source for the reported discrepancies between methods, is the fact that, in biological samples, a process called Magnetization Transfer (MT) is known to influence the observed relaxometry measurements. To characterize tissue more fully, so called multiple-pool models have been suggested. Current clinical protocols for quantitative imaging generally fail to take MT correctly into account, and therefore produce variable results that undermine their utility as secure diagnostic methods. Quantitative MT protocols can more precisely characterise tissue, but require more data to be collected so are not regarded as clinically feasible.

The work here presented, built on single-compartment DESPOT relaxometry approach and sought to increase its precision of by two means: (i) a joint system relaxometry (JSR) approach that estimates parameters in a single step

using all available data; and (ii) optimizing acquisition parameters by deploying a robust design tool based on the Crámer-Rao lower bound (CRLB). Once this was achieved, the absolute accuracy of gradient echo methods was explored by exploring the influence of magnetization transfer effects on single-pool assumptions. It was then hypothesised that robust relaxometry methods can be achieved by ensuring Constant Saturation of Magnetization Transfer (CSMT) effects. This was demonstrated both numerically and experimentally.

Acknowledgements

The development of the work here presented would not be possible without the immeasurable support of friends, colleagues and family. I am specially thankful to both my supervisors, Professor Jo Hajnal and Shaihan Malik whose guidance and discussions were crucial in the work development. I will always cherish the support they have provided and hope, to some day be able to inspire someone with the same love for the scientific process as they have done to me.

I also immensely cherish the support obtained from everyone in the Centre for the Developing Brain where the presence of such a wide range of background and knowledge allows it to be a pristine place for scientific development. More specifically I'll always remember the coffee-break discussions with Francesco Padormo, Arian Beqiri, Giulio Ferrazi and Prachi Patkee. A big thanks must also be given to both Ana Baburamani and Regina Vontell for our extremely fun and exciting phantom building session at the biology lab.

Family support is one of the most valuable feelings someone may ever experience. The knowledge that there's always someone who believes in you was one of the main drivers throughout the development of this project. with this in mind I must gratefully acknowledge my Mom, Dad and Brother for all the support throughout the years.

Finally but not least, the person who put up with long scanning weekends, long nights and most of all supported me without question in the moments where it was most needed. Vasiliki Chatzi (FHW) this thesis is as much mine as it is yours and I believe that says it all. Thank you!

Contents

List of Figures

List of Tables

Chapter 1

Introduction

Magnetic Resonance Imaging (MRI) is nowadays used as a clinical tool to assess information regarding neurological health. In this context, the ability to probe tissue specific relaxation times T_1 and T_2 has proven to be useful in detecting and understanding diseases [1, 2]. Unfortunately, "gold standard" methods for estimating relaxation times are two dimensional acquisitions based on spin-echo processes which require long acquisition times hindering their application in a clinical setting. On the contrary, gradient echo methods such as the Variable Flip Angle [3] method, DESPOT1/2 [4] or even quantitative multi-parametric mapping approach [5] were previously shown to access high-resolution 3D maps of the human brain in clinically feasible times . However, they've been reported to produce a systematic offset when compared to gold-standard methods and a common ground between both has still to be found [6]. One possible explanation for the reported variations is the multi-compartment nature of biological samples. To counteract this, multiple-pool methods such as quantitative Magnetization Transfer imaging (qMT) [7] or multi-compartment DESPOT (mcDESPOT) [8] have been proposed. Multi-compartment approaches although appealing, require an increased amount of sampled data which hinders their clinical applicability. Also, the required signal to noise ratio to achieve acceptable precision of estimated parameters has been shown to be infeasible in a routine MRI setting [9]. In fact, this has been corroborated in work developed prior to the one reported in this thesis [10], where the stability of mcDESPOT approach was explored and agreement with the findings presented in [9] was found. This instability of multi-compartment methods, motivated the focus in single compartment methodology and within this work, optimization of such methods is sought for brain imaging as maximizing the amount of information obtained per unit time is crucial to promote the clinical applicability of such methods.

With this in mind, this thesis starts by describing, in Chapter 2, the basic MRI concepts necessary to understand the work presented. Building on those concepts, Chapter 3 focuses on the discussion of some of the commonly used relaxometry methods, and their potential sources of bias, which are routinely applied throughout the scientific community. In Chapter 4 a robust framework based on the Crámer Rao Lower Bound (CRLB) is proposed in order to select, given a selected relaxometry approach, which measurements allow minimal estimation variance to be achieved given a fixed time constraint. This optimization approach is furthermore applied in Chapter 5 where a Joint System Relaxometry (JSR) approach is proposed to maximize the amount of information per unit time by combining different image modalities into a single estimation framework. This work has in fact been subject to peer-review and can be found in [11]. Chapter 6 addresses the issue of systematic variations observed in different relaxometry strategies. We attribute the observed deviations to magnetization transfer effects and reflect upon the consequences of assuming a single source of magnetization inside each voxel when a binary spin system is present. It then proposes a signal excitation scheme based on non-selective multi-band pulses that induce Constant Saturation of Magnetization Transfer (CSMT) throughout all measurements in order to minimise this source of error.

1.1 Scientific Contributions

Although this thesis focus on the optimization of variable flip angle relaxometry methods, throughout the three years that lead to the development of this work, collaboration with external projects (which although not necessarily relevant) allowed my development as an MRI scientist and contributed in a direct or indirect way towards the completion of this project. Therefore, a list of scientific contributions that were developed throughout the duration of this project is presented.

1.1.1 Journal Papers

1. **Joint System Relaxometry (JSR) and Crmer-Rao Lower Bound optimisation of sequence parameters: a framework for enhanced precision of DESPOT T1 and T2 Estimation** A. G. Teixeira, R. P., J. Malik, S., V. Hajnal, J. 13 Feb 2017 In: Magnetic resonance in medicine : official journal of the Society of Magnetic Resonance in Medicine / Society of Magnetic Resonance in Medicine;

2. **Sensitivity encoding for aligned multishot magnetic resonance reconstruction** Cordero-Grande, L., A. G. Teixeira, R. P., Hughes, E. J., Hutter, J., Price, A. N., Hajnal, J. V. Sep 2016 In : IEEE Transactions on Computational Imaging. 2, 3, p. 266-280;

3. **A dedicated neonatal brain imaging system** Hughes, E. J., Winchman, T., Padormo, F., Teixeira, R., Wurie, J., Sharma, M., Fox, M., Hutter, J., Cordero-Grande, L., Price, A. N., Allsop, J., Bueno-Conde, J., Tusor, N., Arichi, T., Edwards, A. D., Rutherford, M. A., Counsell, S. J., Hajnal, J. V. 19 Sep 2016 In : Magnetic resonance in medicine : official journal of the Society of Magnetic Resonance in Medicine / Society of Magnetic Resonance in Medicine;

1.1.2 Conference Papers

1. A. G. Teixeira, R.P., J. Malik, S., V. Hajnal, J., **Optimizing single component DESPOT using a Cramer-Rao Lower Bound framework**. in Proc Int Soc Magn Reson Med (ISMRM), Milan, Italy, 2014;

2. A. G. Teixeira, R.P., J. Malik, S., V. Hajnal, J., **Explicit Modeling of SPGR signals using Extended Phase Graphs in DESPOT style Relaxometry - A Dictionary Approach**. in Proc Int Soc Magn Reson Med (ISMRM), Toronto, Canada, 2015;

3. Hutter, J., Tournier, J., Hughes, E., N. Price, A., Cordero-Grande, L., G. Nunes, R., A. G. Teixeira, R.P., J. Counsell, S., L. R. Andersson, J., Rueckert, D., Edwards, A. D., V. Hajnal, J., **Optimized Multi-Shell HARDI Acquisition with Alternating Phase Encoding Directions for Neonatal DMRI**. in Proc Int Soc Magn Reson Med (ISMRM), Toronto, Canada, 2015;

4. Cordero-Grande, L., Hughes, E., A. G. Teixeira, R.P., V. Hajnal, J., **Parallel Imaging for Motion Correction in Neonatal Brain MR Reconstruction**. in Proc Int Soc Magn Reson Med (ISMRM), Toronto, Canada, 2015;

5. A. G. Teixeira, R. P., Kelly, C., Arichi, T., J. Malik, S., Counsell, S., V. Hajnal, J., **Optimizing SWI in Neonates**. in Proc Int Soc Magn Reson Med (ISMRM), Singapore, 2016;

6. N. Price, A., J. Malik, S., Hutter, J., Buhrer, M., Cordero-Grande, L., A. G. Teixeira, R. P., J. Hughes, E., A. Rutherford, M., V. Hajnal, J., **Multiband TSE Imaging of the Fetal Brain at 3T**. in Proc Int Soc Magn Reson Med (ISMRM), Singapore, 2016;

7. Ferrazzi, G., A. G. Teixeira, R.P., Hutter, J., Cordero-Grande, L., Hughes, E., N. Price, A., V. Hajnal, J., **Revisited Multislice Distributed Inversion Recovery Towards an Efficient Neonatal MR Examination**. in Proc Int Soc Magn Reson Med (ISMRM), Singapore, 2016;

8. Tournier, J., A. G. Teixeira, R.P., Murgasova, M., Edwards, A.D., V. Hajnal, J., J. Counsell, S., **A Simple Method for Myelin Mapping Using T1-Weighted, T2-Weighted and PD-Weighted Images**. in Proc Int Soc Magn Reson Med (ISMRM), Singapore, 2016;

9. A. G. Teixeira, R.P., N. Price, A., A. Baburamani, A., J. Malik, S., V. Hajnal, J., **Robust VFA relaxometry by Continuous Saturation of Magnetization Transfer (CSMT) effects with Non-selective Multi-Band pulses**. in Proc Int Soc Magn Reson Med (ISMRM), Honolulu, Hawaii, 2016;

10. Ferrazzi, G., N. Price, A., A. G. Teixeira, R. P., Padormo, F., Cordero-Grande, L., Hughes, E., McCabe, L., Rutherford, M., Murgasova, M., V. Hajnal, J., **An optimised 2D MPRAGE sequence for T1 contrast in the fetal brain: application to slice to volume reconstruction and multi-band acceleration**. in Proc Int Soc Magn Reson Med (ISMRM), Honolulu, Hawaii, 2016;

11. Cordero-Grande, L., Ferrazzi, G., A. G. Teixeira, R.P., Shahzad, H., N. Price, A., V. Hajnal, J., **Motion correction in volumetric brain imaging based on DISORDER: Distributed and Incoherent Sample Orders for Reconstruction Disentanglement using Encoding Redundancy**. in Proc Int Soc Magn Reson Med (ISMRM), Honolulu, Hawaii, 2016;

12. Hutter, J., J. Slator, P., O'Muircheartaigh, J., A. G. Teixeira, R.P., N. Price, A., D. S. Gomes, A., McCabe, L., Arulkumaran, S., Rutherford, M., V. Hajnal, J., **An exploration of quantitative physiological multi-modal in-vivo imaging of the human placenta**. in Proc Int Soc Magn Reson Med (ISMRM), Honolulu, Hawaii, 2016;

13. S. Santos, N., A. G. Teixeira, R.P., V. Hajnal, J., G. Nunes, R., **Assessing the Accuracy of T2 and B1+ Maps Estimated from Multi-echo Spin Echo MRI Sequences Using Extended Phase Graph Signal Predictions**. in Proc Int Soc Magn Reson Med (ISMRM), Honolulu, Hawaii, 2016;

14. Chatzi, V., A. G. Teixeira, R.P., Tournier, J., **A multivariate machine learning framework for psychosis: integrating diffusion and structural MRI**. in Proc Int Soc Magn Reson Med (ISMRM), Honolulu, Hawaii, 2016;

Chapter 2

Background

This chapter, aims to present a brief summary of the basic magnetic resonance imaging (MRI) physical principles, necessary to understand the work presented throughout this thesis.

According to [12] the idea of using spatial varying magnetic fields in order to obtain information about a given object was first proposed and demonstrated by Lauterbur and Mansfield in 1973 in what may be considered as the birth of MRI. Due to its non-ionizing nature and excellent soft tissue contrast, MRI quickly transformed into a technique which is currently widely used in Hospital environment.

2.1 Basic Principles of MRI

The fundamental principals of MRI are based on the interaction between atomic nuclei (typically protons) and external magnetic fields. In spite of its quantum nature [13, 14], the nuclear resonance problem can be mostly explained from a classical perspective. This description, dwells with the evolution of a single proton aligned with a main magnetic field $\vec{B}$ throughout the duration of the experiment. When in the presence of such a field, generated torques tend to align protons with the field direction. Depending on the proton's intrinsic spin, the resulting alignment will be either along the parallel direction (low energy state) or the anti-parallel direction (high-energy state) (Figure 2.1) [15]. The resulting net magnetic moment is defined as the magnetization which can be quantified as having a magnitude and a direction it is, therefore, best described by a vector $\vec{M}$. Its rate of change over time (time derivative) due to an external field is proportional to

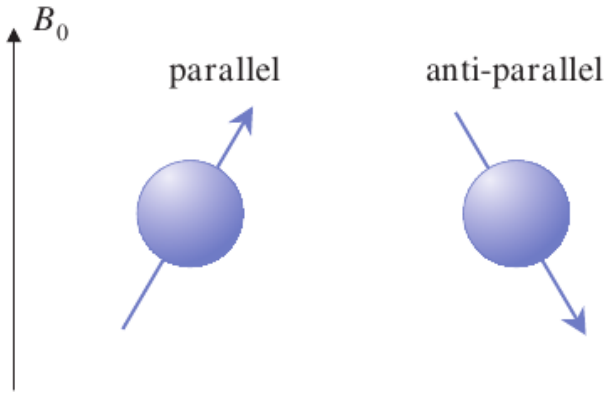

Figure 2.1: Graphical representation of the two possible orientations for a proton when subjected to an external magnetic field. Adapted from [15]

the gyromagnetic ratio constant γ ($2\pi 42.6 \times 10^6\ rad.s^{-1}T^{-1}$) and is always perpendicular to both $\vec{M}$ and $\vec{B}$ being described by the well known Bloch Equation (Equation 2.1) [12, 16]

$$\frac{d\vec{M}}{dt} = \gamma(\vec{M} \times \vec{B}). \tag{2.1}$$

Note that the external magnetic field seen by $\vec{M}$ includes the superposition of the desired main magnetic field in the z direction $\vec{B_0}$, local field inhomogeneities $\delta\vec{B_0}$, an external excitation field $\vec{B_1}$ and imaging gradients that are a linear function of space $\vec{G} \cdot \vec{r}$ such that [16]

$$\left(\frac{d\vec{M}}{dt}\right)_{B_0} + \left(\frac{d\vec{M}}{dt}\right)_{\delta\vec{B_0},\vec{B_1},\vec{G}\cdot\vec{r}} = \gamma\{\vec{M} \times [\vec{B_0} + \delta\vec{B_0} + \vec{B_1} + \vec{G} \cdot \vec{r}]\}. \tag{2.2}$$

Ignoring all contribution external to $\vec{B_0}$ would result in a precession of $\vec{M}$ around the main field with angular velocity given by the Larmor Equation $\omega_0 = \gamma|\vec{B_0}|$. If we position ourselves in a rotation frame of reference that oscillates at ω_0 Equation 2.2 will simplify to

$$\left(\frac{d\vec{M}}{dt}\right)_{\delta\vec{B_0},\vec{B_1},\vec{G}\cdot\vec{r}} = \gamma\{\vec{M} \times [\delta\vec{B_0} + \vec{B_1} + \vec{G} \cdot \vec{r}]\} \tag{2.3}$$

which, if we assume a perfect homogeneous main field ($\delta\vec{B_0} = 0$), will have the matrix representation

$$\left(\frac{d\vec{M}}{dt}\right)_{\vec{B_1},\vec{G}\cdot\vec{r}} = \begin{bmatrix} 0 & \gamma\vec{G}\cdot\vec{r} & -\gamma B_{1,y} \\ -\gamma\vec{G}\cdot\vec{r} & 0 & \gamma B_{1,x} \\ \gamma B_{1,y} & -\gamma B_{1,x} & 0 \end{bmatrix} \begin{bmatrix} M_x \\ M_y \\ M_z \end{bmatrix}. \tag{2.4}$$

At equilibrium no transverse magnetization exists ($M = [M_x, M_y, M_z] = [0, 0, M_0]$), therefore, if no $\vec{B_1}$ is applied no motion is induced in the system.

2.1.1 Excitation Pulse

Building from Equation 2.4 it can be seen that through interaction with an applied excitation field $\vec{B_1}$ (also known as RF pulse) it is possible to disturb the equilibrium magnetization. The simplest case can be derived for non selective excitations under which no imaging gradients are applied. Considering a RF pulse with constant amplitude $\omega_1(rad.s^{-1})$, such that $\omega_1 = 2\pi\gamma\vec{B_1}(t)$, and duration $t(s)$ applied along the x direction (Figure 2.2) Equation 2.4 becomes

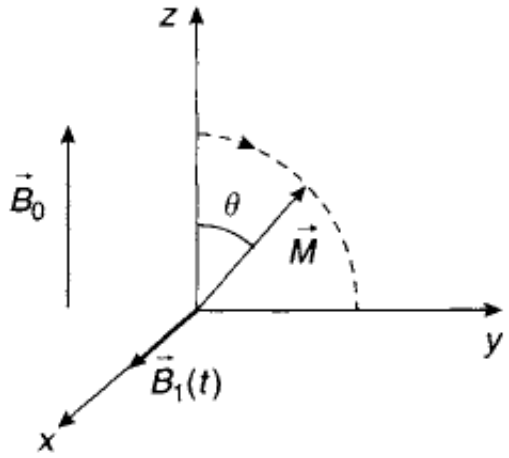

Figure 2.2: Representation of an excitation pulse in the rotating reference frame. The magnetization vector M is initially aligned with B_0 ($M = [M_x, M_y, M_z] = [0, 0, M_0]$). An RF excitation pulse $B_1(t)$ is applied along the x axis resulting in the rotation in the yz plane by the flip angle θ. [17]

$$\left(\frac{d\vec{M}(t)}{dt}\right)_{\vec{B_1}} = \begin{bmatrix} 0 & 0 & 0 \\ 0 & 0 & \gamma B_{1,x} \\ 0 & -\gamma B_{1,x} & 0 \end{bmatrix} \begin{bmatrix} M_x(t) \\ M_y(t) \\ M_z(t) \end{bmatrix} \tag{2.5}$$

whose solution for Equation 2.5 can be easily found to be

$$\begin{bmatrix} M_x(t) \\ M_y(t) \\ M_z(t) \end{bmatrix} = \begin{bmatrix} 1 & 0 & 0 \\ 0 & \cos\omega_1 t & \sin\omega_1 t \\ 0 & -\sin\omega_1 t & \cos\omega_1 t \end{bmatrix} \begin{bmatrix} M_x^0 \\ M_y^0 \\ M_z^0 \end{bmatrix} \equiv \vec{M}(t) = \vec{R}(\theta = \omega_1 t)\vec{M}(t = 0). \tag{2.6}$$

Equation 2.6 shows a very powerful property of the excitation on the magnetization. The magnetization vector after the RF pulse M^+ is the magnetization prior to the pulse M^- rotated by a flip angle $\theta = \omega_1 t$ (Figure 2.2). The same reasoning

can be applied to slice selective excitations, however $\vec{G} \cdot \vec{r}$ needs to be considered. Throughout this work only non-selective excitations were used and further discussion is out of the scope of this thesis.

The most common flip pulses are the $\theta = \pi/2$ pulse and the $\theta = \pi$ pulse that are responsible for flipping the magnetization vector by respectively 90^{o} and 180° from their initial state. The following section will describe how the magnetization is expected to evolve after it has been subject to rotation during the so called "free precession".

2.1.2 Imaging Gradients and Relaxation

After the magnetization has been perturbed from equilibrium it is usually subject to the influence of imaging gradients that allow the sampling of the object of interest. Therefore it is important to understand how the magnetization evolves due to presence of this gradients. Building from Equation 2.4 assuming $\vec{B}_1(t) = 0$ we have

$$\left(\frac{d\vec{M}(t)}{dt}\right)_{\vec{G}\cdot\vec{r}} = \begin{bmatrix} 0 & \gamma\vec{G}\cdot\vec{r} & 0 \\ -\gamma\vec{G}\cdot\vec{r} & 0 & 0 \\ 0 & 0 & 0 \end{bmatrix} \begin{bmatrix} M_x(t) \\ M_y(t) \\ M_z(t) \end{bmatrix} \tag{2.7}$$

which, if we make use of the complex notation $M_T(t) = M_x(t) + iM_y(t)$ ($i = \sqrt{-1}$) can be simplified into [12, 16]

$$M_T(t) = M_T(t=0)e^{-i\vec{r}\cdot\int\gamma\vec{G}(t)dt}. \tag{2.8}$$

Setting $\vec{r}$ to be a linear function of z allows us to create a linear space dependent Larmor frequency distribution

$$\omega_G(z,t) = \gamma z G(t) \tag{2.9}$$

for the one dimensional case. The use of a gradient to establish a relation as shown in 2.9, where the position of spins along a known direction results in a specific precessional distribution is referred to as frequency encoding along that direction [12]. For the one dimensional case (1D) Equation 2.9 allows us to measure the signal

$$s(k) = \int \rho(z)e^{-i2\pi\gamma z\int\vec{G}(t)dt}dz. \tag{2.10}$$

where, $\rho(z)$ is the total spin density (proportional to the equilibrium magnetization, it is the concentration of nuclei in tissue processing at the Larmor frequency) and $k : k(t) = \gamma\int_0^t G(t)dt$ is defined as the spatial frequency [12]. Equation 2.10 is one

of the main building blocks of MR imaging reconstruction when linear gradients are applied. The measured signal $s(k)$ is the Fourier transform of the spin density of the sample and as a consequence the spin density can be determined by applying the inverse Fourier transform of the signal $s(k)$ such that [12]

$$\rho(z) = \int s(k)(e)^{+i2\pi kz} dk. \tag{2.11}$$

Note that imaging gradients have no effect on the M_z component of the magnetization.

This however, is not a full description of the magnetization behaviour. If no extra terms were considered the magnetization would continue its precession after excitation *ad eternum* and never return to equilibrium. To take this into account it must be considered that at the microscopic level, spin-spin interactions cause the transverse magnetization to slowly degrade over time. This is an irreversible destructive process which is approximated by a first order constant rate $R_2 = 1/T_2$. Recovery towards equilibrium is attributed to energy exchanges between spins and their surrounding lattice. This is commonly approximated by a first order recovery rate $R_1 = 1/T_1$. Therefore, Equation 2.7 can be re-written such that

$$\left(\frac{d\vec{M}(t)}{dt}\right)_{\vec{G}\cdot\vec{r}} = \begin{bmatrix} -R_2 & \gamma\vec{G}\cdot\vec{r} & 0 \\ -\gamma\vec{G}\cdot\vec{r} & -R_2 & 0 \\ 0 & 0 & -R_1 \end{bmatrix} \begin{bmatrix} M_x(t) \\ M_y(t) \\ M_z(t) \end{bmatrix} + \begin{bmatrix} 0 \\ 0 \\ M_0R_1 \end{bmatrix}. \tag{2.12}$$

Therefore, using the complex notation we obtain transverse

$$M_T(t) = M_T(0)e^{-i\vec{r}\cdot\int\vec{G}(t)dt}e^{-tR_2} \tag{2.13}$$

and longitudinal magnetization

$$M_z(t) = [M_z(t=0) - M_0]e^{-tR_1} + M_0 \tag{2.14}$$

2.1.3 Spin Echo and Fast Spin Echo Imaging

Following the description of the effects induced on the magnetization from excitation pulses and imaging gradients it is possible to understand one of the most well known imaging acquisitions - The Spin Echo. It's sequence diagram can be found in Figure 2.3. The basic spin echo experiment, first presented in 1950 by E. L. Hahn [18], is performed by applying an excitation $\pi/2$ pulse along the x direction (Figure 2.2) followed by a refocusing π pulse along the y direction separated by a time distance $T_E/2$. This set-up allows an echo formation at a time

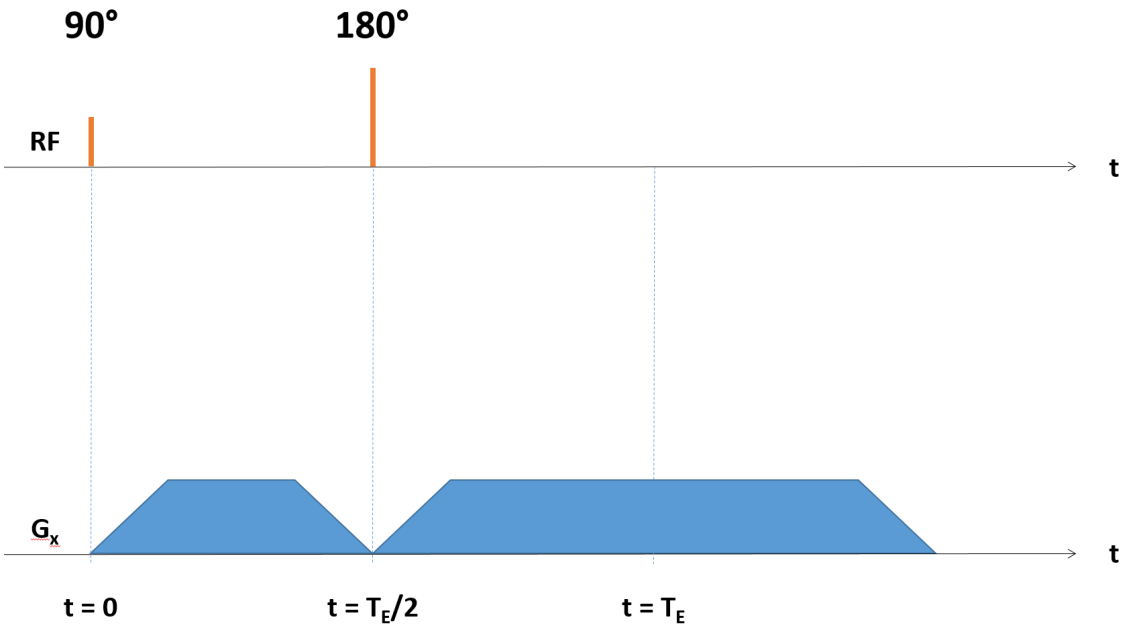

Figure 2.3: Time diagram of 1 dimensional Spin-Echo Sequence

T_E since the rate at which spins accumulate phase is unchanged throughout the experiment. Repetition of this refocusing is possible by continuously applying refocusing pulses separated by a time interval T_E giving origin the the turbo spin echo sequence (TSE). This will force the spin system to keep refocusing until the signal loses coherence due to R_2 decay.

From a more mathematical point of view, in the rotating frame of reference, defining the initial magnetization at equilibrium as $\vec{M}(t = 0^-) = (0, 0, M_0)^T = \vec{M}^-(t = 0)$ we start by applying a $90°$ pulse along the x direction. This induces a rotation towards the y axis and we define the post-pulse magnetization as $\vec{M}^+(t = 0)$. Recalling that the magnetization evolution after excitation is governed by Equations 2.13 and 2.14 we can define the phase evolution of the magnetization between $t = 0$ and $t = T_E/2$ as

$$\phi(t = T_E/2) = \gamma x \int_0^{T_E/2} G_x(t)dt \tag{2.15}$$

and the magnetization immediately prior to the inversion pulse becomes

$$M_T^-(t = T_E/2) = M_T(t = 0)e^{-i\phi(t=T_E/2)}e^{-T_E R_2/2}. \tag{2.16}$$

The $180°$ pulse induces a complete inversion of the dephasing caused by the imaging gradients which can be mathematically expressed as a minus sign in the

magnetization phase

$$M_T^-(t = T_E/2) = M_T(t = 0)e^{i\phi(t=T_E/2)}e^{-T_E R_2/2}. \tag{2.17}$$

With this, all that is necessary to realign the spins and form an echo is to counteract the effect of the first gradient by applying the same level of dephasing such that between $t = T_E/2$ and $t = T_E$ the relationship

$$\phi(t = T_E) = -\gamma x \int_0^{T_E/2} G_x(t)dt + \gamma x \int_{T_E/2}^{T_E} G_x(t)dt = 0 \tag{2.18}$$

holds and the magnetization at $t = T_E$ becomes:

$$M_T(t = T_E) = M_T(t = 0)e^{-T_E R_2} \tag{2.19}$$

$$M_z(t = T_E) = M_0(1 - e^{-T_E R_1}) \tag{2.20}$$

Note that the great strength of this approach is that even if gradient inhomogeneities exist such that $G = G_x + \delta B_0$ they will be refocused at $t = T_E$ as long as the timings are maintained. This refocusing can be repeated as n times by applying refocusing pulses at $t = (2n - 1)T_E/2$ such that:

$$M_T(t = nT_E) = M_T(t = 0)e^{-nT_E/T_2}, n = 1, 2, 3, ..., \infty \tag{2.21}$$

$$M_z(t = nT_E) = M_0(1 - e^{-nT_E/T_1}), n = 1, 2, 3, ..., \infty \tag{2.22}$$

2.1.4 Gradient Echo Imaging

In a gradient echo sequence, after excitation, a set of imaging gradients is applied in order to sample the different spatial dependent frequencies necessary to form an MR image (Figure 2.4). Contrary to the Spin-Echo, the readout gradient only compensates the dephasing that is consequence of the first gradient lobe. Dephasing caused by magnetic field inhomogeneities or spin-spin interactions still cause a gradual signal intensity loss commonly approximated as $R_2^* = R_2 + R_2'$ [15]. On the other hand the lack of the refocusing pulse allows more rapid acquisitions to be performed.

Following the same mathematical description as in the previous section, the evolution of the magnetization as a function of time can be described. Mathematically representing the magnetization phase evolution due to the sequence

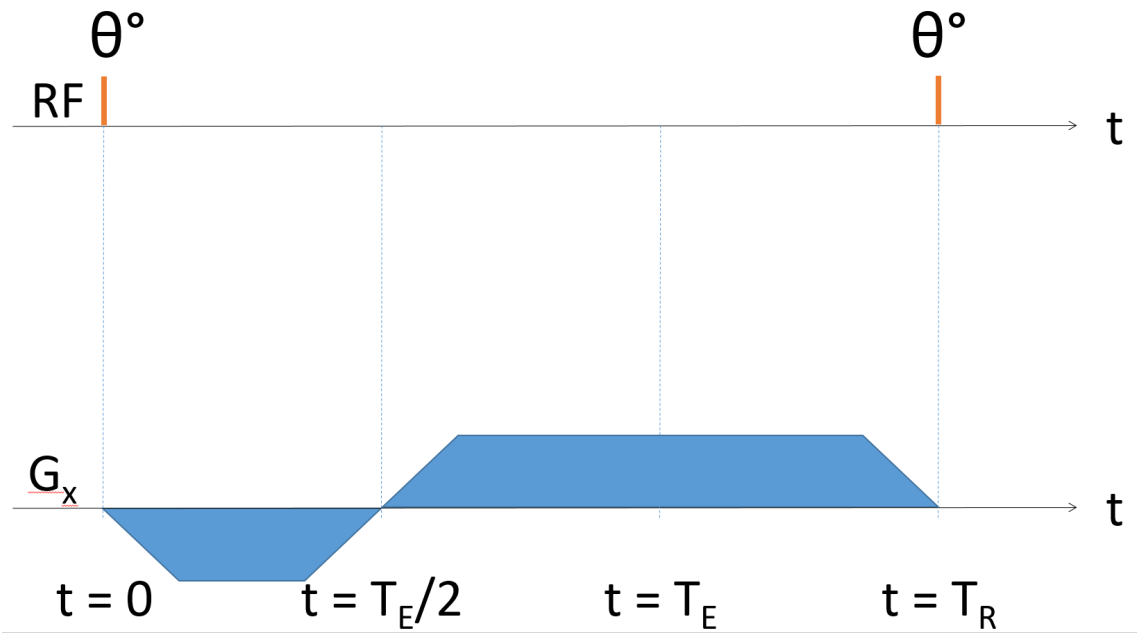

Figure 2.4: Time diagram of 1 dimensional Gradient-Echo Sequence

diagram presented in Figure 2.4:

$$\phi(t = T_E) = -\gamma x \int_0^{T_E/2} G_x(t) + \delta B_0 dt + \gamma x \int_{T_E/2}^{T_E} G_x(t) + \delta B_0 dt \tag{2.23}$$

where, δB_0 is explicitly defined in order to demonstrate that even by planning the readout gradient to rephase the prewinder gradient we have:

$$\phi(t = T_E) = \gamma x \{ \int_0^{T_E/2} \delta B_0 dt + \int_{T_E/2}^{T_E} \delta B_0 dt \} = \phi_{\delta B_0} \tag{2.24}$$

Showing that contrary to the Spin-Echo approach Gradient Echo sequences are modulated by an extra dephasing term due to local field inhomegeneities such that:

$$M_T(t = T_E) = M_T(t = 0) e^{-i\phi_{\delta B_0}(T_E)} e^{-T_E R_2^*} \tag{2.25}$$

2.1.5 Magnetization preparation pulse

Prior to imaging acquisition with either a Spin-Echo or Gradient-Echo method the available magnetization can prepared using a preparation/inversion pulse (typically $180°$ pulse) that perturbs the equilibrium magnetization to induce an extra source of signal contrast. Defining the inversion time T_I as the time between the preparation pulse and the imaging block, and T_R as the time between two consecutive inversion pulses such that $T_R >> 1/R_1$ it can be seen from Equation

2.14 that the available longitudinal magnetization is expected to be:

$$M_z(t = T_I) = [-M_0 - M_0]e^{-T_I R_1} + M_0 = M_0[1 - 2e^{-T_I R_1}] \tag{2.26}$$

The same signal evolution as discussed in the previous two sections is then expected given that the initial state of the magnetization prior to excitation is given by $\vec{M}_z(t = T_I)$.

2.1.6 Rotation Operator Algorithm

The common approach to simulate an MRI experiment makes use of the rotation operator algorithm (ROA) which represents the Bloch equations as rotations of magnetization vectors [19]. This algorithm operates by assuming spin dephasing ϕ as rotations around the z-axis, and excitations produced by RF pulses as rotations around the x-axis with a flip angle θ [19] (Equation 2.6). If one treats RF pulses as acting instantaneously on a magnetization vector (also know as isochromat) $(M_x, M_y, M_z)^T$ then they can be defined as the following rotation matrices:

$$R_x(\theta) = \begin{bmatrix} 1 & 0 & 0 \\ 0 & \cos(\theta) & -\sin(\theta) \\ 0 & \sin(\theta) & \cos(\theta) \end{bmatrix} \tag{2.27}$$

and dephasing ϕ of the isochromat

$$R_z(\phi) = \begin{bmatrix} \cos(\phi) & -\sin(\phi) & 0 \\ \sin(\phi) & \cos(\phi) & 0 \\ 0 & 0 & 1 \end{bmatrix} \tag{2.28}$$

Resulting in the notation for a general RF pulse with azimuthal phase Φ relative to the x-axis

$$R_\Phi(\theta, \Phi) = R_z(\Phi)R_x(\theta)R_z(-\Phi) \tag{2.29}$$

If one is interested in simulating the effect of a MR sequence on an ensemble of spins, making use of this tool requires a sufficient number of isochromats with different dephasing angles ϕ to be simulated in order to obtain a reliable estimation. This means that this approach is well suited to track the time evolution of a small number of isochromats but special care is required to estimate signal intensities, since the later would require the user to take into account a sufficient amount of individual magnetization contributions which will depend on the sequence in question.

2.1.7 Extended Phase Graphs

The Extended Phase Graphs (EPG) approach presents an alternative model that allows a comprehensive explanation of the phenomena occurring in a MRI experiment. Also, it can be used to trace and compute the interaction of spins as they are subject to different RF pulses and dephasing gradients giving an excellent insight of the physical processes present in different MR imaging approaches [20].

During a MRI experiment, field gradients are used to obtain spatial encoding, signal spoiling, motion sensitivity, etc., therefore the spin system is consistently in an incoherent state except when a echo is generated (coherent state). If one uses a rotating frame of reference which is in resonance with the spins precession frequency, and ignoring relaxation effects, the magnetization time evolution due to an applied gradient on a single isochromat which is at an off-center position $\vec{r}$ can be computed by

$$M_x(\vec{r}) = M\cos(\gamma\vec{r}\int_0^t \vec{G}(t')dt') = M\cos(\vec{k}\vec{r}) \tag{2.30}$$

$$M_y(\vec{r}) = M\sin(\gamma\vec{r}\int_0^t \vec{G}(t')dt') = M\sin(\vec{k}\vec{r}) \tag{2.31}$$

where the angular wave vector $\vec{k}(t)$ represents a quantitative measure of dephasing which can, to some extent, be associated with the concept of k-space. In order to avoid the distinction between the x and y components of the magnetization vector a change of basis to the the complex magnetization components is used [19, 21] and therefore following the notation presented in [19]:

$$M_+(\vec{r}) = M_x(\vec{r}) + iM_y(\vec{r}) = Me^{i\phi\vec{r}} = Me^{i\vec{k}\vec{r}} = (M_-)^* \tag{2.32}$$

$$M_-(\vec{r}) = M_x(\vec{r}) - iM_y(\vec{r}) = Me^{-i\phi\vec{r}} = Me^{-i\vec{k}\vec{r}} = (M_+)^* \tag{2.33}$$

Where, "$*$" represents the complex conjugate operation and $i = \sqrt{-1}$ is the imaginary unit from complex algebra. This basis transformation is of high practical value because it simplifies the effect of an $180°$ RF pulse to a complex conjugate operation ($(M_+)^* = M_-$).

So far in this section it has been discussed the magnetization behaviour of isochromats with different frequency offsets along the gradient direction. However, in MRI, one is interested in understanding the total net magnetization which can be obtained by summing the contribution of all the isochromats that have been considered within a volume of interest V. In mathematical terms, assuming

the continuous limit, this can be expressed has an integration over the considered volume:

$$\int_V M_+(\vec{r})e^{-i\vec{k}\vec{r}}d^3r = \tilde{F}_+(\vec{k}) \Leftrightarrow M_+(\vec{r}) = \int_V \tilde{F}_+(\vec{k})e^{i\vec{k}\vec{r}}d^3k \tag{2.34}$$

$$\int_V M_-(\vec{r})e^{-i\vec{k}\vec{r}}d^3r = \tilde{F}_-(\vec{k}) \Leftrightarrow M_-(\vec{r}) = \int_V \tilde{F}_-(\vec{k})e^{i\vec{k}\vec{r}}d^3k \tag{2.35}$$

$$\int_V M_z(\vec{r})e^{-i\vec{k}\vec{r}}d^3r = \tilde{Z}(\vec{k}) \Leftrightarrow M_z(\vec{r}) = \int_V \tilde{Z}(\vec{k})e^{i\vec{k}\vec{r}}d^3k \tag{2.36}$$

Equation 2.34, 2.35 and 2.36 interprets the transverse magnetization as a sum of complex spatial harmonics or "partition states" with wave vectors $\vec{k}$, in other words, $\tilde{F}_+(\vec{k})$ is the Fourier decomposition of the magnetization $M_+(\vec{r})$ [19].

This approach allows efficient description of gradient dephasing in a system of reference. With this, it is possible to keep record of how partition states populations evolve due to their exposure to different gradients. This exposure results in the relationships between the dephasing $\tilde{F}_+(\vec{k})$ and rephasing $\tilde{F}_-(\vec{k})$ states which is a key concept within the EPG framework.

The second key concept present in the EPG calculus is the effect RF pulses have on the partition states. The ROA rotation matrices $R_x(\alpha)$ and $R_z(\phi)$ presented in section 2.1.6 can be transformed to the complex basis by applying the same transformation matrix **S** used to transform the magnetization array $M = [M_x, M_y, M_z]^T$ to the complex domain:

$$\begin{bmatrix} M_+ \\ M_- \\ M_z \end{bmatrix} = \begin{bmatrix} 1 & +i & 0 \\ 1 & -i & 0 \\ 0 & 0 & 1 \end{bmatrix} \begin{bmatrix} M_x \\ M_y \\ M_z \end{bmatrix} = \mathbf{SM} \tag{2.37}$$

Therefore the RF pulse in the new complex basis can be defined as [19, 20]:

$$\mathbf{T}_x(\alpha) = \mathbf{S}\mathbf{R}_x(\alpha)\mathbf{S}^{-1} = \begin{bmatrix} \cos^2(\alpha/2) & \sin^2(\alpha/2) & -i\sin(\alpha) \\ \sin^2(\alpha/2) & \cos^2(\alpha/2) & +i\sin(\alpha) \\ -(i/2)\sin(\alpha) & +(i/2)\sin(\alpha) & \cos(\alpha) \end{bmatrix} \tag{2.38}$$

and the dephasing matrix,

$$\mathbf{T}_z(\phi) = \mathbf{S}\mathbf{R}_z(\phi)\mathbf{S}^{-1} = \begin{bmatrix} e^{i\phi} & 0 & 0 \\ 0 & e^{-i\phi} & 0 \\ 0 & 0 & 1 \end{bmatrix} \tag{2.39}$$

With this in mind a general operator $\mathbf{T}(\alpha, \phi) = \mathbf{T}_z(\phi)\mathbf{T}_x(\alpha)\mathbf{T}_z(-\phi)$ can be defined

as the effect of a RF pulse on the complex magnetization:

$$\begin{bmatrix} M_+ \\ M_- \\ M_z \end{bmatrix}^+ = \mathbf{T}(\alpha,\phi)\mathbf{M}^- \\ = \begin{bmatrix} \cos^2(\alpha/2) & e^{2i\phi}\sin^2(\alpha/2) & -ie^{i\phi}\sin(\alpha) \\ e^{-2i\phi}\sin^2(\alpha/2) & \cos^2(\alpha/2) & +ie^{-i\phi}\sin(\alpha) \\ -(i/2)e^{-i\phi}\sin(\alpha) & +(i/2)e^{i\phi}\sin(\alpha) & \cos(\alpha) \end{bmatrix} \begin{bmatrix} M_+ \\ M_- \\ M_z \end{bmatrix}^- \quad (2.40)$$

Here the $+$ and $-$ as superscripts are used to specify the magnetization "pre" and "post" RF pulse [19, 20] while the subscripts highlight magnetization which is either dephasing $(+)$ or rephasing $(-)$. Equation 2.40 shows the second key concept behind the EPG framework: The RF pulse has the effect of interchanging the population of the dephasing magnetization ($\tilde{F}_+$), rephasing magnetization ($\tilde{F}_-$) and longitudinal magnetization ($\tilde{Z}$) partitions.

By combining the Fourier description of the magnetization (Equations 2.35, 2.34 and 2.36) with the partition "mixing" effect presented in Equation 2.40, the EPG framework that allows the description a group of isochromats as they are affected by applied gradients and RF pulses (including the computation of echo intensities) is presented:

$$\begin{pmatrix} \tilde{F}_{+\vec{k}} \\ \tilde{F}_{-\vec{k}} \\ \tilde{Z}_{\vec{k}} \end{pmatrix}^+ = \\ \begin{pmatrix} \cos^2(\alpha/2) & e^{2i\phi}\sin^2(\alpha/2) & -ie^{i\phi}\sin(\alpha) \\ e^{-2i\phi}\sin^2(\alpha/2) & \cos^2(\alpha/2) & +ie^{-i\phi}\sin(\alpha) \\ -(i/2)e^{-i\phi}\sin(\alpha) & +(i/2)e^{i\phi}\sin(\alpha) & \cos(\alpha) \end{pmatrix} \begin{pmatrix} \tilde{F}_{+\vec{k}} \\ \tilde{F}_{-\vec{k}} \\ \tilde{Z}_{\vec{k}} \end{pmatrix}^- \quad (2.41)$$

Some care must be taken with this newly defined basis and how each state interacts with the other states [20]. As a first instance, it must be guaranteed that the total amount of magnetization is conserved - $M_x^2 + M_y^2 + M_z^2 = 1$, from which it can be obtained that:

$$\sum_{k=1}^{\infty} \tilde{F}_{+k} + \tilde{F}_{-k} + \tilde{Z}_k + \tilde{Z}_k^* = 1 \quad (2.42)$$

Also, extra redundancy dependencies exist such as [19]:

$$\tilde{F}_{+k}^* = \tilde{F}_{-k} \quad (2.43)$$

and,

$$\tilde{Z}_k^* = \tilde{Z}_{-k} \tag{2.44}$$

This discussion presented the building blocks of the EPG framework.

2.1.8 Turbo Spin Echo from an EPG perspective

The magnetization response of a Turbo Spin Echo (TSE) sequence can be directly obtained by applying the EPG formalism. The Carr-Purcell-Meiboom-Gill (CPMG) condition must be satisfied in order to obtain and maintain correct refocusing throughout the echo train. This requires the initial excitation and refocusing pulses to be orthogonal, or in other words, 90° out of phase (reduce the effect of refocusing imperfections). With this in mind the T-matrix from Equation 2.41 is set as:

$$T(\pi/2,0) = \begin{pmatrix} 0.5 & 0.5 & -i \\ 0.5 & 0.5 & i \\ -0.5i & 0.5i & 0 \end{pmatrix} \text{ and } T(\pi,\pi/2) = \begin{pmatrix} 0 & -1 & 0 \\ -1 & 0 & 0 \\ 0 & 0 & -1 \end{pmatrix} \tag{2.45}$$

This allows an easy description of what we expect the magnetization to behave. Assuming no relaxation is present, and an initial state $\tilde{F}_0^- = [0,0,1]^T$ the excitation pulse $T(\pi/2,0)$ will send all the magnetization to the transverse plane $\tilde{F}_0^+ = [-i,i,0]^T$. Because of the equidistant time distance between RF pulses in the TSE sequence it is very simple to define a shift operator that depicts the dephasing of states in the magnetization Fourier domain [19, 20]:

$$S(\Delta k) : \tilde{F}_k \rightarrow \tilde{F}_{k+\Delta k} \text{ and } \tilde{Z}_k \rightarrow \tilde{Z}_k \tag{2.46}$$

This means that the population of $\tilde{F}_0^+$ will evolve to $\tilde{F}_1^-$. Further, $T(\pi,\pi/2)$ will shift the entire population from the dephasing partition ($\tilde{F}_1^-$) to the rephasing partition ($\tilde{F}_{-1}^+$).

Commonly [19, 20, 22–24], the states dephasing evolution or pathway is described throughout the literature as shown in Figure 2.5. This figure allows, without prior knowledge of the correct refocusing pulse to be applied, to predict the correct timings of the echo generation and how different dephasing pathways may interact throughout the experiment if perfect 180° refocusing are not applied (see black lines in Figure 2.5) and generate unwanted stimulated echoes. The pathway generated by the TSE experiment discussed above in this text (perfect refocusing is assured) is shown by the orange pathway. This quick and simple

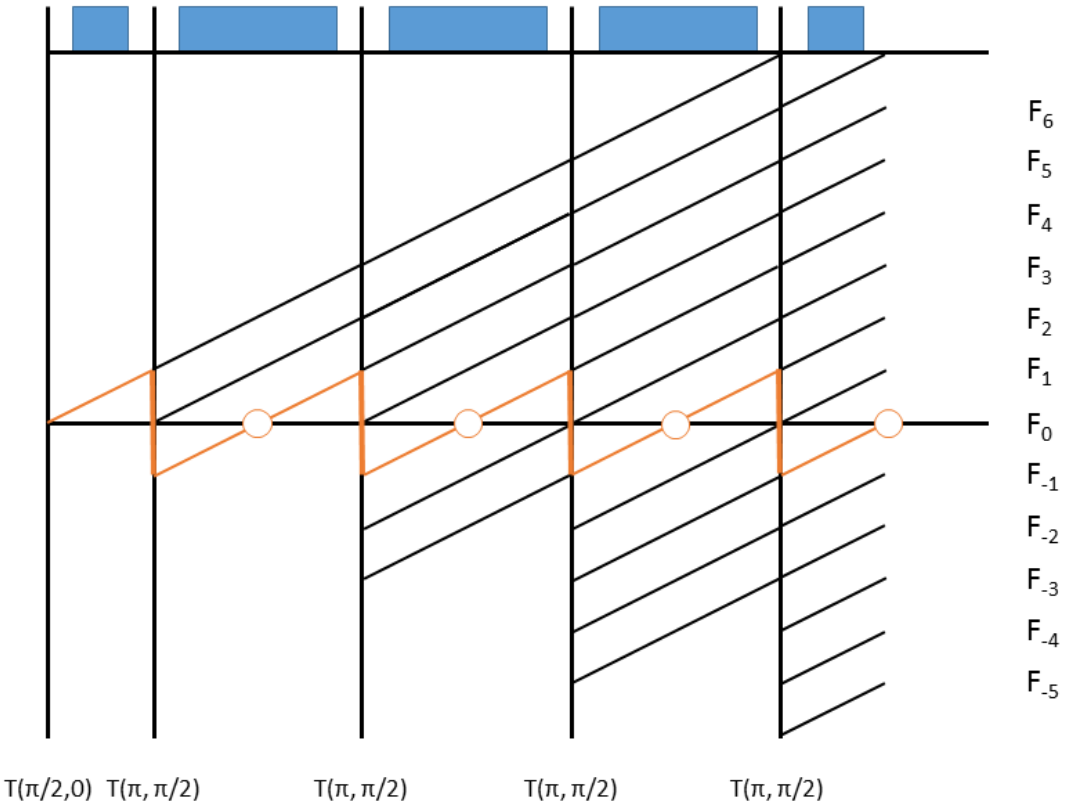

Figure 2.5: Extended Phase Graph for a CPMG multi-echo sequence. Pulses are represented by vertical lines and state evolution due to gradient dephasing shown by solid black lines between pulses. Orange lines represent the specific pathway generated by a TSE experiment with $90°$ excitation pulse and $180°$ refocusing pulse.

example demonstrates how powerful this framework can be to obtain a deeper understanding about how the gradients and RF pulses interact for measured signal formation.

2.1.9 SPGR - Spoiled Gradient Echo

For a gradient echo sequence with $T_R >> 1/R_2$, all transverse magnetization is zero before the next RF-pulse is applied. However this results in long acquisition times which are not practical if we want to do a certain amount of measurements with different acquisition parameters. We are interested in a regime where $T_R < 1/R_2$ (fast sequence), however this implies that there is still some transverse magnetization prior to each RF pulse. In this situation, spoiling may be obtained by applying a spoiler gradient and a spoiler RF pulse in order to force the transverse magnetization to be zero prior to each excitation [12, 24–27]. It is important to guarantee that spoiling occurs before each RF pulse because it allows the magnetization vector to evolve towards a steady-state solution that is

well known throughout the literature [4, 12, 24, 28, 29] and shown in the following equation:

$$S_{SPGR} = M_0 \frac{1 - E_1}{1 - E_1 \cos(\theta)} \sin(\theta) e^{-T_E R_2^*} \tag{2.47}$$

where, M_0 is the voxel proton spin density, θ is the applied flip angle and $E_1 = e^{-T_R R_1}$.

Equation 2.47, known as the Ernst formula [24], can only be applied as long as the correct spoiling before each RF pulse is guaranteed. If no spoiling is applied a transverse magnetization interference appears altering the expected signal behaviour either constructively or destructively [12, 24]. This can be seen by the extended phase graph diagram presented in Figure 2.6 where the black lines represent all the different pathways that may be populated and contribute to signal if no spoiling is guaranteed. On the other hand, if correct spoiling is applied only the $\tilde{F}_0$ state will contribute to the measured signal and the central (orange) pathway will explain the signal evolution.

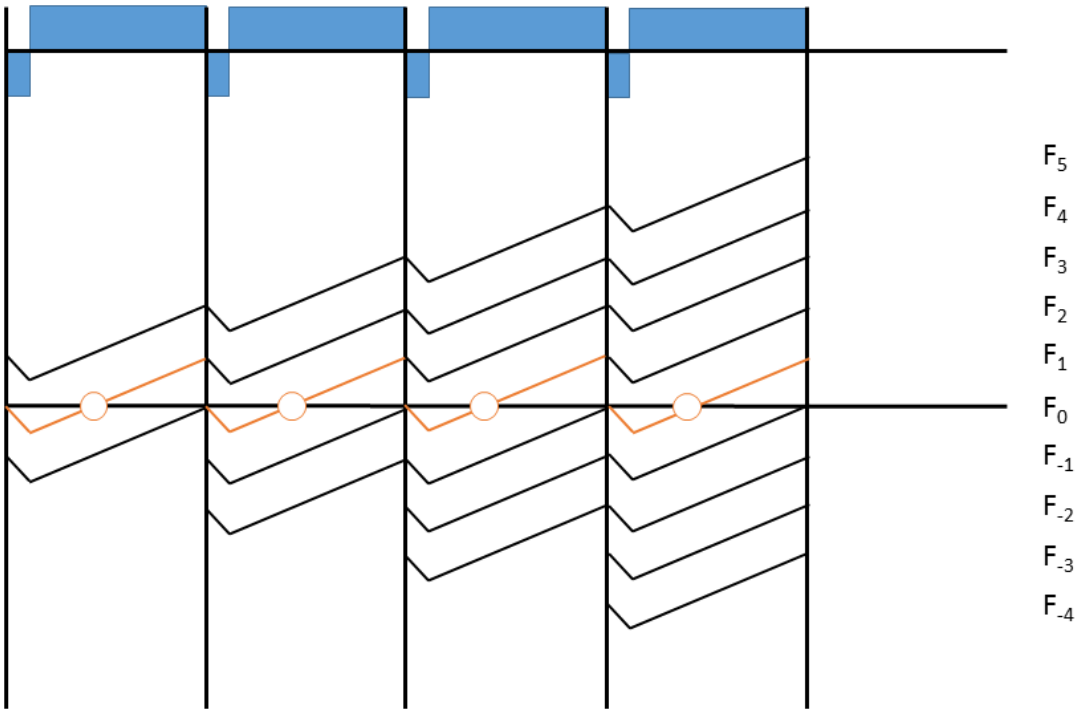

Figure 2.6: Extended Phase Graph diagram for a gradient echo experiment. RF pulses are represented by vertical lines and possible state evolution pathways due to the applies gradients (blue) are shown by solid black lines between pulses. Orange pathways represent the specific pathway generated by a correctly spoiled gradient echo sequence.

2.1.10 bSSFP - Balanced Steady State Free Precession

The balanced steady state free precession (bSSFP) is a very fast gradient echo sequence, that makes use of both longitudinal and transverse magnetization to produce a dynamic equilibrium state for a fixed $T_R << 1/R_2 < 1/R_1$ [4, 24, 30]. Contrary to the SPGR, instead of making use of gradient or RF spoiling techniques to guarantee control of the transverse magnetization, the bSSFP approach rewinds the magnetization so that only the $\tilde{F}_0$ state is present at each RF pulse. This can easily be seen in the EPG diagram of Figure 2.7 where only one single pathway is allowed for the spins to evolve. If the rewind is correctly applied this sequence guarantees that all the magnetization will never leave the $\tilde{F}_0$ resulting in a very high signal-to-noise ratio acquisition.

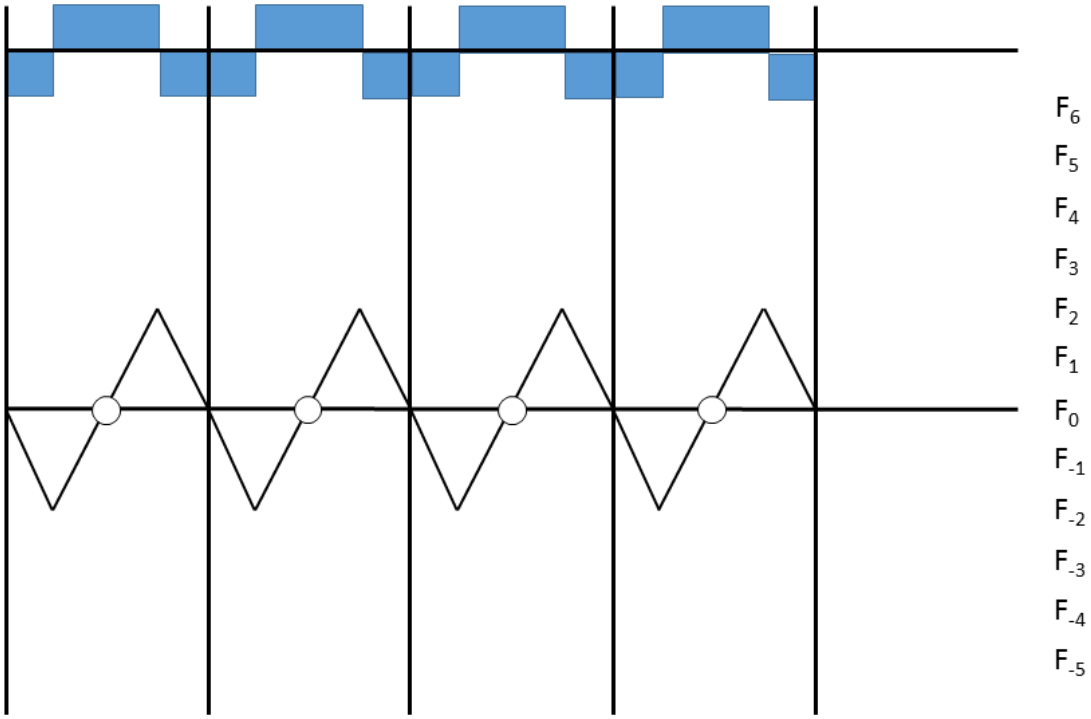

Figure 2.7: Extended Phase Graph diagram for a balance Steady State Free Precession sequence. Before each RF pulse all applied gradients are balance (zero net area) in order to avoid populating higher order $\tilde{F}_n$ states. The sequence offers a very high signal-to-noise ratio and presents a R_1/R_2 contrast.

Because both longitudinal and transverse magnetization need to be taken into account on this type of MR sequence a more complex mathematical description of this signal is necessary. Assuming an initial magnetization M_0, relaxation variables $E_1 = e^{-T_R R_1}$ and $E_2 = e^{-T_R R_2}$ it is possible to write out the individual

components of the magnetization vector in its steady-state [12]:

$$M_x^{SS} = M_0(1 - E_1)\frac{E_2 \sin\theta \sin(\beta)}{d} \tag{2.48}$$

$$M_y^{SS} = M_0(1 - E_1)\frac{(1 - E_2\cos(\beta))\sin(\theta)}{d} \tag{2.49}$$

$$M_z^{SS} = M_0(1 - E_1)\frac{[1 - E_2\cos(\beta)) - E_2\cos(\theta)(\cos(\beta) - E_2)]}{d} \tag{2.50}$$

where,

$$d = (1 - E_1\cos(\theta))(1 - E_2\cos(\beta)) - E_2(E_1 - \cos(\theta))(E_2 - \cos(\beta)) \tag{2.51}$$

Here, $\beta = \Delta\Omega T_R = 2\pi\gamma\delta B_0 T_R + \Phi_{RF}$ is the off resonance dephasing angle resulting from frequency offset $\Delta\Omega$(Hz) plus the rotation induced by incrementing the RF pulse phase Φ_{RF} at each T_R^{SSFP} in radians. It is important to notice, although regarded as a Gradient Echo sequence, bSSFP signal has Spin-Echo characteristics as long as $T_E = T_R^{bSSFP}/2$ [31].

2.2 Summary Conclusion

This chapter aimed to summarize the building blocks from which the work developed throughout this thesis is based on. Exploring and understanding the limits under which the analytical description of each sequence is valid and how they can or cannot be used in the estimation of relaxation parameters will be the main focus of the following chapters.

Chapter 3

MR Relaxometry

The ability to probe tissue specific relaxation times has been sought by the MRI scientific community due to its promise of being more reliable in multi-centre studies or clinical trials [5, 32, 33]. Also, the ability to quantify tissue relaxation properties, as a reliable and absolute measure, would allow MR images to influence clinical decisions in the same way as, for example, body temperature or blood pressure do [34]. The following chapter dwells on current established relaxometry methods. It starts by introducing both spin echo and gradient echo approaches to estimate relaxation times of interest. Given their time efficiency, a bigger emphasis is given to gradient echo methods where a reflection on currently known sources of signal bias as well as the necessary state of the art precautions that must be taken in order to guarantee a precise and accurate measurement are presented.

3.1 Gold-Standard Relaxometry

3.1.1 Inversion Recovery T1 Measurement

Gold standard T_1 relaxometry measurements make use of inversion recovery spin echo sequences (Equation 2.26). In this approach the equilibrium magnetization is inverted with a preparation pulse (typically $180°$) and images are acquired at different stages of the T_1 recovery. As an example, Figure 3.1 demonstrates a series of IR single shot TSE sequences acquired at inversion times of $T_I = 200ms$ (top-left) to $T_I = 1800ms$ (bottom-right) in increments of $200ms$.

The sampled data can then be used to compose a voxelwise estimation of M_0

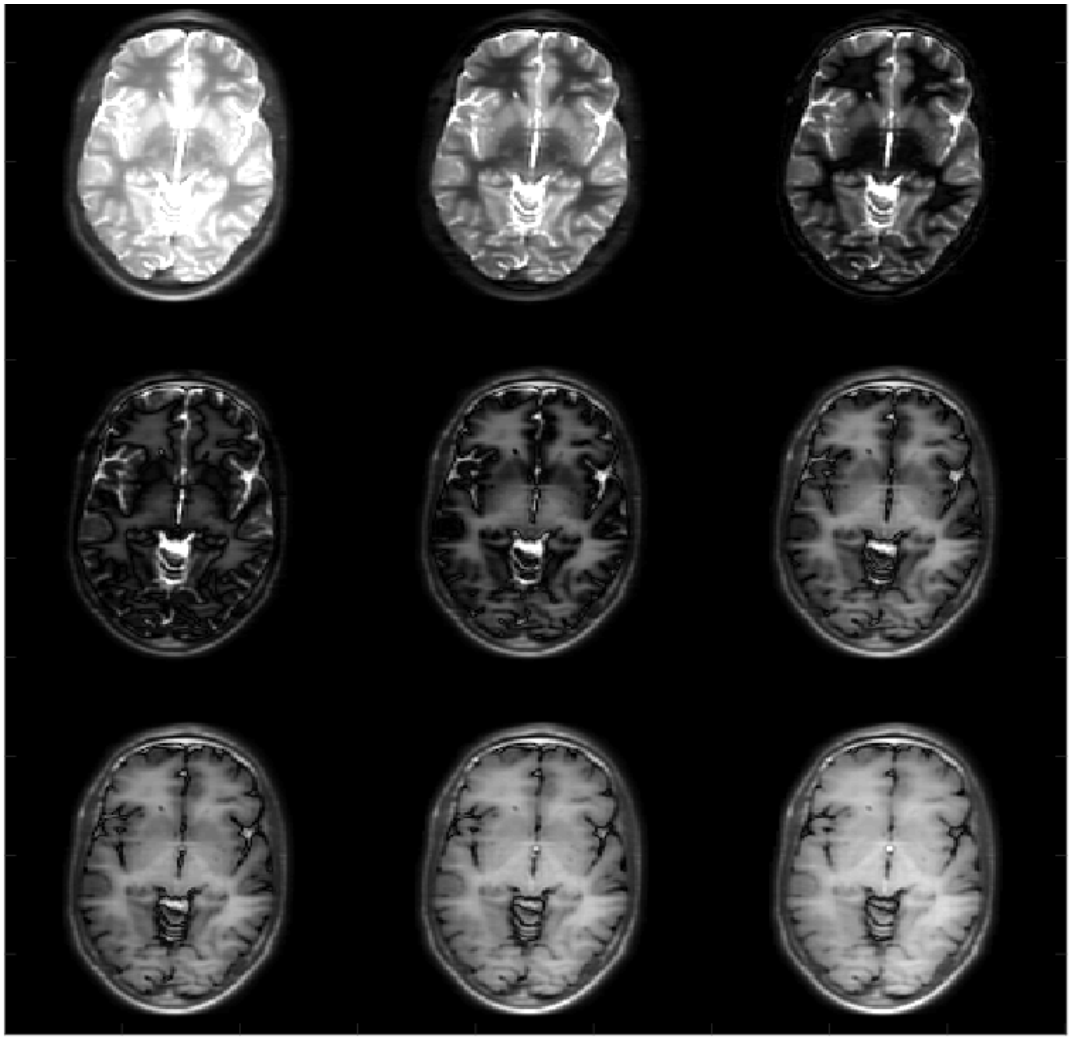

Figure 3.1: Exemplar IR-TSE T_1 weighted images sampled at inversion times of $T_I = 200ms$ (top-left) to $T_I = 1800ms$ (bottom-right) in increments of $200ms$. Images were acquired $1.4 \times 1.6 \times 4.0mm^3$ and an in-plane field of view of $250 \times 250mm$.

and T_1 given the expected mono-exponential recovery of Equation 2.26. Although regarded as being accurate, this approach can be hindered by things such as imperfect inversion profiles (in slice selective acquisitions), Rician noise bias close to the null point (if magnitude images are used), or other unknown sources of signal bias that are not taken into account by the analytical mathematical expression. Furthermore, this approach requires long acquisition times because the magnetization must be allowed to recover before each phase encode measurement ($T_R >> T_1$). Its inherently slow nature therefore hinders its clinical applicability explaining why relaxometry hasn't been adopted as a clinical standard.

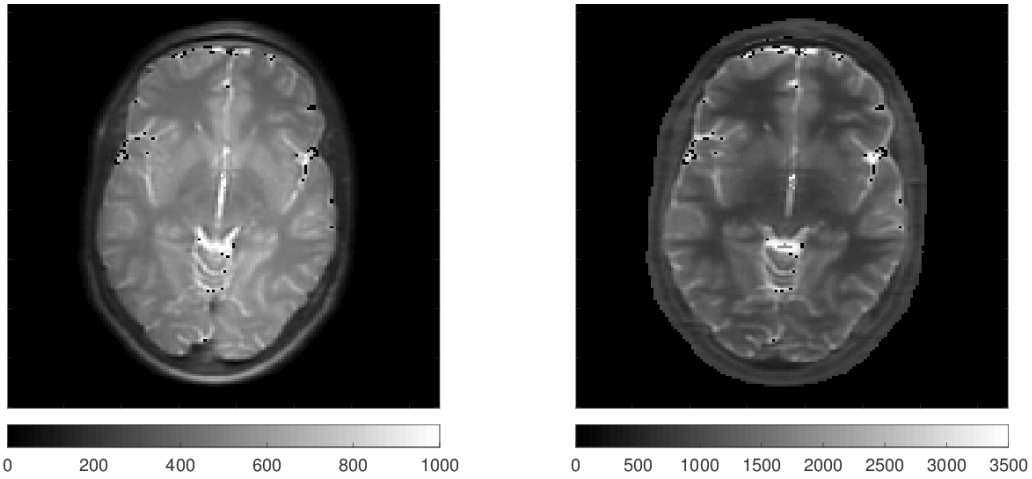

Figure 3.2: Exemplar M_0 (left) and T_1 (right) estimated maps from spin echo data shown in Figure 3.1.

3.1.2 Spin-Echo T2 Measurement

The gold standard methods for T_2 relaxometry are based on spin echo acquisitions. Estimates of T_2 are obtained by acquiring images at different echo times T_E in order to sample along a T_2 decay curve (equation 2.19). Although being generally acknowledged as the most accurate known method of quantifying T_2, its long duration hinders its clinical applicability [35]. In order to circumvent this issue, a multiple echo spin-echo approach, can be used to sample all the desired echoes within one excitation by systematically refocusing the available magnetization with 180° pulses. However, the obtained gain in acquisition time comes at the cost of accuracy loss due to residual imperfections [35–37] which are not necessarily taken into account in the spin echo decay analytical solution. Common causes are imperfect refocusing due to slice profiles, RF interference or purposeful reduction in refocusing angles due to energy deposition constraints [36, 37] inducing stimulated or indirect echoes. All sources, which are not taken into account, responsible for either increasing or decreasing the measured signal intensities are responsible for biasing the desired estimation.

For demonstration purposes, Figure 3.3 presents a single, *in vivo* representative, axial slice sampled using multi-echo SE (CPMG) acquisition. The images were sampled with echo times between $T_E = 10ms$ (top-left) until $T_E = 320ms$ in incremental steps of $10ms$. As expected from Equation 2.19 at short echo times contrast is mainly due to proton density ($T_E \approx 0$), while for longer echo times contrast is mainly due to different T_2 of tissues. Given the data shown in Figure 3.3, Equation 2.19 can be used to make a voxelwise estimation of the relaxation parameter $T_2 = 1/R_2$ and initial magnetization $M_T(t = 0)$. The reader is invited to

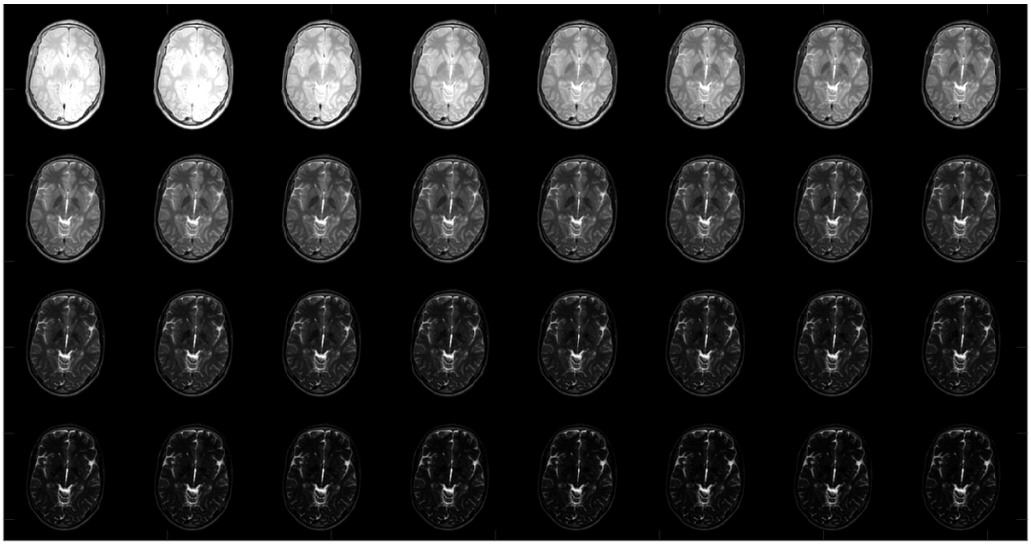

Figure 3.3: Montage of multi echo SE T_2 weighted images sampled at 32 different echo times equally spaced echo times between $T_E = 10ms$ (top-left) and $T_E = 320ms$ (bottom-right).

note that in order to mitigate stimulated echo contributions, it is common practice to only use even echoes for T_2 estimation [15]. An illustrative example can be seen in Figure 3.4 where estimated maps of $M_T(t = 0)$ (left) and T_2 (right) are shown.

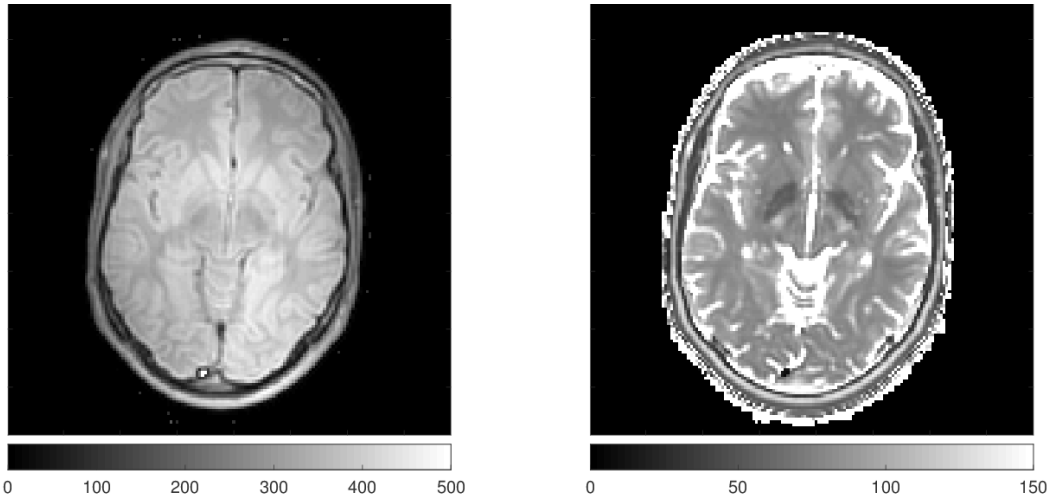

Figure 3.4: Exemplar $M_T(t = 0)$ (left) and T_2 (right) estimated maps from spin echo data shown in Figure 3.3.

Currently, the development of T_2 of relaxometry methods is an active area of research and a reliable common ground must still be found [36] between them. More recently [3–5, 38–42], gradient echo methods have been shown to be capable of reliably estimating T_1 and T_2 in clinically feasible times and will be the main

focus of this work.

3.2 Driven Equilibrium Single Pulse Observation of T1 and T2

Driven Equilibrium Single Pulse Observation of T_1 and T_2 (DESPOT) originally called variable nutation angle method was first introduced as a way to estimate T_1 by applying a set of spoiled gradient echo (SPGR) measurements over different flip angles [28]. The DESPOT nomenclature was first introduced by John Homer and Martin S. Beevers in 1985 [28] and further expanded to DESPOT1 and DESPOT2 by Deoni et al. in 2003 [4] when they suggested the use of a balanced steady-state free precession sequences (bSSFP) to map T_2 information after T_1 had been assessed.

The parameters of interest are obtained from a set of SPGR and bSSFP images acquired at fixed T_R and incrementally increased flip angle θ. Following the description presented in [4] the SPGR signal (Equation 2.47 can be represented in the linear ($Y = mX + b$) form by:

$$\frac{S_{SPGR}}{\sin\theta} = e^{-T_R/T_1}\frac{S_{SPGR}}{\tan\theta} + M_0(1 - e^{-T_R/T_1}) \tag{3.1}$$

from which the slope m and Y-intercept b can be estimated by linear regression, allowing us to extract T_1 and M_0 as being:

$$T_1 = -T_R/\log(m) \tag{3.2}$$

$$M_0 = b/(1 - m) \tag{3.3}$$

Once T_1 has been assessed it is used in a linearised model version of bSSFP equations (Equations 2.51) in order to estimate T_2:

$$\frac{S_{bSSFP}}{\sin\theta} = \frac{e^{-T_R/T_1} - e^{-T_R/T_2}}{1 - e^{-T_R/T_1}e^{-T_R/T_2}}\frac{S_{bSSFP}}{\tan\theta} + \frac{M_0(1 - e^{-T_R/T_1})}{1 - e^{-T_R/T_1}e^{-T_R/T_2}} \tag{3.4}$$

where, also by linear regression we obtain a new m and b resulting in:

$$T_2 = -T_R/\log\left(\frac{m - e^{-T_R/T_1}}{me^{-T_R/T_1}} - 1\right) \tag{3.5}$$

$$M_0 = b(e^{-T_R/T_1}e^{-T_R/T_2} - 1)/(1 - e^{-T_R/T_1}) \tag{3.6}$$

The linearised approach, just presented, is very powerful as it allows very little computation time to produce estimation maps for the entire 3D volume. However, the magnetization evolution is complex and seldom follows the expected analytical solutions which rely on several assumptions (e.g. instantaneous excitation, correct magnetization spoiling, etc,...). The following sub-sections dwell precisely on some of these assumptions in order to identify the measurement conditions that will be applied throughout this thesis.

3.2.1 B1 field correction

When it first was proposed [28] the DESPOT1 approach made no assumptions regarding inhomogeneities of the transmit field B_1. Nowadays, as magnets operate at higher field strengths, the Larmour frequency of the excitation field has increased such that at 3T its wavelength becomes comparable to the size of the human body. This causes standing wave effects that result in a position dependant distribution of the desired flip angle. In other words, at each measured voxel the effective flip angle θ_e is related to the prescribed flip angle θ_p by a scaling factor $\kappa = \theta_e/\theta_p$. As an example, the effect of incorrect knowledge of κ on the SPGR signal evolution is shown in Figure 3.5. To highlight the importance of this correction, bottom of Figure 3.5 demonstrates the effect of incorrect knowledge of κ on the estimated apparent T_1^{app} (blue line). This is known to induce a quadratic error [3, 43, 44] such that $T_1^{app} \approx \kappa^2 T_1$ (yellow line).

Several approaches have been proposed to address this issue in the context of relaxometry. In the most accepted approach, B_1 spatial distribution can be sampled *a priori* using conventional mapping methods such as Actual Flip Angle Imaging (AFI) [45, 46], the Saturated Double Angle Method (SDAM) [47] or the Dual Refocusing Echo Acquisition Mode (DREAM) [48]. Once κ is obtained it can be used as a correction factor such that the correct effective flip angle is known on a voxel by voxel basis. In the interest of time, S. Deoni addressed the issue of B_1 correction, in 2007, by acquiring a Magnetization Prepared Recalled Gradient Echo (MPRAGE) with a centre out read-out, half the resolution and interpolated to the same grid as the SPGR acquisition in order to estimate κ jointly with T_1 and M_0 [49]. His approach however, ignores the Look-Locker recovery of the magnetization [50], and assumes that under the proposed conditions the MPRAGE signal can be approximated by the IR signal model which is difficult to guarantee. Hurley et al., [51] have also presented a fit based approach where AFI and SPGR acquisitions and signal models are iteratively evaluated in order to simultaneously

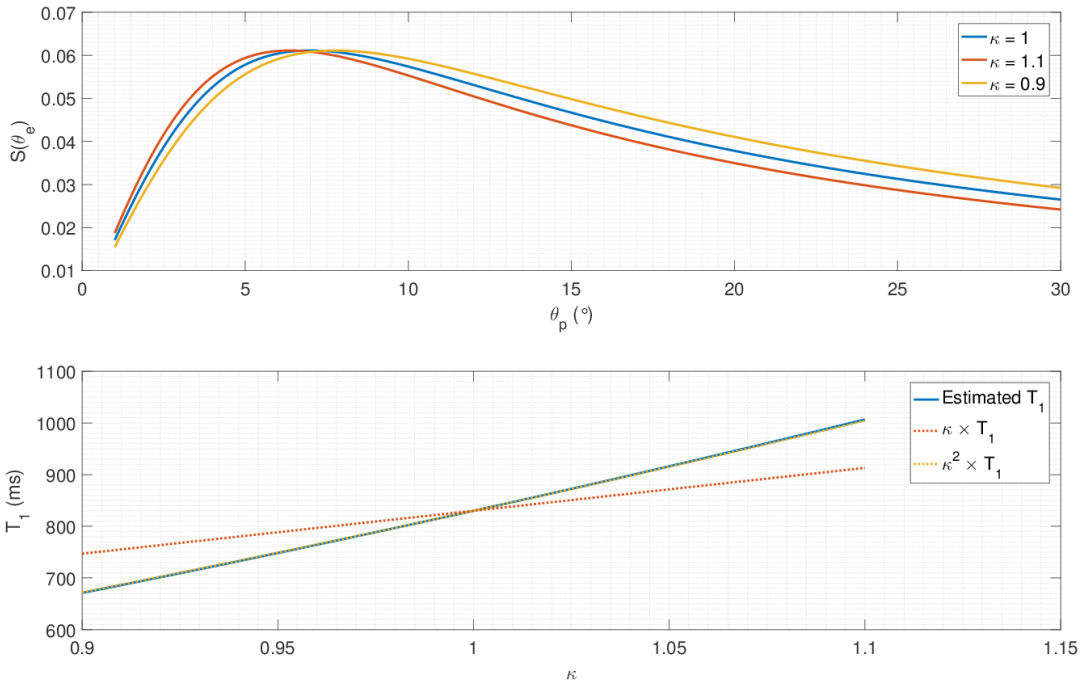

Figure 3.5: For a representative $T_1 = 830ms$ and $T_R = 6.2ms$ the top graph represents the effect of incorrect knowledge of B_1 spatial distribution κ. Blue line represents $\theta_e = \theta_p$, red line $\theta_e = 1.1\theta_p$ and yellow line $\theta_e = 0.9\theta_p$. Bottom graph shows estimated T_1 using the described DESPOT1 approach. Dashed red and yellow line correspond to correct T_1 multiplied by κ and κ^2 respectively showing that incorrect knowledge of κ can be approximated as inducing a quadratic bias on the apparent T_1 [3,43].

estimate T_1 and B_1 distributions.

As an alternative approach, Weiskopf et al. [52] proposed a retrospective procedure (UNICORT) in which B_1 uncorrected T_1 maps are fed into a bias field correction algorithm in order to estimate B_1.

3.2.2 B0 field correction

The first suggestion of DESPOT2 estimation approach in 2004 [41,53] addressed the issue of δB_0 dependency of the bSSFP signal by acquiring images with different RF phase increments (typically $180°$ and $0°$) and combine them via maximum intensity projection prior to fitting T_2 map using the linear model. This approach however, results in residual oscillations in the final estimated maps which can be understood by analysing the plots of Figure 3.6. Figure 3.6 overlays bSSFP signal evolutions as a function of δB_0 for different applied flip angles θ. Signals obtained with RF phase increments of $\phi_{incr} = \pi rad$ (blue) and $\phi_{incr} = 0rad$ (red) are overlaid. Signal obtained, after maximum intensity projection is computed, as

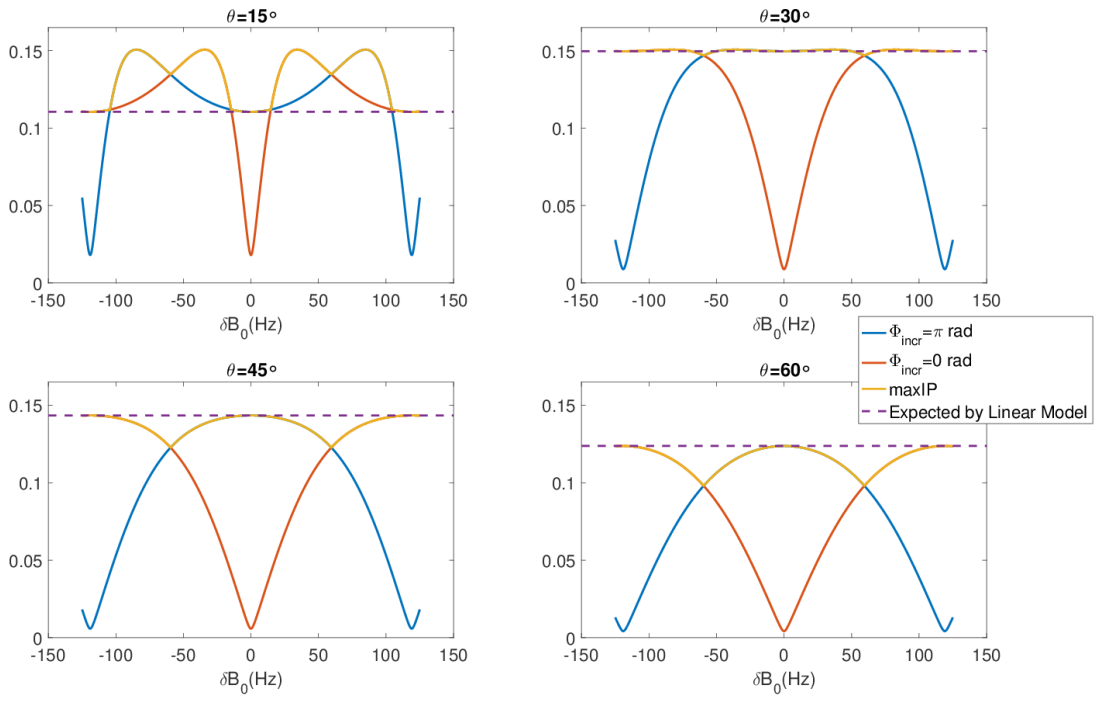

Figure 3.6: Effect of correcting for bSSFP frequency profile using a maximum intensity projection approach. Blue and red lines correspond to bSSFP acquired with same flip angle and opposite phase increment schemes (π and 0 radians per T_R). Yellow line shows the result of maximum intensity projection correction. Purple line define signal ideal signal expected by the model. All signals were modelled with a $T_R = 4.2ms$.

function of δB_0 is highlighted in yellow. "Ideal signal" expected by linear model is highlighted in dashed purple line. If T_2 is estimated based on the maximum intensity projection in areas where the yellow curve is significantly different from the expected signal will induce a T_2 bias which will depend on δB_0.

In the work presented in 2009 S. Deoni dropped the linear DESPOT2 fit approach and its maximum intensity projection and proposed estimating δB_0 map as part of the relaxometry protocol in the so called DESPOT-FM [54]. More recently, an analytical correction for δB_0 induced bSSFP signal variations has been proposed by Jutras et al [55]. In their work, Jutras et al also propose the use of a linear bSSFP model however, a correction term was derived for the incorrect apparent T_2 as a function of both δB_0 and ϕ_{incr} allowing unbiased T_2 estimates to be obtained.

3.2.3 Finite RF pulse Correction

The use of gradient echo steady state methods with current hardware capabilities allows data sampling with repetition times typically in the range between

$T_R = 3 - 5ms$. Although it allows excellent sampling rate, under this regime, the assumption of no relaxation occurring during excitations fails to hold [56–58]. In this section, following the description of [57], a simple mathematical framework for describing bSSFP with known RF pulse duration T_{RF} is presented.

When on resonance (i.e. $\delta B_0 = 0$), common bSSFP sequence alternates between excitation with flip angle $\pm\theta$ ($R(\theta, n\pi), n = 1, 2, 3, ...\#T_R$). This results in a dynamic steady state described by a *zenithal* translation through a fully longitudinal alignment position (3.7). Recalling from Chapter 2 we expect T_2 decay to

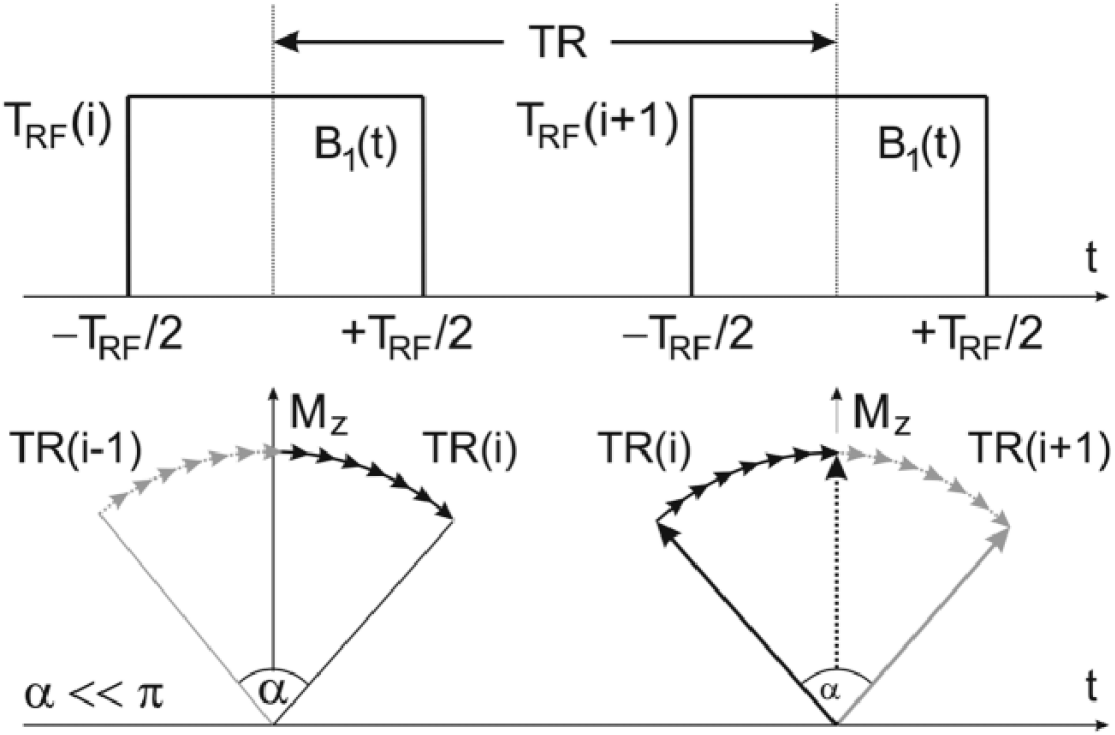

Figure 3.7: Steady-state movement representation within T_R bSSFP with πrad phase cycling. Adapted from [57]

.

occur while the magnetization has some transverse component $\vec{M_T}$. It is therefore reasonable to assume that while aligned with the longitudinal direction the magnetization doesn't suffer from T_2 loss and therefore, the common described steady state overestimates the time magnetization is in the transverse plane. Considering finite RF pulses subject to $\theta <= 180°$ it is shown [56, 57] they only affect transverse magnetization by avoiding T_2 decay during the mean residence time in the longitudinal direction ζT_{RF}. This means the magnetization relationship now follows as [57]:

$$\frac{dM_T(t)}{dt} = -\frac{(1-\zeta)}{T_2} M_T(t) \tag{3.7}$$

$$\frac{dM_z(t)}{dt} = -\frac{M_z(t) - M_0}{T_1} \tag{3.8}$$

and a simple correction:

$$E_2 = e^{-(T_R - \zeta T_R F)/T_2} \tag{3.9}$$

$$\zeta \approx 0.68 - 0.125(1 + \frac{T_{RF}}{T_R})\frac{T_2}{T_1} \tag{3.10}$$

is sufficient to take into account the average time the magnetization spends in the longitudinal axis. Note that ζ is parametrized from numerically solving the Bloch equations and is only valid for hard pulses. However, if a shaped pulse is applied the same correction can be applied given that the effective hard pulse equivalent duration computed. This can be achieved by knowledge of the time-bandwidth product property of the pulse [57].

3.2.4 SPGR and correct spoiling conditions

An additional source of bias and instabilities that requires special care, is the influence of incorrect magnetization spoiling on the SPGR signal [25, 26, 44, 59]. In order to counteract this issue and allow a T_2 independent steady state to be formed, the phase of the applied RF-pulse ϕ_{incr} is incremented at each excitation (RF-spoiling) [25] in combination with gradient spoilers [60] which force the magnetization to interact in a destructive way before each excitation pulse. Figure 3.8 demonstrates the expected SPGR signal evolution of typical white matter relaxation times ($T_1^{WM}/T_2^{WM} = 830/50ms$) for different ϕ_{incr} using the EPG formalism for $\theta = 4^\circ$ (solid blue) and $\theta = 18^\circ$ (solid red). Overlaid as dashed lines are expected Ernst signal solutions for reference. SPGR gradient spoiling area was kept at the default values optimized by the manufacturer software (Release R3.2.2, Philips Achieva-Tx, Best, Netherlands) which result on total phase dispersion of ≈ 7 radians per voxel in the readout direction. The effect of incorrect RF-spoiling is highlighted at the bottom graph of Figure 3.8 where the expected T_1 bias, defined as $\epsilon T_1 = (T_1^{DESPOT1} - T_1^{WM})/T_1^{WM}$, is plotted as a function of applied ϕ_{incr}. Zero bias line (dashed red) is plotted for reference.

Correct signal spoiling however, is also dependent on the interaction between T_1, T_2, θ and T_R^{SPGR}, and may prove to be difficult to obtain for the wide range of relaxation times present in the human brain. Throughout this work, in order to minimize this effect, the EPG framework was employed to generate signal evolutions as a function of T_R^{SPGR} and FA θ for expected T_1 and T_2 values of WM ($T_1^{WM}/T_2^{WM} = 830/50ms$) and GM($T_1^{GM}/T_2^{GM} = 1500/70ms$). EPGR gener-

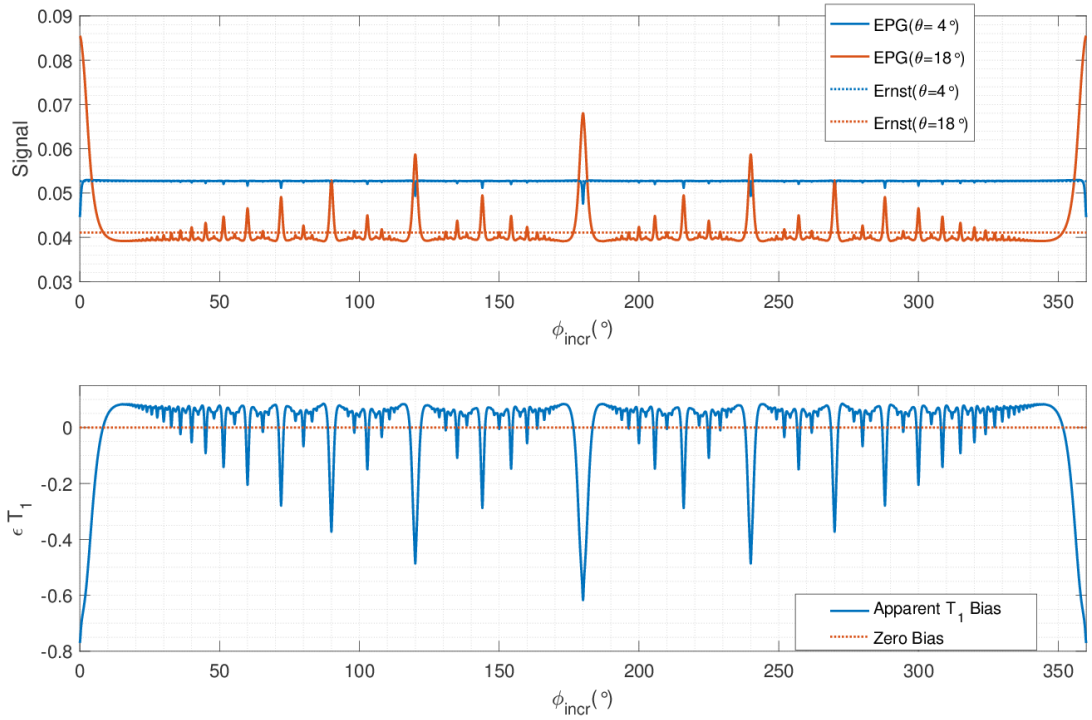

Figure 3.8: Top graph summarizes the comparison between EPG simulation and Ernst expected SPGR signal evolution as a function of RF phase increments ϕ_{RF}. A representative $T_1 = 830ms$ and $T_2 = 50ms$ combibation was assumed. Bottom graph demonstrates apparent T_1 bias ($\epsilon T_1 = (T_1^{DESPOT1} - T_1^{WM})/T_1^{WM}$) using DESPOT1 on EPG simulated data of top graph.

ated signals were then compared with the idealised Ernst signal evolution. For each T_R^{SPGR}/θ combination the EPG signal evolution was computed for a number of $6T_1/T_R^{SPGR}$ excitations in order to guarantee that the steady state was achieved. RF-spoiling was set by incrementing the phase of each RF-pulse at each excitation (n) by $n50^\circ$ [44]. The value of 50° for the phase increment was chosen due to its reported stability [44]. Diffusion effects were taken into account by assuming a diffusion coefficient of $2.3 \times 10^{-9} m^2 s^{-1}$. The parameter $\epsilon_{WM/GM} = 100 \times (S_{WM/GM}^{Ernst} - S_{WM/GM}^{EPG})/S_{WM/GM}^{EPG}$ was defined as the percentage deviation between Ernst and EPG frameworks. Its distribution for the explored grid is shown in Figure 3.9. Figure 3.9 demonstrates the expected signal bias due to incorrect spoiling for different combinations of T_R^{SPGR} and θ^{SPGR}. Red line line corresponds to maximum flip angle for which all considered T_R^{SPGR} result in a WM error smaller then 5%.

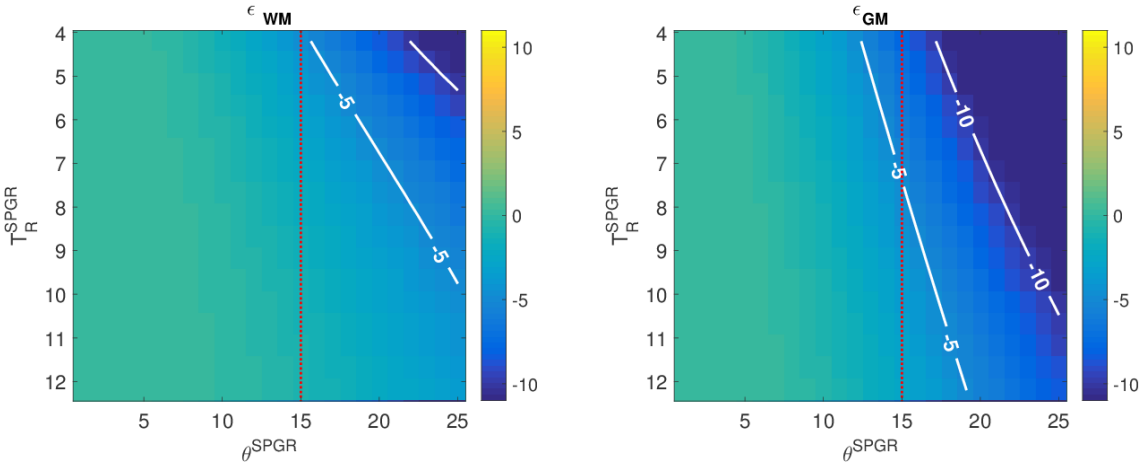

Figure 3.9: Percentage deviation for both WM (left) and GM (right) between EPG signal model and Ernst relationship. iso-contours highlight 5% and 10% signal bias.

3.2.5 Coil Combination

With the evolution of parallel imaging, the use of multi-channel receive coils has become current practice in a clinical setting. Although substantial discussion has been presented regarding optimal fitting strategies for T_1 mapping, there has been scarce discussion on how these methods should be applied for multichannel data [61]. Building on the discussion presented in [61] there are three main ways multichannel data can be handled:

1. Treat each channel signal as an individual measurement and jointly estimate relaxation data from them;

2. Treat each channel as independent acquisition and thereafter combine the separately estimated relaxation parameters;

3. Create a composite image from multichannel data such data relaxation parameters estimation is performed on a high SNR signal;

The work developed throughout this thesis mainly focused using composite image with higher SNR as it will reduce the dimensionality of the estimation problem and it has been reported to diminish noise amplification [61]. Although appealing, special care needs to be taken when combining different measurement channels into a single composite image. A practical and naive approach to combine multi-channel data is to take the square-root of the sum-of-squares (SOS) of all channels [61, 62]. This approach however, has two main problems. Firstly, SOS, by definition, discards all phase information present in the measured signal and will induce signal bias due to the well-known Rician noise distributions of MR magnitude images, secondly final composite image will still be modulated by each channel sensitivity profile [61, 62]. The first issue however, can be avoided

if coil sensitivity is estimated *a priori* allowing optimal coil combination [61–63] into a high SNR image. Although other coil combination procedures such as GRAPPA [64] exist, in this work SENSE [63] was preferred as it was readily available in our imaging system.

3.3 Summary Conclusion

This chapter sought to present a brief summary of some of the current methodologies applied in MR Relaxometry. “Gold Standard methods”, although appealing, do not produce consistent results between different studies [6] and require long acquisition times which hinders their clinical applicability. On the other hand, gradient echo methods such as DESPOT have the advantage of providing fast (efficient) sampling. However, they are more susceptible to error, such as due to B1 and B0 inhomogeneities, and a consensus between relaxation times determined by these methods and spin echo methods still has not been found [6]. The chapter provided a review of the currently known sources of error that impact relaxation time estimation from variable flip angle methods. Methodologies for minimizing and/or avoiding them are discussed and incorporated in the succeeding chapters of this thesis and are summarised in Table 3.1 for easy reference.

Variable Flip Angle Relaxometry Common Sources of Error

Error Source	Sequence Type	Type of Bias	Solution Employed
B1 Field	bSSFP, SPGR	Over and underestimation of relaxation times, a B1 "imprint" can be seen in the estimated maps	Sample B1 calibration map using AFI
B0 Field	bSSFP	Both over and underestimation of T2, a B0 "imprint" can be seen in the map	Sampled bSSFP at with different RF phase increments in order to estimate underlying B0
RF pulse duration	bSSFP	Systematic overestimation of T2	Record RF pulse duration and correct T2 decay per Equation 3.10
Spoiling	SPGR	T1 systematically biased depending on degree of spoiling. Effect can change with both RF and Gradient spoiling approaches.	RF phase spoiling kept fixed at 50°. Magnetization evolution simualted using EPG framework and employed gradients. Restricted our operation regimes to ensure less then 5% WM signal deviations
Coil Combination	bSSFP, SPGR	Rician Bias of signal where coil sensitivities are poor	One high SNR image is constructed from the coil array prior to performing relaxometry estimation. SENSE reconstruction was employed throughout this text

Table 3.1: Summary table of the different sources of relaxometry estimation bias identified in this thesis and how they were addressed in the following chapters.

Chapter 4

Cramér-Rao Lower Bound in MR Relaxometry

In their 2013 paper [9], Christopher L. Lankford and Mark D. Does, used a statistical tool known as the Cramér-Rao Lower bound (CRLB) as a way to predict the minimum possible variance one can obtain when estimating parameters using the multi compartment DESPOT two-pool model (mcDESPOT). The CRLB predicts the minimum obtainable variance of estimated model parameters given the noise properties of the measurement experiment [9, 65, 66] and has previously been used as an optimization tool for MR protocols [65–69]. This chapter focuses on the adaptation of this statistical tool in order to design an optimization tool which seeks to enhance DESPOT-type relaxometry protocols estimation precision.

4.1 Introduction

4.1.1 CRLB under Gaussian Distributed Noise

The most common way to derive the CRLB is assuming all measurements are modulated by Gaussian distributed noise [9, 67] which is a valid assumption in MRI signal acquisitions as long as sufficient SNR is guaranteed [70]. Following the notation presented in [9], if we assume a model $g(x, \Theta)$, where $x \in \Re^N$ is an independent parameter vector (for what this work is concerned input flip angles at a given T_R) and $\Theta \in \Re^M$ is a vector of model parameters to be estimated such as M_0, T_1 and T_2. Considering a set of N noisy observations $y \in \Re^N$ from which we obtain a random estimate $\widehat{\Theta}$, the estimated parameter vector covariance matrix

$\Sigma_{\widehat{\theta}}$ is known to be bounded by [9, 67, 71]

$$\Sigma_{\widehat{\Theta}} \geq \frac{\partial E[\widehat{\Theta}]}{\partial \Theta} F^{-1} \frac{\partial E[\widehat{\Theta}]}{\partial \Theta}^{T} \tag{4.1}$$

where, F is the Fisher information matrix, $E[.]$ is the expectation operator, and the derivative of one vector with respect to another follows the convention $(\partial a/\partial b)_{ij} \equiv \partial a_i/\partial b_j$. We note that $A \geq B$ means that $A - B \geq 0$ or in other words is a positive semi-definite matrix. In Equation 4.1 the CRLB also includes the estimator gradient matrix $\frac{\partial E[\widehat{\Theta}]}{\partial \Theta}$ which represents the rate of change the expected value of the estimate with respect to each parameter. This is important when restrictions on the estimation process yield biased estimates $E[\widehat{\Theta}] - \Theta \neq 0$, however for unbiased estimates ($E[\widehat{\Theta}] - \Theta = 0$) this may be replaced by an identity matrix. Unless stated otherwise, this work always assumes unbiased conditions and therefore $\partial E[\widehat{\Theta}]/\partial \Theta$ is considered to be the identity matrix. In lay terms, the matrix F represents how much information the N noisy observations (y) contain about the parameter vector Θ. On a more detailed note, this is achieved by considering the curvature of the log-likelihood hyper-surface $L = p(y|\Theta)$ [9]. In the case of Gaussian distributed noise of the observed data $y_i, i = 1, 2, 3, \ldots, N$ the matrix F simplifies into the $M \times M$ array with rows/columns (j/k) given by [9, 66, 67]:

$$F_{jk} = E(\frac{\partial^2 L}{\partial \Theta_j \partial \Theta_k}) = \sum_{i=1}^{N} (\frac{1}{\sigma_i^2} \frac{\partial g_i}{\partial \Theta_j} \frac{\partial g_i}{\partial \Theta_k}) \tag{4.2}$$

In order to estimated the CRLB, both SPGR (Equation 2.47) and bSSFP (Equations 2.51) are, for simplicity, numerically differentiated throughout this work via forward differentiation.

Because all signals are considered to be magnitude of a complex number, and we add Gaussian distributed noise to both the real and imaginary components, the resulting measured signal noise is known to follow a Rician distribution [70]. This means that the Gaussian CRLB model is only valid for signals with sufficiently high SNR (SNR≥ 3) [9, 70], therefore, it was found instructive to present how to estimate the CRLB assuming Rician distribution of the noise model.

CRLB under Rician Distributed Noise

The Rice distribution is described in equation 4.3 and is built from the log-likelihood of a set of N measurements that can be expressed as:

$$L = \sum_{i=1}^{N} [\log M_i - 2\log\sigma + \log I_0(\frac{A_i M_i}{\sigma^2}) - \frac{A_i^2 + M_i^2}{2\sigma^2}] \tag{4.3}$$

Where A_i and M_i are, for the i^{th} measurement, respectively the signal predicted by the model ($g(x, \widehat{\Theta})$) and the actual measurement. With this in mind the F may be computed by:

$$F_{jk} = E(\frac{\partial^2 L}{\partial\Theta_j \partial\Theta_k}) = \int_0^\infty \frac{\partial^2 L}{\partial\Theta_j \partial\Theta_k} P(M) dM \tag{4.4}$$

which according to [67] can be expressed as:

$$E(\frac{\partial^2 L}{\partial\Theta_j \partial\Theta_k}) = \sum_{i=1}^{N} \frac{1}{\sigma^4} \frac{\partial A_i}{\partial\Theta_j} \frac{\partial A_i}{\partial\Theta_k} (Z_k - A_k^2) \tag{4.5}$$

where, considering I_i as a Bessel function of the ith order,

$$Z_k = \int_0^\infty A_i^2 I_1^2(\frac{A_i M}{\sigma^2}) I_0^{-2}(\frac{A_i M}{\sigma^2}) P(M) dM \tag{4.6}$$

with the function Z_k being numerically computed, since it does not have a closed form [67].

Although presented here, the Rician description was not used throughout this thesis, as it computationally more demanding, and therefore it was adopted, for simplicity, to restrict the work presented to operate in the Gaussian regime.

4.2 Methods: CRLB as Cost Function

So far, given a certain number of fixed measurements, the computation of the lowest obtainable variance has been discussed. Instead, in this section, the CRLB is used as a cost function to optimize DESPOT estimation protocols. In other words, the main goal of the work here presented is to create a framework which, for a given model and number of measurements, selects in a rigorous way, which sampled data allows the achievement of the lowest estimation variance possible. The CRLB has been previously used to optimize experiment design in diffusion

MRI [67] and quantitative magnetization transfer MRI [66]. Following the methodology proposed in [66], we sought to enhance estimation precision for multiple parameter estimates by considering several diagonal elements of $\Sigma_{\widehat{\Theta}}$ simultaneously. This corresponds to only considering the minimal obtainable variance of each parameter of interest. In order to achieve equal relative precision for each degree of freedom, the CRLB of each parameter is weighted by the inverse square of the parameter value. This means we can compute a root mean squared coefficient of variance CV_{rms}^{CRLB} which we then seek to optimize:

$$\mathrm{CV}_{rms}^{CRLB} = \sqrt{\sum_{m=1}^{M} \frac{[\Sigma_{\widehat{\Theta}}]_{mm}}{\Theta_m^2}} \tag{4.7}$$

It is important to notice that CV_{rms}^{CRLB} is computed for a specific parameter vector $\vec{\Theta}$. However, we are interested in being able to evaluate CV_{rms}^{CRLB} over a wide range of different $\vec{\Theta}$. Therefore, we compute CV_{rms}^{CRLB} over G different parameter vectors $\vec{\Theta}_G = [\Theta_1^G, \Theta_2^G, \ldots, \Theta_M^G]$ and the maximum value obtained is minimized resulting in the cost function

$$\mathrm{CF}_{grid} = \mathrm{max}_G\Big(\mathrm{CV}_{rms}^{CRLB}(\vec{\Theta}_G)\Big). \tag{4.8}$$

Here, the maximum of the considered grid is extracted in order to minimize the worse case scenario. To exemplify, if one is interested in assuming our model estimate $\widehat{\theta} = [\rho, T_1, T_2]$ but we are only interested in improving T_1 and T_2 estimation (effectively we are not interested in ρ) then this means that Equation 4.8 will simplify into:

$$\mathrm{CF}_{grid} = \mathrm{max}_G\left(\sqrt{\frac{\sigma_{CRLB}^2(T_{1G})}{T_{1G}^2} + \frac{\sigma_{CRLB}^2(T_{2G})}{T_{2G}^2}}\right) \tag{4.9}$$

4.2.1 Optimizing DESPOT1 and DESPOT2

Building on the SPGR (Equation 2.47) and bSSFP (Equation 2.48 to 2.51) signal models, we derive optimal acquisition protocols for both DESPOT1 and DESPOT2 relaxometry approaches. The linearised signal models were avoided mainly for two reasons. Firstly, it restricts all SPGR/bSSFP acquisitions to have fixed T_R. Secondly, it involves a normalization step by $\sin\theta$ and $\tan\theta$ which will affect the expected Gaussian noise distribution. Both DESPOT1 and DESPOT2 optimal protocols were sought through a direct search approach implemented in

MatLab 2016a *patternsearch* optimization toolbox. At each iteration, this algorithm computes a sequence of points (mesh) around the current central point. The cost function is evaluated at each point in the mesh which contracts or expands depending if a lower value of cost function is found (for further details see `http://uk.mathworks.com/help/gads/patternsearch.html`). This routine is not guaranteed to find global optima, so the optimization was simply repeated for 10 randomly distributed starting values. The global optimum, if not obtained, is not expected to dramatically improve the estimation quality compared to the solution achieved as in practice several different local minima are found whose cost-function demonstrate similar performance.

DESPOT1

The full Ernst model as presented in Equation 2.47 was assumed. Adult specific protocols were derived given expected relaxation times for white matter and gray matter such that:

- WM - $\widehat{\Theta}_{c=1} = [M_0^{WM} = 1, T_1^{WM} = 830ms]$ [6];
- GM - $\widehat{\Theta}_{c=2} = [M_0^{GM} = 1, T_1^{GM} = 1500ms]$ [72];

Baseline protocol acquisition parameters were adopted from the work presented by S. Deoni in 2009 [54] and corresponds to $T_R^{SPGR} = 6.2ms$ and $\theta = [4°, 18°]$. It was hypothesised that optimal acquisition schemes might consider different repetition times as well as flip angles. Therefore, defining minimum $T_{R,min}^{SPGR} = 4.2ms$, optimal θ^{SPGR} and T_R^{SPGR} solutions were sought by minimizing Equation 4.8 subject to $\sum T_R^{SPGR} = 12.4ms$.

DESPOT2

Once T_1 has been assessed DESPOT2 can be used to estimate T_2. For simplicity we assume correct knowledge of T_1, which corresponds to not taking into account the noise distribution of the T_1 measurement. We define an optimization grid that is adult brain specific such that:

- WM - $\widehat{\Theta}_{c=1} = [M_0^{WM} = 1, T_2^{WM} = 50ms]$ with $T_1^{WM} = 830ms$ [6, 72];
- GM - $\widehat{\Theta}_{c=2} = [M_0^{GM} = 1, T_2^{GM} = 70ms]$ with $T_1^{GM} = 1500ms$ [72];

To avoid increased banding artefacts, SFFP repetition times were fixed at $T_R^{SSFP} = T_R^{min} = 4.2ms$. Optimal θ^{SSFP} solutions were sought by minimizing Equation 4.8.

Baseline protocol was defined as $T_R = 4.2ms$,$\theta_1 = 15^\circ$ and $\theta_2 = 65^\circ$ [54].

Numerical Validation

Numerical validation of the proposed CRLB optimization framework for DESPOT1 and DESPOT2 was obtained by performing $N = 10^5$ noise independent Monte Carlo trials for both baseline and adult optimized flip angle sets. Complex Gaussian distributed noise with standard deviation $0.05M_0$ (SNR=20) for both the real and imaginary components was added to the signal equation. As in [54], magnitude data is used to estimate relaxation parameters. More specifically for DESPOT2 validation, it was assumed on-resonance conditions ($\delta B_0 = 0$) with RF phase cycling scheme $\Phi_{RF} = 180^\circ$. Instantaneous RF pulse duration was assumed such that $T_{RF} \to 0ms$.

In order to compare baseline with optimized protocols expected estimation coefficient of variation $\text{CV}_{T_1}^{CRLB} = \sigma_{CRLB}^2(T_1)/T_1^2$ is computed for T_1 values ranging from 1ms to 4000ms in 0.1ms steps. The same is repeated for T_2 such that $\text{CV}_{T_2}^{CRLB} = \sigma_{CRLB}^2(T_2)/T_2^2$ is defined and computed for a grid of relaxation times where T_1 values range from 1ms to 2000ms in 1ms steps and T_2 values range from 1ms to 120ms in increments of 1ms.

Experimental Validation

All images were obtained on a 3 Tesla Philips Achieva-TX (Philips Healthcare, Best, Netherlands) system with the manufacturer 32 channel receive adult head coil and processed from k-space raw data using the MRecon environment (Gyrotools LLC, Zurich). Experimental validation of the CRLB optimization was performed both on an in-house built spherical gel phantom and *in vivo*. The phantom consists of a 0.5% Agarose, 0.9% NaCl and 0.02mM $MnCl_2$ water solution with relaxation times $T_1^{Phantom} = 2200$ and $T_2^{Phantom} = 174ms$. $T_1^{Phantom}$ was mapped using single shot inversion recovery fast spin echo with k-space filled from low to high frequencies (minimizing T_2 effects) for inversion times of 107ms to 1857ms in increments of 125ms. Measurements were separated by a 20s gap in order to guarantee full M_z recovery. T_2 was obtained by multi-echo (CPMG) spin echo sampled at 32 echoes (each echo samples an image with different T_2-weighted contrast) with echo times ranging from 15ms until 480ms in increments of 15ms and a fixed T_R of 2000ms. In order to minimize imperfect refocusing contributions, only the even echoes were used to estimate T_2 decay [15], and both T_1 and

T_2 maps were estimated based on a least square criteria against their expected mono-exponential decay curves. *In vivo* data was imaged on a single female volunteer (age 22) which gave informed consent according to local ethics guidelines.

Both SPGR and bSSFP images were sampled as a sagittal acquisitions with a field of view of $250 \times 250 \times 250mm^3$ at $0.8mm^3$ isotropic resolution, on a Cartesian grid and a fixed bandwidth of 959Hz/pixel. In the interest of time, SENSE factor of 2 in both phase encode directions (Anterior-Posterior and Right-Left) was applied. Transmit field distributions were assessed with the AFI approach [45], with a $T_{R,1}/T_{R,2} = 25/125ms$ and maximum allowed gradient spoiling between each T_R [73], the field of view was set to match SPGR and bSSFP acquisitions and the acquired resolution was set to $3.91mm^3$ in all three dimensions. A linear relationship between prescribed and actual flip angle was assumed ($\theta_{actual} = \kappa\theta_{prescribed}$) in order to perform transmit field corrections on a voxel by voxel basis. bSSFP δB_0 correction was performed based on an acquired field map obtained as a dual echo gradient echo with $T_{E,1} = 2.3ms$ and $T_{E,2} = 4.6ms$, $T_R = 20ms$ and flip angle of 10°. Acquired field of view and sampling grid was matched with AFI acquisition described above.

More specifically for the *in vivo* case, prior to estimation of the relevant relaxation maps, FSL's standard tools [74] (`http://fsl.fmrib.ox.ac.uk`) for brain extraction (*bet*), registration (rigid 6 degrees of freedom alignment using *flirt*) and segmentation (3 tissue extraction using *fast*) were used.

4.2.2 Fitting Procedure

For all Monte Carlo simulations and experimental data acquired as defined above, parameter estimation was obtained using MatLab2016a *lsqnonlin* optimization routine from its optimization toolbox. Cost function was defined as the difference between measured data and expected signal models. Stopping criteria are defined as $< 10^{-15}$ change of cost function value or a maximum number of iterations of $100\times$ the number of estimation parameters.

4.3 Results: CRLB as an Optimization Tool

4.3.1 DESPOT1 estimation

Numerical Validation

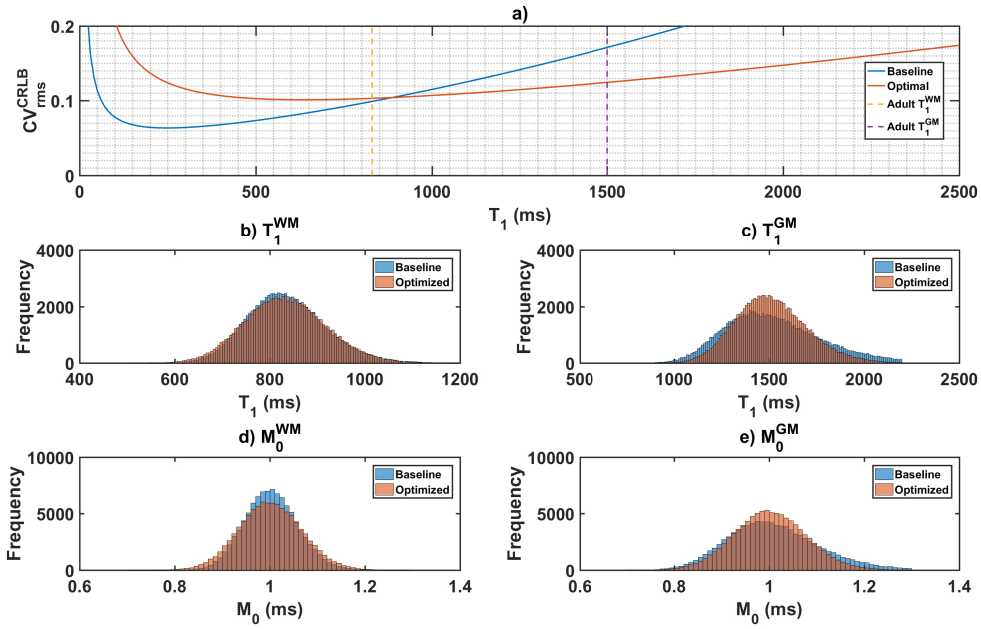

Figure 4.1: a) predicted estimation root-mean-square CV for both baseline (blue) and optimized(red) acquisition schemes. WM and GM T_1 are shown for reference. b-e) Monte Carlo comparison between considered baseline (blue) optimized (orange) DESPOT1 protocols. All graphs were obtained for an SNR of 20. Both M_0 (b) and c)) and T_1 (c) and e)) specific histograms are shown.

Optimal acquisition parameters obtained for the considered brain relaxation times correspond to flip angles $\theta_1 = 2.16°$ and $\theta_2 = 12.48°$ both with a T_R^{SPGR} of 6.2ms. The reader is invited to note that in spite of being allowed different T_R^{SPGR} values, interestingly, optimal solution converged to a situation where $T_{R,1}^{SPGR} = T_{R,2}^{SPGR}$. Figure 4.1 a) shows the predicted T_1 CV ($CV_{T_1}^{CRLB}$) as a function of T_1 for both baseline and adult optimal acquisition protocols. Assumed WM and GM T_1 values are highlighted for guidance. It is predicted that estimation CV of the Baseline protocol should be higher for relaxation times of less then $850ms$. The optimized protocol is expected to outperform the Baseline protocol for relaxation times larger then $850ms$. Monte Carlo validation results can be seen in Figure 4.1 b-e). Estimated WM and GM M_0 (respectively b) and d)), and T_1 (respectively c) and e)) for both the baseline and optimized acquisition protocols which are overlaid for comparison.

Experimental Validation - Phantom

Phantom specific optimized protocol was explored and obtained solution was found to be $T_{R,1}^{SPGR} = T_{R,2}^{SPGR} = 6.2ms$ with $\theta_1 = 1.8°$ and $\theta_2 = 10.3°$. Figure

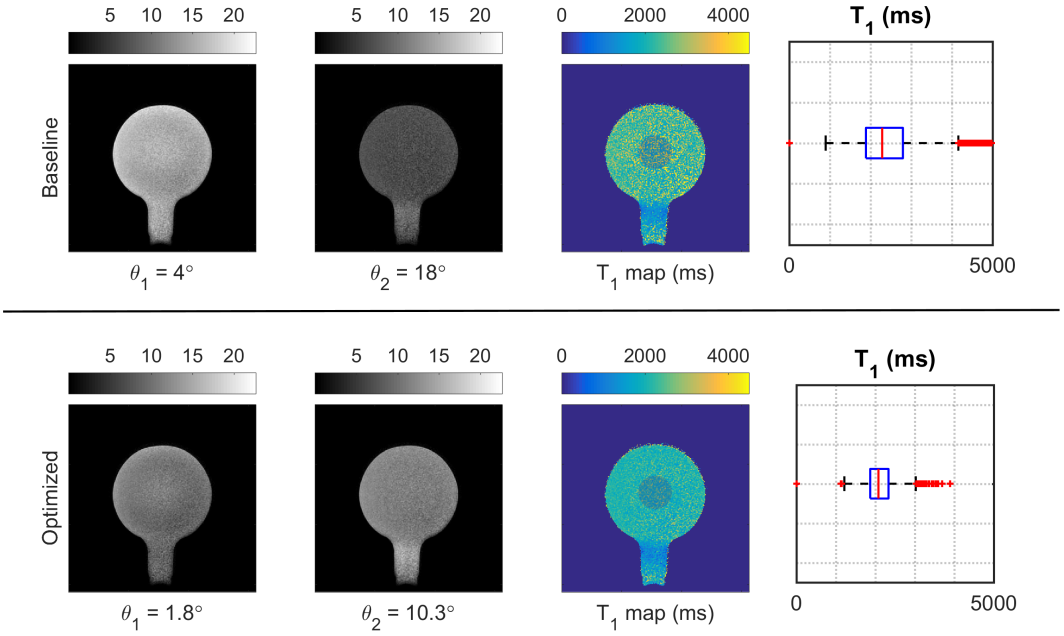

Figure 4.2: (Top) From left to right, Baseline acquisition exemplar slices of measured data, obtained T_1 distribution map and a box-plot summary of the highlighted ROI. (Bottom) Same as Top for optimized FA set.

4.2 from left to right compares sampled SPGR data, obtained T_1 map and a box-plot summary of the highlighted region of interest for both Baseline (Top row) and Phantom specific (Bottom row) protocols. Visual comparison between Baseline and Optimized Estimation maps demonstrates lower estimation variance of the Optimized flip angle set as a reduction of the ”grainy” texture of the final estimated map. The shaded area in estimated T_1 maps has been overlaid in order to highlight the selected region of interest used to extract the data used to generate the box-plot of the furthermost right column. Note that, for both box-plots, the x-axis is maintained fixed so that direct comparison between baseline and optimized protocols can be performed. A narrower distribution of T_1 values corresponds to a better estimation quality.

On a more quantitative note, the interquartile range of the baseline estimation is 922ms which is reduced to 446ms when applying the phantom optimized flip angle measurements. This corresponds to a 51.6% reduction in estimation interquartile range corroborating our hypothesis that the CRLB can be used as a criteria to improve relaxometry experiments by minimizing estimation variance of

the parameter of interest (i.e. T_1).

Experimental Validation - *In Vivo*

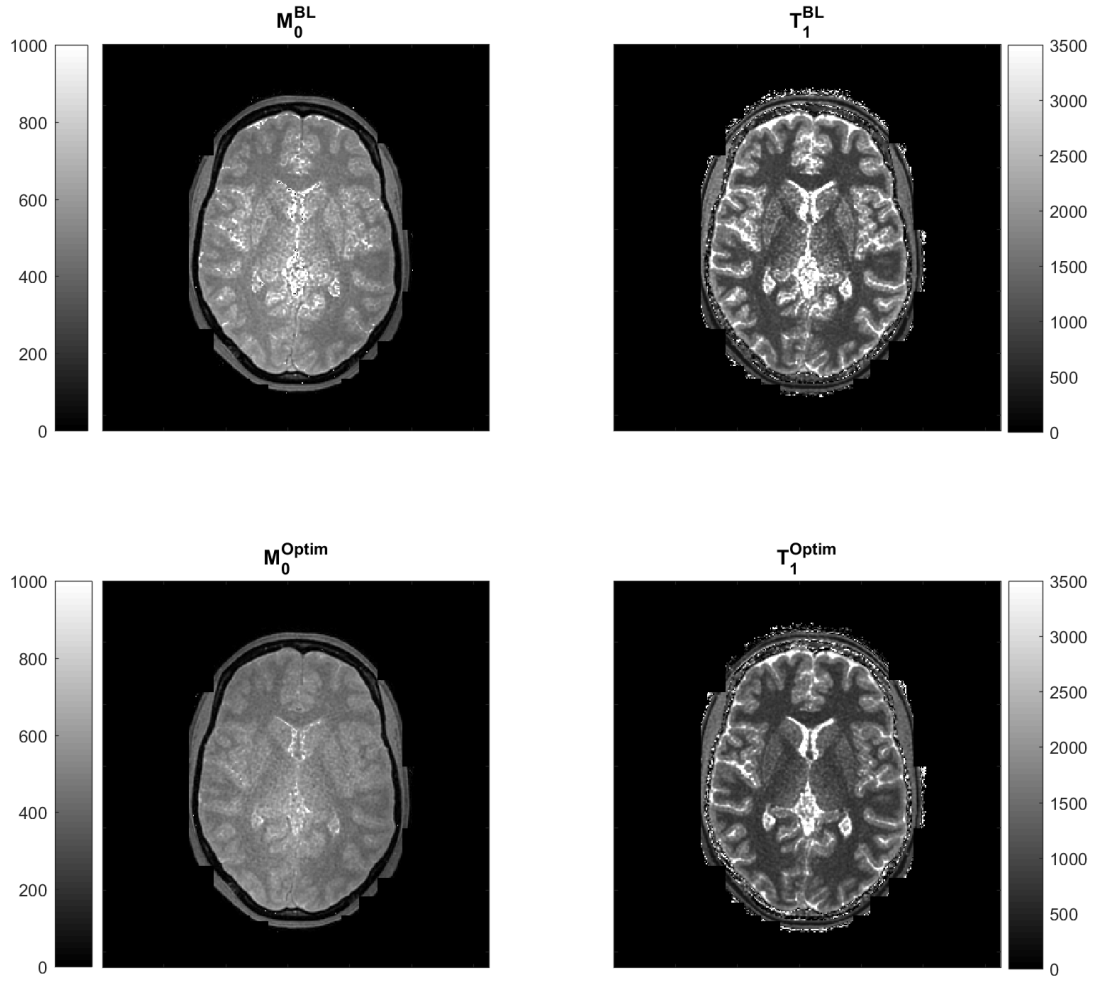

Figure 4.3: Exemplar axial slice comparison between estimated M_0 (left) and T_1 (right) distributions of both Baseline (top) and HV Optimized (bottom) acquisition protocols. Improvement of estimation precision can be qualitatively evaluated as optimal acquisition parameters induce a less "grainy" texture of the estimated maps.

In-vivo validation, compared the estimation maps using the considered baseline acquisition protocol and the CRLB optimised set of parameters. Exemplar M_0 and T_1 maps can be seen on the left and right of Figure 4.3 respectively. Top row corresponds to Baseline acquisition parameters while bottom row demonstrates estimated maps using CRLB optimized measurements. Visual inspection shows improvement of estimation quality specially in the centre of the brain where SNR levels are lower due to low receive sensitivities of the measurement coils.

Figure 4.4 demonstrates WM (left) and GM (right) specific T_1 histograms, normalized by WM and GM volume respectively, where Baseline (blue) and CRLB optimized (orange) protocols were used. Note that the same segmentation mask (after alignment) is used for both histograms and both higher hight and a smaller distribution width are a direct measurement of estimation quality improvement. Clear enhancement can be seen for the optimised flip angle set. Deviations of average T_1 estimated values can be observed between different *in-vivo* measurements which are much less significant compared to the ones observed on phantom experiment (see Figure 4.2) and are not expected from Monte Carlo simulations.

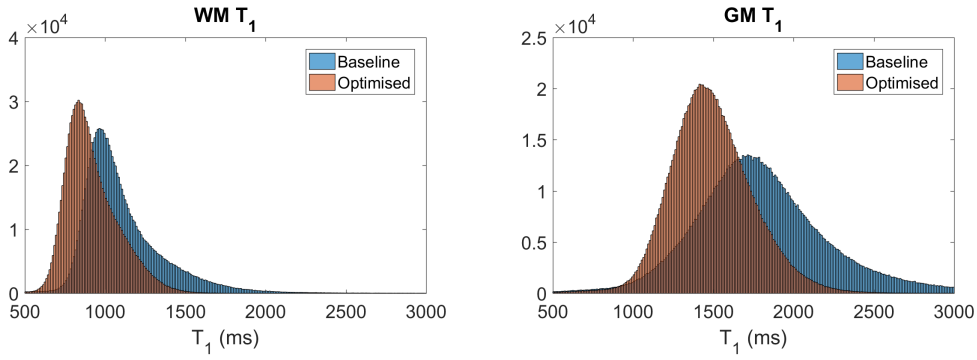

Figure 4.4: Comparison between Baseline (blue) and Optimised (orange) acquisition protocols. White matter specific (left) and Gray matter specific (right) and shown. A clear improvement in estimation precision can be observed for both WM and GM histograms. Systematic shift towards lower relaxation times is observed for the optimized protocol.

4.3.2 DESPOT2 estimation

Numerical Validation

Obtained optimal DESPOT2 estimation acquisition flip angles for *in vivo* measurements are respectively $\theta_1 = 10.6°$ and $\theta_2 = 55.9°$.

Left of Figure 4.5 demonstrates the predicted signal evolution as function of flip angle for both considered WM and GM relaxation times. Highlighted as dashed vertical lines are both baseline (yellow) and optimized (purple) protocols. bSSFP signal and CRLB are T_1 dependant therefore, we use the grid of T_1 and T_2 relaxation times as defined in the Methods section and plot (Right of Figure 4.5) the expected estimation CV defined as $\Delta\text{CV}_{T2} = 100 \times (\text{CV}_{T2}^{Optim} - \text{CV}_{T2}^{BL})/\text{CV}_{T2}^{BL}$. This grid is not to be confounded with the optimization grid used which corresponds to both WM and GM points highlighted as white and grey dots respectively. From

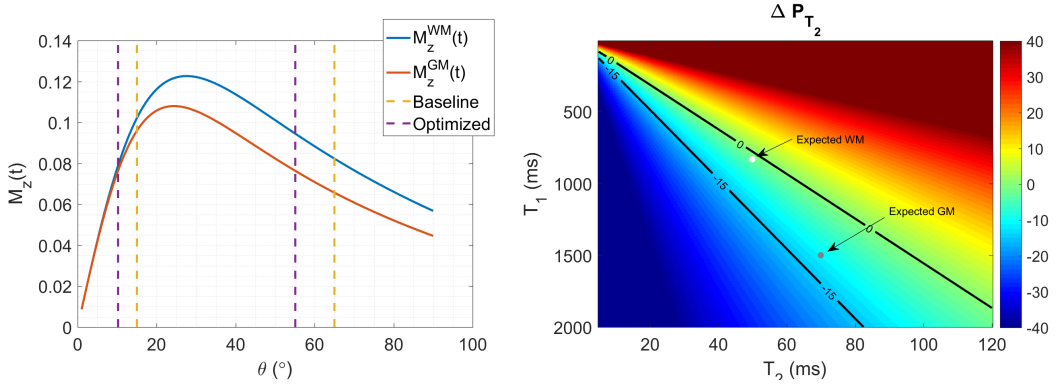

Figure 4.5: (Left) Comparison between WM and GM SSFP signal evolutions for different flip angles. Baseline and optimal flip angle set are shown for reference. (Right) Comparison of expected estimation CV difference ($\Delta\text{CV}_{T2} = 100 \times (\text{CV}_{T2}^{Optim} - \text{CV}_{T2}^{BL})/\text{CV}_{T2}^{BL}$) for a grid of different T_1 and T_2 relaxation times. WM (white dot) and GM (gray dot) expected relaxation times are highlighted. From here, it can be inferred, that minimum improvement is expected for WM T_2 estimation using optimized protocol. Mensurable benefit is expected for GM estimation.

Figure 4.5 enhanced estimation quality ($\Delta\text{CV}_{T2} < 0$) precision is expected for both tissue types. From here, it can be inferred, that minimum improvement is expected for WM T_2 estimation using optimized protocol. Mensurable benefit is expected for GM estimation.

Experimental Validation - Phantom

Phantom specific optimized protocol obtained was $\theta_1 = 13.3°$ and $\theta_2 = 68.4°$. This solution however is expected to induce minimal improvement since the expected change in variance is $< 1\%$, which although not exciting, experimental validation of this result still corroborates the agreement between prediction and experiment.

Figure 4.6 compares obtained estimated T_2 distributions in the same region of interested demonstrated in Figure 4.2. The proposed optimization framework was not able to find a set o flip angle measurements that would significantly improve T_2 estimation of the phantom which is corroborated by Figure 4.6.

Experimental Validation - *In Vivo*

As with DESPOT1, direct comparison between Baseline protocol and CRLB optimised protocol was performed and is summarised in Figures 4.7 and 4.8.

Exemplar M_0 and T_2 maps can be seen on the left and right of Figure 4.7 re-

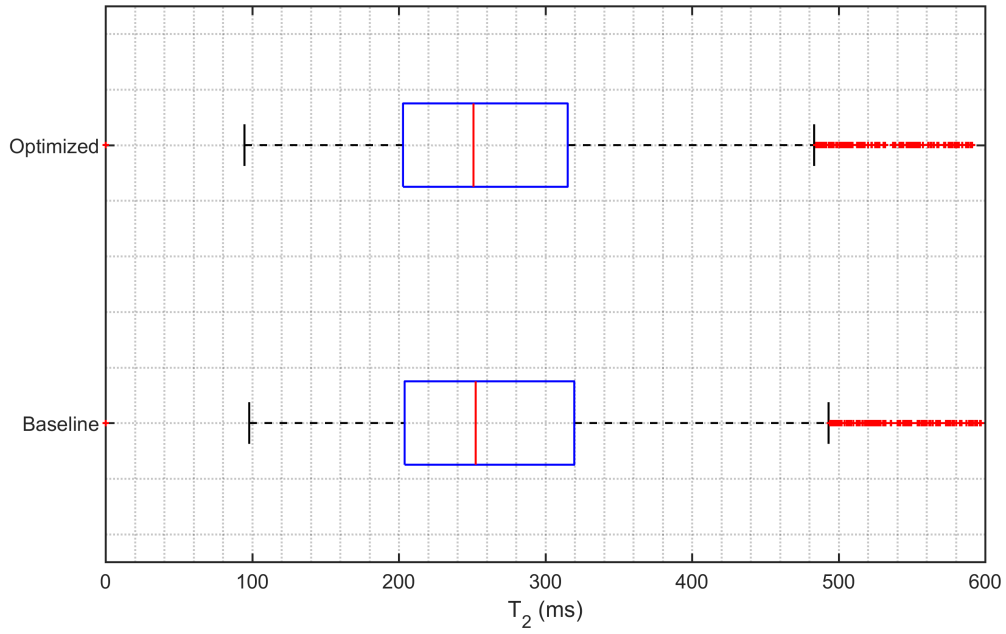

Figure 4.6: Box and whiskers plot comparison of DESPOT2 estimation using Optimized (Top) and Baseline (Bottom) set of acquired flip angles.

spectively. Top row corresponds to Baseline acquisition parameters while bottom row demonstrates estimated maps using CRLB optimized measurements. Both were estimated assuming T_1 map acquired with Baseline DESPOT1 protocol as correct T_1 value. Note that from Figure 4.5 it was expected minimal to no improvement in WM estimation while significant improvement is expected in GM. This can be verified in Figure 4.8 where direct comparison between baseline and CRLB optimised protocol is performed for WM (left) and GM (right). Also, contrary to T_1 estimation, no bias in distribution is shown between baseline and optimized acquisition protocol.

4.4 Discussion

This chapter sought to demonstrate how the CRLB can be used as a robust design tool to improve DESPOT-type relaxometry estimation.

DESPOT1 phantom experiment (Figure 4.2) shows a 51% improvement in estimation quality, compared to baseline measurement, when a phantom specific optimization protocol is designed. This shows that the proposed CRLB approach allows relaxation time specific optimization. This is further validated on *in vivo* T_1 estimation (4.4) where visual assessment of the obtained relaxation maps show

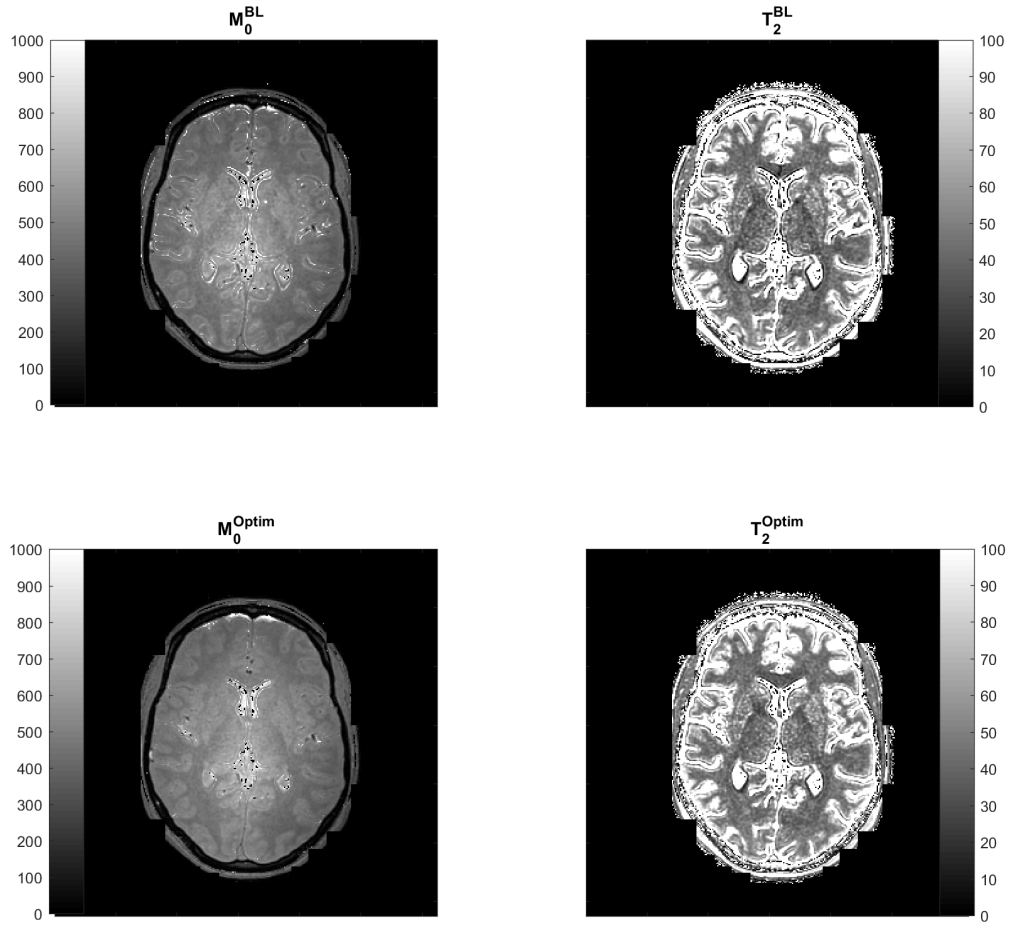

Figure 4.7: Exemplar axial slice comparison between estimated $M_0(a.u)$ (left) and $T_2(ms)$ (right) distributions of both Baseline (top) and HV Optimized (bottom) acquisition protocols. Both maps are estimated assuming T1map acquired with Baseline DESPOT1 protocol.

significant improvement in precision specially for deep GM tissue parameters which is in good agreement with the prediction of Figure 4.1 (longer relaxation times are expected to benefit more from the optimized flip angle set). Significant bias can be observed between baseline and optimized estimation protocols. Numerical simulations, such as the ones in Figure 4.1, suggest that minimal-to-no bias should occur when applying different flip angle measurements. We attribute this to magnetization transfer effects, whose exploration are outside the scope of this chapter and will be further investigated in chapter 6.

Regarding T_2 estimation based on DESPOT2 method, it was not possible to find a set of flip angles measurements that would significantly improve T_2 estimation for the phantom. Although Figure 4.6 demonstrates the small expected improvement in precision, it is from Figure 4.8 the validation of the proposed op-

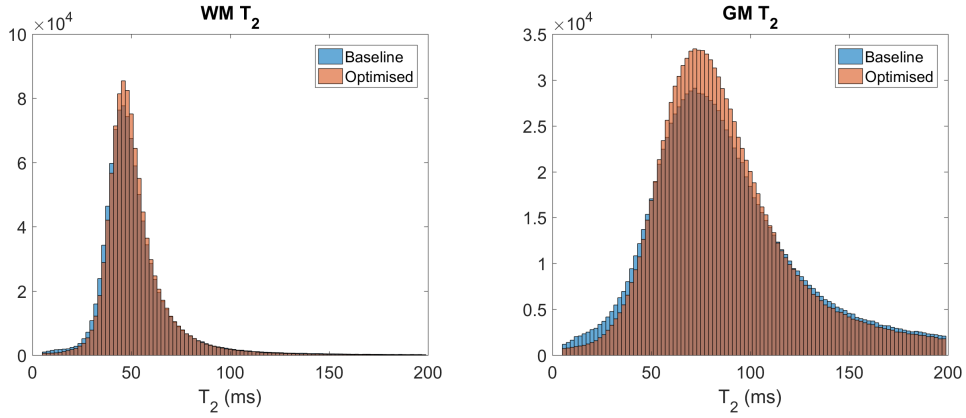

Figure 4.8: Comparison between Baseline (blue) and Optimised (orange) acquisition protocols. White matter specific (left) and Gray matter specific (right) and shown.

timization framework is corroborated. From Figure 4.5 negligible improvement is expected for WM T_2 estimation and some improvement is expected for GM. This can be clearly seen in Figure 4.8 where both WM and GM specific histograms are displayed for both Baseline (blue) and Optimized flip angle set (orange), corroborating the agreement between CRLB prediction and obtained experiment. The reader is invited to notice, that regarding T_2 estimation, no bias is shown between both acquisition protocols (in contrast with T_1). Also, note that the same Baseline T_1 maps was used in order to mitigate the effect of noise propagation in the performed comparison.

Previous studies, such as the ones presented in [4] and [75], have proposed alternative methods to optimize DESPOT1 and DESPOT2 relaxometry although they usually focus on a single tissue of interest (WM). The main advantage of the proposed CRLB approach is its flexibility to be extended to any number of tissue types of interest. This might be of interest for designing clinical studies for clinical conditions, such as multiple-sclerosis, where T_1 and T_2 values of interest may not be necessarily the same as the ones expected in healthy volunteers WM and GM.

4.5 Conclusion

The work presented in the current chapter proposed and validated the use of the Crámer-Rao Lower Bound as a design tool for DESPOT-type relaxometry. The main advantage of this optimization approach is that it allows several tissues of interest to be simultaneously evaluated which may prove useful for studies where both WM and GM are of interest, or significant deviations in average relaxation time values are expected.

Chapter 5

Joint System Relaxometry - JSR

The concepts presented in this chapter are a novel scientific contribution which has been peer-reviewed and published in [11]. More specifically, the Joint System Relaxometry (JSR) is introduced as a framework where multiple signal models sensitive to common MR parameters are simultaneously evaluated in order to better constraint estimation of the same parameters.

5.1 Introduction

In the previous chapters a description of current DESPOT-type methods to estimate single compartment relaxation parameters (T_1 and T_2) was given as well as a proof of concept on the CRLB application to optimize them. Recently, multi-component signal models have also been proposed [8, 76, 77] and an interesting discussion regarding their estimation stability based on both Monte Carlo [77] or Cramér-Rao Lower bound (CRLB) methods [9] can be found elsewhere [9, 77, 78].

The work presented in this chapter is divided in two main topics. Firstly, the concept of JSR is introduced where multiple signal models sensitive to same MR parameters are simultaneously evaluated in order to better constraint the estimation procedure towards the correct solution. More specifically, we have focused in adopting the full (i.e. not linearised) models for both SPGR and SSFP signals in order to maximize the information available to correctly constrain the obtained solution. Secondly, we apply the CRLB framework proposed in Chapter 4 to optimize the JSR estimation. This allows the selection of optimized acquisition protocols for specific tissues of interest.

In summary, the current chapter has compared the proposed JSR methodology with currently established methods, used the CRLB framework to determine optimal acquisition strategies for adult brain relaxometry, tested the resulting framework on a phantom and *in vivo* to determine the performance benefits that can be achieved and explored if this approach can impact on the reported over-estimation of relaxation parameters in the single compartment model.

5.2 Theory

For the work presented in this chapter we've adopted the convention that all signals are normalised by the proton density, M_0, as all measured signals have a scanner dependent scaling factor that must be explicitly accommodated during fitting (see methods section). With this in mind, Equations 2.47 and 2.48 to 2.51 were redefined such as:

$$S_{SPGR}(\alpha, T_R^{SPGR}) = \frac{1 - E_1(T_R^{SPGR})}{1 - E_1 \cos(\kappa\alpha)} \sin(\kappa\alpha) e^{\frac{-T_E^{SPGR}}{T_2}} e^{\frac{-T_E^{SPGR}}{T_2'}} e^{-i2\pi\Delta\Omega T_E^{SPGR}} \tag{5.1}$$

$$S_{SSFP}(\alpha, T_R^{SSFP}) = [M_x^{SS}(\alpha, T_R^{SSFP}) + iM_y^{SS}(\alpha, T_R^{SSFP}] e^{\frac{-T_E^{SSFP}}{T_2}} e^{-i2\pi\Delta\Omega T_E^{SSFP}} \tag{5.2}$$

where,

$$M_x^{SS}(\alpha, T_R^{SSFP}) = (1 - E_1(T_R^{SSFP})) \frac{E_2(T_R^{SSFP}) \sin(\kappa\alpha) \sin(\beta)}{d} \tag{5.3}$$

$$M_y(\alpha, T_R^{SSFP}) = (1 - E_1(T_R^{SSFP})) \frac{(1 - E_2(T_R^{SSFP}) \cos(\beta)) \sin(\kappa\alpha)}{d} \tag{5.4}$$

with,

$$\begin{aligned} d =& (1 - E_1(T_R^{SSFP}) \cos(\kappa\alpha))(1 - E_2(T_R^{SSFP}) \cos(\beta)) \\ & - E_2(T_R^{SSFP})(E_1(T_R^{SSFP}) - \cos(\kappa\alpha))(E_2(T_R^{SSFP}) - \cos(\beta)) \end{aligned} \tag{5.5}$$

Equations 5.1 to 5.5 summarize the full magnetization description which we refer as Joint System Relaxometry (JSR) to distinguish from the commonly used sequential approach. T_R^{SPGR}, T_E^{SPGR}, T_R^{SSFP} and T_E^{SSFP} are respectively the repetition and echo times of SPGR and SSFP acquisitions. T_2' follows the common definition $1/T_2^\star = 1/T_2 + 1/T_2'$. The flip angle α is modulated by the dimensionless transmit field inhomogeneity κ, $E_1(T_R^{SPGR,SSFP}) = \exp(-T_R^{SPGR,SSFP}/T_1)$ and $\beta = 2\pi\Delta\Omega T_R^{SSFP} + \Phi_{RF}$ is the off-resonance dephasing angle in radians resulting from the frequency offset $\Delta\Omega(Hz)$ plus the rotation induced by incrementing the

phase Φ_{RF} of the RF pulse at each T_R^{SSFP} [12]. Finite duration of the RF pulse (T_{RF}) was considered by following the correction proposed in [57, 79] and defining $E_2 = \exp(-(T_R^{SSFP} - \zeta_\beta \frac{T_{RF}}{T_R^{SSFP}})/T_2)$, with $\zeta_\beta = \zeta \cos^2([\frac{\beta}{2}(1-(1-\zeta)\frac{T_{RF}}{T_R^{SSFP}})])$ and $\zeta \approx 0.68 - 0.125(1 + \frac{T_{RF}}{T_R^{SSFP}})\frac{T_2}{T_1}$. The reader is invited to note that SPGR and SSFP are not required to have equal repetition and echo times.

The proposed JSR approach requires careful balance between SPGR and SSFP signal intensities during readout periods. Although possible to compute the echo-time decay from the magnetization prior to the RF-pulse, using the magnetization immediately after the excitation pulse allows a simple exponential decay to be added to the steady-state solution. This is contrary to the approach described by Deoni in 2009 [54], where the steady-state magnetization immediately before each RF pulse was considered. The $\exp(-T_E^{SPGR}/T_2')$ term is present in the SPGR and not in the SSFP sequence model which is a consequence of the latters spin-echo behaviour as described in [30].

Equation 5.1 is only valid if perfect spoiling of the transverse magnetization is attained before each RF pulse. This is easily obtained for $T_R^{SPGR} >> T_1$, however, RF and gradient spoiling methods need to be applied when $T_R^{SPGR} << T_1$ [6, 44]. A good discussion of this issue is presented in [44] and the reported value of 50° as stable RF-phase increment is assumed (see Chapter 3); no further correction to the apparent T_1^{app} obtained is applied. However, the obtained steady state is still $T_R SPGR$, T_1, T_2 and FA dependent. To ensure that imperfect spoiling was kept under control, the SPGR sequence was modelled using the extended phase graph algorithm (EPG) [19, 73] including attenuating effects associated with diffusion resulting from both imaging and spoiler gradients. Choice of FA and T_R was then constrained to ensure a peak error of $\leq 5\%$ compared to the ideal Ernst regime for relevant T_1 and T_2 ranges (See Figure 3.8 in Chapter 3).

5.3 Methods

All simulations and off-line post-processing were performed using MatLab 2016a (The MathWorks Inc., Natick). Equations 5.1 to 5.5 were defined as being normalised by M_0, effectively defining them with respect to unit proton density. To fit the JSR model, which is the concatenation of the SPGR and SSFP signal models set out in equations 5.1 to 5.5, to actual image data it is necessary to take account of the strength of the signals found in each voxel. This is proportional to M_0, scaled by an arbitrary position dependent complex gain, $Ae^{-i\phi_A}$, which can

be attributed to receive sensitivity including all sources of incidental phase.

$$JSR = Ae^{-i\phi_A} M_0 [S^1_{SPGR}, ..., S^{N_{SPGR}}_{SPGR}, S^1_{SSFP}, ..., S^{N_{SSFP}}_{SSFP}] \tag{5.6}$$

Since it is not possible to separate the different contributions to this compound scaling factor, we define a complex weighted proton density $\rho = Ae^{-i\phi_A} M_0 = \rho^r + i\rho^i$. This formulation keeps the SSFP model and acquisitions everywhere differentiable, which is not the case in their characteristic stop-band areas when using magnitude images, allows $\Delta\Omega$ to be directly estimated from the image data and retains a Gaussian image noise distribution. The SPGR acquisitions may contain additional phase factors, which might require an extra parameter to fit that is not needed for relaxation time determination. We therefore discard the SPGR image phase by taking the magnitude and enforcing $\rho_{SPGR} = |\rho| = \sqrt{(\rho^r)^2 + (\rho^i)^2}$ resulting in the final considered JSR model of Equation 5.7.

$$\begin{aligned} JSR_{final} = &[|\rho| S^1_{SPGR}, ..., |\rho| S^{N_{SPGR}}_{SPGR}, \\ &Re(\rho S^1_{SSFP}), Im(\rho S^1_{SSFP}), ..., Re(\rho S^{N_{SSFP}}_{SSFP}, Im(\rho S^{N_{SSFP}}_{SSFP}))] \end{aligned} \tag{5.7}$$

Where real (Re) and imaginary (Im) signals are concatenated in order to keep the cost function real valued. For this approach it is important that the signal to noise ratio (SNR) of each SPGR image set is sufficient to avoid significant Rician bias. This was empirically confirmed by using Matlabs Kolmogorov-Smirnov test to check for normal distributions on WM and GM segmented SPGR images.

For both simulation and optimisation a grid of T_1 and T_2 pairs were used covering the relevant ranges for brain, from 600 to $1200ms$ in steps of $25ms$ for T_1 and 25 to $80ms$ in increments of $5ms$ for T_2. Although estimated, cerebral spinal fluid relaxation times have been excluded from the optimization since it is difficult to guarantee correct spoiling of the magnetization and are, usually, of less clinical interest. Optimising the measurement to estimate the higher T_1, T_2 values of CSF could diminish precision for brain tissue while not achieving any valid measurement The proton density was given the value 10 in arbitrary units with zero phase (i.e. $\rho^r = 10$ and $\rho^i = 0$). Although not necessary, for ease of guaranteeing equal sampling conditions between acquisitions such as bandwidth and geometrical distortions, $T_E^{SPGR} = T_E^{SSFP} = 0.5T_R^{SSFP}$ was enforced. Further, due the short readout times used in this work (see below), SPGR T_2' signal deviations were neglected. This is justified since, for typical frontal white matter $T_2' = 285ms$ [80], induced signal deviations of not considering $e^{-T_E^{SPGR}/T_2'}$ are less then 1%.

All images were obtained on a 3 Tesla Philips Achieva-Tx (Philips Healthcare, Best, Netherlands) system with the manufacturer 32 channel receive adult head coil and processed from k-space raw data using the MRecon environment (Gyrotools LLC, Zurich, Switzerland). To assure equal RF pulse duration T_{RF} between each flip angle measurement of each respective sequence (SPGR or SSFP), the scanner software was modified to force a fixed pulse duration that is determined by the largest FA required with all other FA obtained by varying the pulse amplitude only. Non-linearity of RF-amplifier was corrected by enforcing a vendor calibration step which allows pre-emphasis of the RF-shape. VFA data was sampled as a sagittal acquisition with a field of view of $250 \times 250 \times 250mm^3$ at $0.8mm^3$ isotropic resolution, fixed bandwidth of 959Hz/pixel and SENSE factor of 2 (Anterior-Posterior) and 2 (Right-Left) in both phase encode directions for both in vivo and phantom measurements. SPGR spoiling area was kept at the default values optimized by the manufacturer software which result on total phase dispersion of approximately 7 radians per voxel in the readout direction. Non-selective excitation pulses were used for all 3D measurements. Correct knowledge of transmit field (B_1) distribution is assumed as it can be assessed with mapping techniques [45, 46, 48, 73] which are not the main focus of this paper. They were experimentally assessed with the AFI approach [45, 46] with $T_{R1}/T_{R2} = 25/125ms$ and maximum allowed gradient spoiling between each T_R, the field of view was set to $250 \times 250 \times 250mm^3$ for an acquired isotropic resolution of $3.91mm^3$ resulting in a total acquisition time of 2 minutes. A linear relationship between prescribed and actual flip angle was assumed ($\alpha_{actual} = \kappa\alpha_{prescribed}$) in order to perform transmit field corrections.

Parameter estimates of each measured voxel $\Theta_{JSR} = [\rho^r, \rho^i, T_1, T_2$ and $\Delta\Omega]$ are obtained through fitting of Equation 5.7 based on a least-square criteria using MatLab2014b *lsqnonlin* routine. The objective function was defined as the sum of the square difference between the model and the measured signal intensity, the stopping criteria were set as 10^{-15} tolerance on the cost function value or to a maximum of 500 iterations. The optimization initial conditions were kept fixed for all estimated voxels and chosen as the expected average relaxation time in the entire brain from pilot data acquired while setting up this study. For all experimental estimation, each imaged voxel was independently processed on a Intel Xeon CPU E5-2687W 0 @ 3.10GHz parallelized to 16 cores taking a total computational time between 6 and 7 hours depending on the extracted brain volume.

For comparison purposes linearised estimations of ρ_1, T_1 were obtained using the DESPOT1 approach as described in [4] and then ρ_2, T_2 and $\Delta\Omega$ were

estimated using the DESPOT2-FM [54] with finite RF pulse correction [57, 79]. Furthermore, a baseline DESPOT1/2 protocol was adapted from [54] and consists of two SPGR (DESPOT1 $\rightarrow$ FA = $4°$ and $18°$, $T_R^{SPGR} = 6.2ms$) and four SSFP (DESPOT2 $\rightarrow$ FA = $15°$ and $65°$, $T_R^{SSFP} = 4.2ms$ for $\phi_{RF} = \pi, 0rad$) measurements resulting in a total acquisition time of 9 minutes and 18 seconds.

5.3.1 CRLB Numerical Validation

Validation that the CRLB is able to accurately predict JSR estimation quality was performed via a Monte Carlo simulation using the values of ρ, T_1 and T_2 defined above. For each element of the resulting grid, 1×10^5 independent trials were generated. Gaussian distributed noise with zero mean and a standard deviation $\sigma = 0.02|\rho|$ [9] was added to both real and imaginary parts of each signal.
For each T_1 and T_2 combination the standard deviation σ of the Monte Carlo simulation as well as the predicted CRLB σ_{CRLB} for both relaxation times were extracted. For comparison each value was normalized by its respective relaxation time defining, Monte Carlo and σ^2_{CRLB} precisions as $p^{\sigma}_{T_{1,2}} = \sqrt{(\sigma_{T_{1,2}})^2/T^2_{1,2}}$ and $p^{CRLB}_{T_{1,2}} = \sqrt{(\sigma_{CLRB_{T_{1,2}}})^2/T^2_{1,2}}$ respectively.

5.3.2 Phantom Validation

Phantom validation was performed by imaging an in-house built spherical phantom filled with a 0.5% Agarose, 0.9% NaCl and 0.02mM MnCl2 solution and mainly focused on two goals:

1. Validation of estimation improvement based on JSR fitting approach
2. Validation of the CRLB framework as a protocol design tool

Comparison between conventional two step fitting approach and proposed JSR is performed based on the baseline protocol. Both DESPOT1/2 and JSR estimation maps were obtained using the same measured data with the procedure described above. For reference purposes, spin echo measurements were performed within a single slice with a FOV of $250 \times 250mm^2$ and an acquired voxel size of $1.6 \times 1.6 \times 4mm^3$. T_1 was mapped using single shot inversion recovery TSE with k-space filled from low to high frequencies (minimizing T_2 effects) for inversion times of $107ms$ to $1857ms$ in increments of $125ms$. Each measurement is separated by a $20s$ gap in order to guarantee full T_1 recovery. T_2 was obtained by multi-echo TSE sampled at 32 echoes with echo times ranging from $15ms$ until $480ms$ in increments of $15ms$ and a prescribed $T_R = 2000ms$. In order to minimize imperfect refocusing contributions, only the even echoes were used to

estimate T_2 decay and both T_1 and T_2 maps were estimated based on a least square criteria against their expected mono-exponential decay curves [6, 12]. Although spin-echo methods may sometimes be described as gold-standard, in the present context we note that they provide a robust means of estimating relaxation parameters by a completely different approach to the one under investigation and so provide an independent point of reference. However, this distinctiveness may also lead to discrepancy with the family of methods under test. The magnetisation transfer ratio (MTR) was also measured using the standard Philips product sequence Transverse acquisition with voxel size of $1 \times 1 \times 2$ for a FOV of $224 \times 168 \times 120$, sinc-shaped preparation with 19.3ms duration, maximum amplitude of 12.2 μT and off-resonance of 1100Hz.

In order to validate the proposed CRLB framework a phantom specific VFA protocol was designed (see below) and estimation compared to considered baseline protocol.

5.3.3 Optimizing JSR

In this work it is proposed that CRLB can be used as a criterion to select optimal JSR acquisition parameters FA, $T_R^{SPGR,SSFP}$ and ϕ_{RF}. To achieve this Equation 4.8 was minimized making use of the pattern search optimization routine, implemented in MatLab2015b *optimtool*. The standard T_1 and T_2 grid defined above was covered and combined with field offsets ranging from δB_0 of $-125Hz$ to $125Hz$ in increments of 1Hz. Note that this routine is not guaranteed to find global optima, however we repeat the optimization for 10 randomly distributed values of flip angles (FA), $T_R^{SPGR,SSFP}$ and ϕ_{RF}. The global optimum, if not obtained, is not expected to dramatically improve the estimation quality compared to the solution achieved as in practice several of the solutions found have a cost-function value which demonstrate similar performance.

Imaging time is a limiting factor and it is possible to improve performance simply by imaging for longer (i.e. at the expense of efficiency). When working at fixed resolution (taken to be the same for all of the contributing acquisitions) with only one average, the total imaging time is simply proportional to the sum of the T_R of the individual sequences in the protocol. For the considered baseline protocol [76] $T_{total} = 29.2ms$ which was fixed for all solutions explored. Within this constraint, the number of SPGR (N_{SPGR}) and SSFP (N_{SSFP}) measurements can be varied along with the T_R, ϕ_{RF} and FA for each acquisition. Solutions can be calculated

using different values of T_R for each acquisition, however, early exploratory work showed that the optimal acquisitions always converged for $T_R^{SSFP} = \min T_R$ thus, for simplicity we constrained SSFP to have minimum T_R. The minimum sequence T_R, depends on resolution and particularly FA (SAR constraints), but is otherwise the same for both SPGR and SSFP on our system. Allowing for a suitable range of flip angles, we set $T_{R_{min}} = 4.2ms$, and this then set the maximum possible number of acquisitions in the permitted T_{total}. T_R^{SPGR} is allowed to freely vary subject to $\sum T_R^{SPGR} + N_{SSFP} T_R^{SSFP} \leq T_{total}$, where an explicit sum is written because both the number of SPGR sequences and their individual repeat times are varied. There are five unknowns to be estimated (Θ_{JSR} =[ρ^r, ρ^i, T_1, T_2 and $\Delta\Omega$]), therefore, a minimum of 5 measurements are required for a fully determined solution. Also, given that we operate with equal echo times for all acquisitions a minimum of 2 SSFP measurements is always required in order to estimate the field map $\Delta\Omega$.

Optimal T_R, ϕ_{RF} and FAs were thus determined for different combinations of N_{SSFP} and N_{SPGR} as expressed in the following table (greyed out cells are excluded as infeasible):

		N_{SSFP}				
		1	**2**	**3**	**4**	**5**
N_{SPGR}	**1**				✓	✓
	2			✓	✓	✓
	3		✓	✓	✓	
	4		✓	✓		

Figure 5.1: Description of the optimization options explored within the time constrain explored. Grey areas were not considered in the optimization search.

‘

5.3.4 *In Vivo* Validation

In-vivo scans were acquired in 4 healthy volunteers (2 male, 2 female, mean age 27yrs, min = 20 - max = 31 yrs), who gave written informed consent according to

local ethics requirements.

Each subject was imaged using the complete baseline protocol and an optimized set of parameters obtained by making use of the proposed CRLB optimization framework. The optimised parameters are listed in the Results section.

Prior to relaxation maps estimation all images were skull striped and aligned using standard FSL *bet* and *flirt* tools (*www.fsl.fmrib.ox.ac.uk*) [74, 81, 82]. An automatic segmentation was also performed on the T1 weighted SPGR image using FSL *fast* tool [74, 81, 82].

Individual T_1 and T_2 histograms were calculated in order to compare estimation performance between baseline and optimized protocols [6, 83].

5.4 Results

5.4.1 CRLB Numerical Validation

Figure 5.2 shows a comparison of the JSR CRLB ($p_{T_{1,2}}^{CRLB}$) and Monte Carlo predicted precision ($p_{T_{1,2}}^{MC}$) for the baseline protocol for the full grid of brain relaxation times. The relative percentage difference between $p_{T_{1,2}}^{CRLB}$ and $p_{T_{1,2}}^{MC}$ is defined as $\epsilon_{T_1}^{MC-CRLB} = (p_{T_{1,2}}^{MC} - p_{T_{1,2}}^{CRLB})/p_{T_{1,2}}^{CRLB}$ is below 1% as can be observed in the right column of Figure 5.2.

5.4.2 Phantom Validation

The phantom had $T_1 = 2058 \pm 27ms$ and $T_2 = 185 \pm 1ms$ as determined using the reference spin echo sequences and MTR=$5.8\% \pm 0.7\%$. Phantom data was used to validate the hypothesis that JSR precision outperforms the standard DESPOT1/2 approach and allowed the proposed CRLB framework to be tested. To achieve this, an extensive set of phantom specific optimised acquisition protocols (Figure 5.1) were obtained using the CRLB framework and the two best protocols are reported in Figure 5.4 together with the baseline parameters for comparison. These three protocols were acquired in the same scanning session and the respective T_1 and T_2 distributions inside a 10mL region at the centre of the phantom are compared in the box-plots of Figure 5.4. For reference, a blue dotted line is drawn that marks the T_1 and T_2 values obtained using spin echo

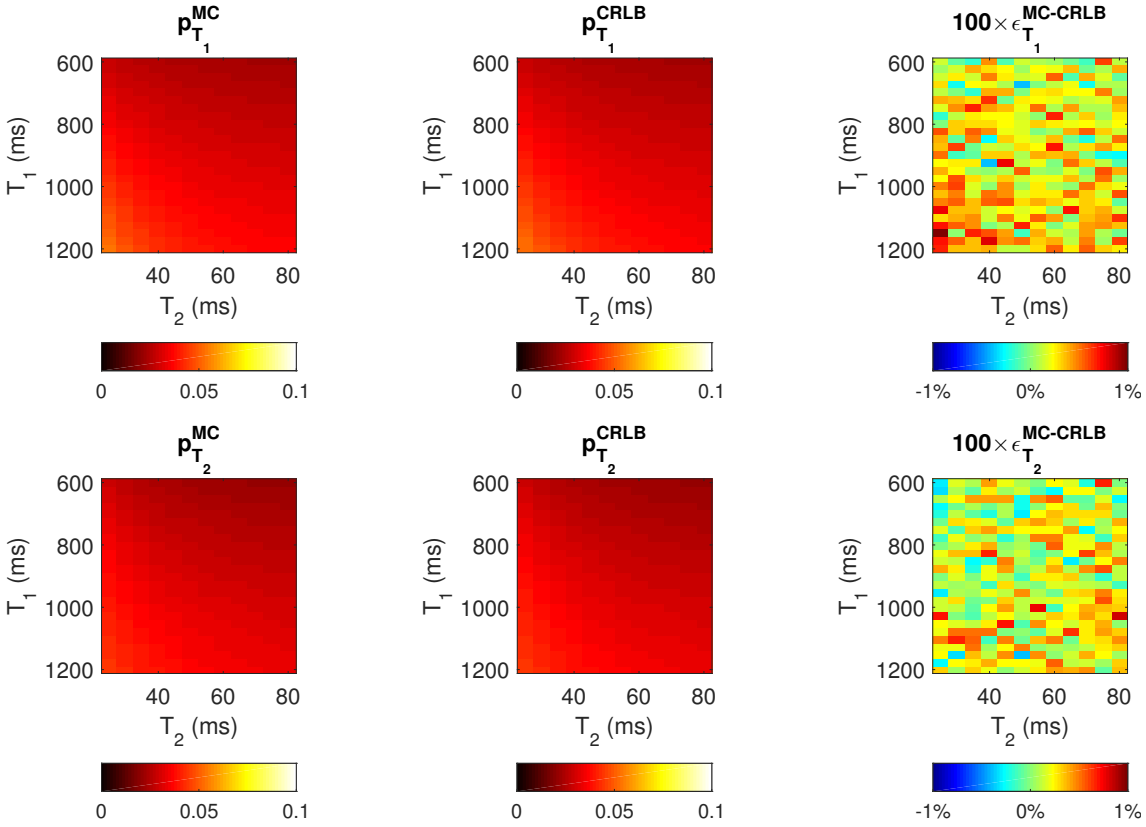

Figure 5.2: Comparison between σ^2_{MC} (Left Column) and CRLB simulations (Middle Column) predicted precisions for different T_1 and T_2 relaxation times combinations. The rightmost column represents the percent different between $p^{CRLB}_{T_1}$ and $p^{MC}_{T_1}$ predictions ($\epsilon^{MC-CRLB}_{T_1}$).

based estimation.

Conventional two-step fitting approach on the Baseline protocol results in interquartile range estimations of 1162ms for DESPOT1 T_1 and 111ms for DESPOT2-FM T_2. Significant improvement is achieved by performing the proposed JSR approach on the same data, with interquartile ranges reduced to 323ms for T1 and 26ms for T_2. Further improvement is obtained by making use of the proposed CRLB optimization framework. JSR-1:4 and JSR-2:4 interquartile T_1 range are reported respectively as 220ms and 200ms, reductions of 32% and 38% respectively. Similar improvement can be observed in T_2 estimation where JSR-1:4 and JSR-2:4 interquartile ranges are respectively 14ms and 15ms (46% and 43% reductions). Percentage deviation of the median value relative to the reference spin echo measurement DESPOT1, JSR Baseline, JSR 1:4 and JSR 2:4 demonstrate respectively 15.1%, 11.0%, 3.3%, 4.4% bias. On the same note, percentage deviation is reported as 20.7% for DESPOT2-FM, 10.9% for JSR Baseline, -11.4% for JSR 1:4 and -9.2% for JSR 2:4.

N_{SPGR}:N_{SSFP}		SPGR		SSFP				
2:4(Baseline)	α^{SPGR}(°)	4.0	18.0	15.0	65.0	15.0	65.0	α^{SSFP}(°)
	T_R^{SPGR}(ms)	6.2	6.2	180	180	0	0	ϕ_{RF}(°)
1:4	α^{SPGR}(°)	11.0		59.1	16.0	14.9	54.7	α^{SSFP}(°)
	T_R^{SPGR}(ms)	12.4		281	100	261	77	ϕ_{RF}(°)
2:4	α^{SPGR}(°)	8.9	6.4	15.1	15.9	56.1	51.5	α^{SSFP}(°)
	T_R^{SPGR}(ms)	8.2	4.2	97	258	288	73	ϕ_{RF}(°)

Figure 5.3: Phantom Specific Acquisition Protocols. Colour bar represents fraction of time SPGR (orange) and SSFP (blue) occupy in each protocol. Gel Optimized solutions where obtained for expected T_1 and T_2 values previously assessed via spin echo methods.

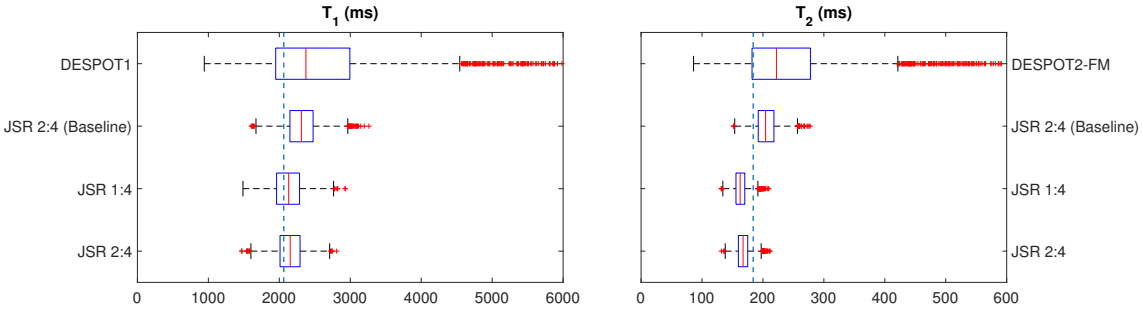

Figure 5.4: Box and whisker plots comparing T1 and T2 distributions within a 10-mL region of interest, estimated using each of the acquisition protocols defined in Table . Each acquisition protocol is identified by the number of SPGR:bSSFP measurements. Baseline corresponds to the acquisition protocol adapted from [54]. Vertical lines show the average spin echo measured T1 and T2. Parameter estimation by DESPOT was processing for the baseline protocol only or JSR, as indicated.

5.4.3 Optimizing JSR

SPGR acquisitions have been criticized for their sensitivity to incorrect/imperfect spoiling of transverse magnetization prior to each excitation pulse [15, 58, 83]. In order to mitigate source of bias, EPG simulations of the SPGR signal response for parameters of interest were compared to the ideal Ernst relationship assumed in this chapter. For reference, Figure 3.9 (Chapter 3) demonstrates the expected percentage signal error $\epsilon = (S_{spgr} - S_{spgr}^{EPG})/S_{spgr}^{EPG}$ for both WM ϵ_{WM} and GM ϵ_{GM} as a function of different T_R^{SPGR} and FA α_{SPGR}. Solutions which would induce a WM error larger than $\pm 5\%$ were avoided by restricting the maximum allowed FA to 15° (red line in Figure 3.9).

As defined in the methods sections, optimized solutions were sought using the proposed CRLB framework for the different combinations of number of SPGR and SSFP measurements described in Figure 5.1. Optimization results can be seen in Figure 5.5 where the optimal solutions for each explored combination of different number of SPGR and SSFP ($N_{SPGR} : N_{SSFP}$) measurements are shown. Figure 5.5 is then colour coded based on the fraction of time spent on either

N_{SPGR}:N_{SSFP}		SPGR				SSFP					100×CF_{grid}
2:4(Baseline)	α^{SPGR}(°)	4.0	18.0			15.0	65.0	15.0	65.0	α^{SSFP}(°)	11.25
	T_R^{SPGR}(ms)	6.2	6.2			180	180	0	0	ϕ_{RF}(°)	
1:4	α^{SPGR}(°)	15.0				10.2	51.1	11.1	42.6	α^{SSFP}(°)	8.04
	T_R^{SPGR}(ms)	12.4				255	327	92	143	ϕ_{RF}(°)	
2:4	α^{SPGR}(°)	9.3	13.0			11.8	44.0	46.1	10.5	α^{SSFP}(°)	8.06
	T_R^{SPGR}(ms)	4.2	8.2			95	125	292	252	ϕ_{RF}(°)	
1:5	α^{SPGR}(°)	12.3				9.2	8.9	41.7	8.4	44.7	α^{SSFP}(°)	8.67
	T_R^{SPGR}(ms)	8.2				305	211	285	99	95	ϕ_{RF}(°)	
2:3	α^{SPGR}(°)	9.9	14.9					8.2	10.3	24.4	α^{SSFP}(°)	10.19
	T_R^{SPGR}(ms)	4.4	12.2					154	322	274	ϕ_{RF}(°)	
2:5	α^{SPGR}(°)	15.0	13.0			19.0	65.0	4.1	11.3	65.0	α^{SSFP}(°)	10.54
	T_R^{SPGR}(ms)	4.2	4.2			246	77	316	191	284	ϕ_{RF}(°)	
3:3	α^{SPGR}(°)	3.2	10.3	10.0				20.5	64.4	5.9	α^{SSFP}(°)	10.63
	T_R^{SPGR}(ms)	8.2	4.2	4.2				28	300	114	ϕ_{RF}(°)	
4:2	α^{SPGR}(°)	2.1	13.1	2.3	12.0				41.4	41.4	α^{SSFP}(°)	10.72
	T_R^{SPGR}(ms)	4.2	6.2	5.2	5.2				39	219	ϕ_{RF}(°)	
3:2	α^{SPGR}(°)	15.0	11.1	3.0					42.0	42.0	α^{SSFP}(°)	10.75
	T_R^{SPGR}(ms)	8.2	4.2	8.4					38	219	ϕ_{RF}(°)	
3:4	α^{SPGR}(°)	2.2	9.6	3.6		7.6	6.1	65.0	65.0	α^{SSFP}(°)	12.21
	T_R^{SPGR}(ms)	4.2	4.2	4.2		86	62	126	287	ϕ_{RF}(°)	
4:3	α^{SPGR}(°)	15.0	15.0	13.8	3.3			65.0	65.0	65.0	α^{SSFP}(°)	13.96
	T_R^{SPGR}(ms)	4.2	4.2	4.2	4.2			233	50	5	ϕ_{RF}(°)	

Figure 5.5: Brain specific optimized JSR acquisition protocols. Baseline shown for reference. 2:4 acquisition protocol was selected for *in vivo* acquisition. From top to bottom optimized protocols are rank ordered based on their attained worse case percentage precision ($100 \times CF_{grid}$ - Equation 4.8) values. Each row is colour coded based on the fraction of time is spent on either SPGR (orange) or SSFP (blue) acquisitions. All obtained protocols are subject to a $T_{total} = 29.2ms$ constraint.

SPGR (orange) or SSFP (blue) acquisitions. Note that best performing acquisitions require larger fraction of time in SSFP acquisition. Each horizontal bar shows the parameters obtained for each explored combination of $N_{SPGR} : N_{SSFP}$ measurements and is rank ordered based on their expected CF_{grid} value (Equation 4.8). All explored protocols are restricted to the self-imposed time constraint of $T_{total} = 29.2ms$ as to guarantee fair comparison with the considered baseline protocol.

5.4.4 In Vivo Experiment

The performed *in vivo* validation, directly compared estimation maps obtained using conventional DESPOT1/2 and JSR fitting methods operating on data acquired using the Baseline protocol. Furthermore, in order to validate that the proposed CRLB framework allows selection of improved acquisition protocols, a brain optimized JSR protocol (based on Figure 5.5) with 2 SPGR and 4 SSFP measurements was also acquired. Given the expected similar performance between 1:4, 2:4 (validated in phantom experiment - see Figure 5.4) we chose to

apply the 2:4 acquisition since collecting two SPGR scans provides a more robust solution for subjects who might not be able to be so still. For reference, representative axial slices of the different acquisition parameters are demonstrated in Figure 5.6. It it interesting to notice how optimized protocol requires sampling of SPGR images with hight T_1 contrast and SSFP images with low banding artifacts. This is contrary to what is observed in the considered baseline protocol where a SPGR image with low T_1 contrast is required as well as SSFP measurements with $\Phi_{RF} = 0^\circ$ which inherently have low SNR.

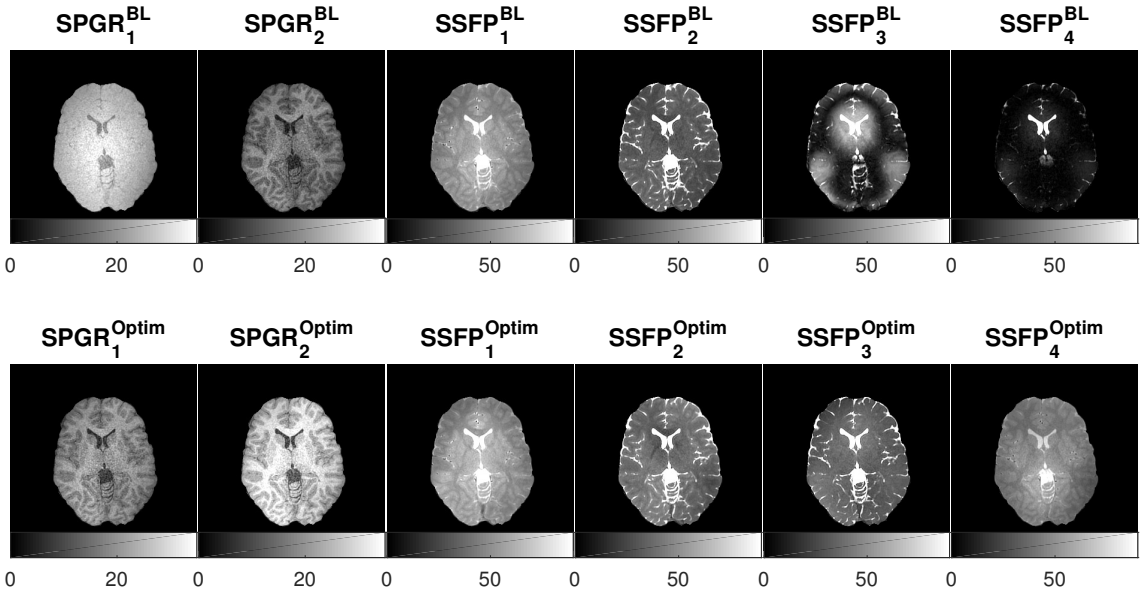

Figure 5.6: A representative axial slice of *in vivo* acquired data from the Baseline (top row) and Optimal (bottom row) protocols. Acquisition parameters for each image are given in Figure 5.5 listed in the same order as presented here. Optimized protocol requires sampling of both SPGR images with high T_1 contrast and low banding artifacts of SSFP acquisition contrary to what is observed in the considered baseline protocol.

Exemplar estimation maps can be seen in Figure 5.7. Note that DESPOT 1/2 relaxation parameter maps (left column in Figure 5.7) are clearly more noisy that the corresponding JSR maps (columns 2 and 3 in Figure 5.7). Also the off-resonance map obtained with two-step fit is much more contaminated by explicit anatomy (particularly the Cerebrospinal Fluid (CSF) spaces) than the corresponding estimate from the JSR process.

Due to its high SNR and contrast the adult optimized SPGR with 8.2ms repetition time was used after brain extraction to segment CSF, WM and GM as described in the Methods section. Tissue specific relaxation histograms were then plotted for all the acquisition schemes and are summarized in Figure 5.8.

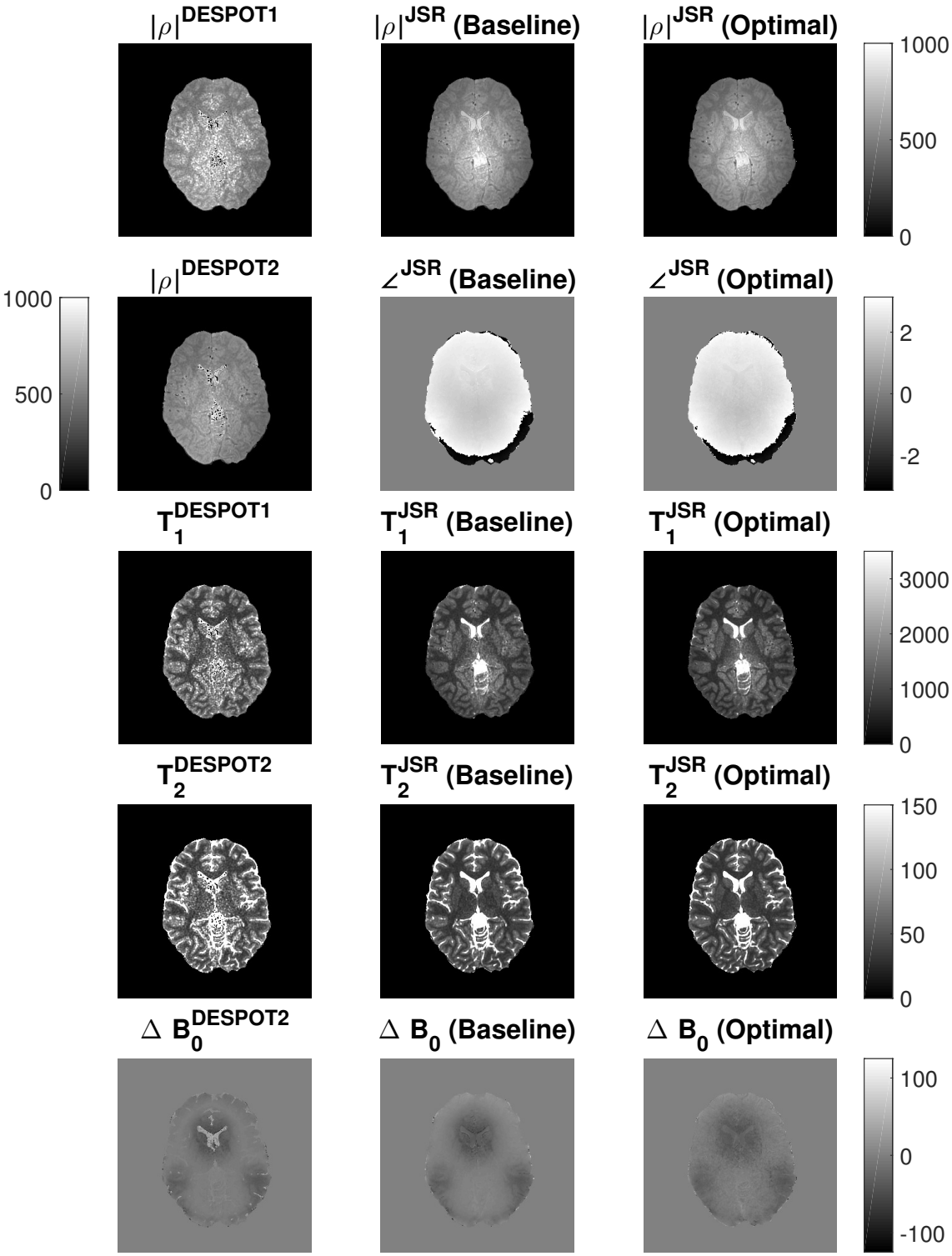

Figure 5.7: Comparison between conventional DESPOT1/2 approach (Left Column), JSR with Baseline protocol (Middle Column) and JSR optimized protocol (Right Column) estimation maps

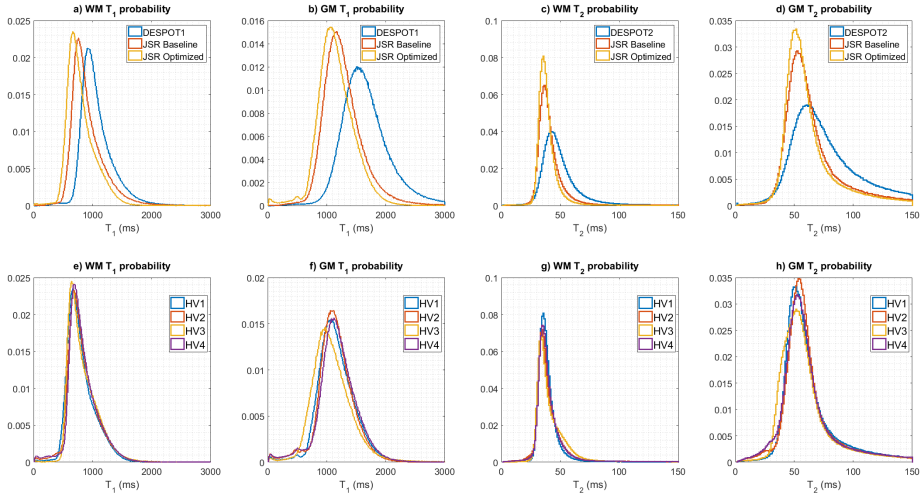

Figure 5.8: Tissue specific histograms for *in vivo* acquisition. Top row compares distributions obtained for Healthy Volunteer number 2 (HV2) with conventional DESPOT1/2 (blue), JSR with Baseline parameters (red) and JSR with optimized acquisition parameters (yellow). Bottom row compares JSR optimized histograms for all imaged volunteers. Tissue segmentation was obtained using the FSL *fast* tool.

Figure 5.8 a), b), c) and d) show the WM/GM T_1 and WM/GM T_2 voxel parameter value frequency distributions obtained on Healthy Volunteer number 2 (HV2) using DESPOT1/2 (blue), JSR with Baseline acquisition (red) and JSR with optimized acquisition (yellow) parameters. As with phantom data, the use of JSR on baseline protocol data, produces narrower estimation distributions compared to the conventional DESPOT1/2 approach. However, the estimation mean relaxation time values shows significant shifts towards lower relaxation time values. Figure 5.8 e), f), g) and h) show the WM/GM T_1 and WM/GM T_2 histograms obtained using the optimized JSR acquisition for all the Healthy Volunteers, showing the reproducibility of the proposed method.

5.5 Discussion

This work aimed to improve precision of DESPOT1/2 based on the joint system relaxometry (JSR) approach, where all the key parameters are estimated in a single calculation. Figure 2 shows 72%/77% decrease in interquartile range of T_1/T_2 estimation between conventional DESPOT and JSR estimation. This is further corroborated by in-vivo data where visual assessment (Figure 5.7) shows that JSR approach reduces the noise of the estimated maps, more specifically in deep grey matter areas where SNR is intrinsically lower. Tissue specific distributions in Figure 5.8 a), b), c) and d) show narrower distributions for JSR compared to VFA

DESPOT1/2. This is mainly due to conventional DESPOT estimation being limited by the inherently lower SNR of the SPGR acquisition. The noise distribution of T_1 then limits T_2 assessment and does not make full use of the high bSSFP SNR. Our approach makes full use of bSSFP information diminishing the estimation variance for both relaxation times. Although more narrow, there are systemic differences between estimated relaxation distributions which are dependent on the specific set of acquisition parameters used, but these are highly reproducible Figure 5.8 e), f) g) and h). Numerical simulations using the described single pool model suggests minimal to no difference on the average estimated values should occur between the estimation procedures even when taking into account errors induced by neglecting T_2'. Indeed, not taking this extra decay into account induces higher JSR estimated T_1 values (opposite of what is seen in Figure 5.4 and Figure 5.8) as the reduction in signal is accommodated as higher saturation of the SPGR curve. Another possible source of error is persistent residual non-linearities that may occur in the RF power amplifier. One possible solution is to follow the work presented by Lutti et. al [84] and fix the RF amplifier power and vary the RF pulse duration to achieve different flip angles. In our work, weve adopted to keep a fix pulse duration and perform a vendor calibration step on each subject that allows pre emphasis of the non-linearities. This approach has the advantage that excitation off-resonance deviations are maintained consistent between different measurements. Phantom data and in-vivo discrepancies are most likely due to magnetization transfer effects, which were not taken into account by the model used in this chapter, but are known to strongly affect the signal of SSFP ([85–87]) which is now used to jointly estimate T_1 and T_2. To corroborate this, the same phantom protocol was acquired on a gel phantom with 4% agarose solution (measured MTR of 20%). For this phantom, the bias between spin echo and VFA measurements was between 5% and 43% for T_1 and -18% and 22% for T_2. This is a larger variation than for the 0.5% Agarose experiment summarised in Figure 5.4 where the range of obtained bias is 4.4% to 15.1% for T_1 and -11.4% to 20.7% for T_2. In Figure 5.8 e), f) g) and h) the optimal JSR protocol tissue specific histograms for each of the Healthy Volunteers are overlaid for comparison. Excellent agreement is shown between all subjects for WM. Relaxation times histograms for GM show slightly larger deviations between subjects although a good agreement is still present. This is most likely due to differences in the brain extraction step of our processing pipeline, although some of the discrepancy can also be attributed to genuine inter-individual variance.

The *in vivo* T_2 values show a significant underestimation when compared to other studies [54, 55, 88]. However, this was not the case for the phantom ex-

periment and in fact failing to apply the T_{RF} correction [79] for the phantom data resulted in an overestimation of the obtained T_2 values by 15-20% compared to the ones displayed in Figure 5.4. This gives confidence that the correction is appropriate, at least for the phantom, which has a much lower MTR than adult brain [7, 72], although it is still not zero.

The second part of this work focused on the validation of the proposed CRLB framework as a protocol design tool. Numerical validations (Figure 5.2) suggest good agreement between the proposed estimation procedure variance and the predicted CRLB (percentage difference $<$1%), without affecting the estimation bias, giving confidence in both the fitting routine and optimization tool. In order to make all results comparable and especially because varying the total acquisition time changes the overall SNR in all scenarios, we optimised the SPGR and SSFP measurements subject to a self-imposed time constraint Ttotal=29.2ms that matches the baseline protocol taken from the literature [54]. Sensitivity of the SPGR measurement to imperfect spoiling was avoided by restricting the maximum allowed SPGR FA to 15°. This cut-off guarantees expected WM spoiling inconsistencies are below 5% while GM are kept bellow 8% for all optimization protocols explored. Although some solutions might benefit from allowing higher SPGR FA this would imply either exploring optimal ways to weight Equation 4.8 given the EPG vs SPGR deviations or employment of a better spoiling scheme such as the one presented in [26] which are both outside the scope of this work as the two best protocols obtained are expected to induce signal bias $\leq 3\%$ for both WM and GM. Also, in the proposed JSR method bSSFP signal is does not suffer from incorrect spoiling bias, and therefore it is expected that spoiling bias will be mitigated since bSSFP T_1 information will help obtain correct solution. Figure 5.1 summarizes the different acquisition options explored in this paper while their respective cost function (CF) figures of merit are summarized in Figure 5.5. The standard approach requires a minimum of two SPGR measurements to estimate T_1, we note that performing JSR allows the acquisition to only require 1 SPGR measurement. This is interchangeable with increasing the number of SPGR measurements provided that the same time is spent sampling SPGR information (Figure 5.4 and 5.5) which is further validated in Figure 5.4 where experimental data corroborates this interchangeability. Both optimal protocols result in a T_1 and T_2 interquartile range reduction of respectively 81% and 87% in comparison to the two step fitting process and 32% and 43% relative to JSR fitting using the baseline protocol. Allowing a single SPGR measurement could be of significant practical importance as SPGR acquisitions are routinely used for clinical diagnosis. Therefore, full brain relaxometry can be achieved by adding 4 bSSFP measurements

which corresponds to less than 5-minute extension of the total scan time.

The JSR framework presented can help achieve optimal acquisition efficiency. In this study full 3D 0.8mm3 isotropic relaxation maps of the human brain were obtained with a total acquisition time of 11 minutes and 18 seconds (9:18 for SPGR and SSFP data plus 2:00 for B1 field estimation). Although we restricted our acquisition time to a baseline protocol for comparison, it would be possible to trade-off JSR's gain in precision for further reduction of the acquisition time.

The work here presented is a proof of concept and demonstrates the benefit of simultaneously using images with different signal responses to minimize variance in relaxometry estimation. Although neglected throughout this work, the JSR framework can be expanded to estimate T_2 by allowing different echo times between acquisitions. Also, it is feasible to include B_1 field estimation directly from the VFA data by incorporating an inversion recovery sequence (e.g. MPRAGE) into the joint system model. Investigation of such protocols showed that the CRLB design framework can be applied, but initial in-vivo testing with JSR processing resulted in T_1 values with higher systematic deviations for different acquisition parameters (e.g. inversion time, RAGE block duration, etc) compared to what is presented in this work. We attribute this to the very different RF conditions engendered by such sequences causing a model bias as a result of MT effects that are not considered (data not shown). This is currently the subject of further investigation, in particular, the option to explicitly include MT in the JSR approach is an interesting future possibility. The JSR approach has a lot in common with the recently introduced fingerprinting concept (MRF) [89, 90], in that all acquired data is employed to estimate the final relaxation and associated parameters. The relative merits of this optimised framework and MRF, both in terms of precision and efficiency remain to be explored.

5.6 Conclusion

The work here presented shows an immediate benefit of the proposed Joint System Relaxometry analysis approach compared to conventional DESPOT1/2 to produce relaxation maps with improved precision. It was also shown that further improvement can be achieved by making use of the Cramér-Rao Lower Bound as a protocol design tool. With this approach it is possible to achieve sub-millimetre maps of ρ, T_1, T_2 and B_0 in an 11-minute examination making the approach appealing for potential clinical use. For examinations in which the clinical protocol

already includes SPGR, the additional time needed to achieve quantitative relaxometry maps is even smaller (≤ 7 additional minutes including B1 calibration in the example shown). As with all variable flip angle approaches, the absolute values of the relaxation times found tend to deviate systematically from spin echo based measurements. However high reproducibility combined with efficiency endow these methods with significant advantages for larger scale studies. The proposed framework enhances both precision and efficiency, further adding to their potential utility.

Chapter 6

Constant Saturation of Magnetization Transfer (CSMT)

So far, throughout this thesis, the influence of magnetization transfer (MT) effects on the final estimation maps has been neglected. In the previous chapter we've shown that the single compartment model can yield precise relaxation times estimates, and values for both T_1 and T_2 are highly stable and reproducible. However, accuracy in simple phantoms and in tissue shows wide variability for different studies [6] and a consensus is yet to be achieved. The work presented in the previous chapter also demonstrates highly reproducible variations dependent on the acquisition parameters selected. Therefore, in the current chapter, it is hypothesised that a key factor in this variability is tissue complexity which undermines the single pool assumption even in nominally homogeneous regions. Multi-compartment relaxometry models have been proposed such as mcDESPOT [8, 91] or qMT [7, 87, 92], and these include 2 or more microscopic pools which exchange magnetization between them although there is not yet an unanimity within the scientific community about the best approach. An interesting discussion regarding the assumptions of different multi-compartment tissue models can be found elsewhere [93]. On the other hand, this increased complexity both decreases the stability of the solutions found [9] and requires a multitude of measurements which prolong the total required acquisition time and therefore clinical applicability. In this work, instead of applying a two-pool model estimation approach, this chapter reflects on the consequences of relaxation estimation assuming a single pool model on data generated using a magnetization transfer two-pool signal. With this in mind, a method is proposed to stabilise VFA measurements of T_1 and T_2 by creating Constant Saturation of Magnetization Transfer (CSMT) conditions for all the sequences deployed and compared this new ap-

proach with conventional sampling schemes.

6.1 Introduction

6.1.1 Magnetization Transfer 2-pool Model

To this point, each measured voxel was assumed to be uniform and contain a single tissue type. Although valid for many phantoms, biological tissues are known to contain a higher level of complexity that has to be addressed. To a certain degree [87], this complexity can be approximated by considering a two-pool exchanging model [92]. This considers a pool of "free" protons (*f*) associated with mobile water molecules and a restricted pool of protons (*r*) associated with heavy and less mobile molecules [7, 87, 94] that are allowed to exchange between each other. The restricted pool of protons is characterized by its quick loss of coherence resulting in characteristic times $T_{2,r} \approx 10\mu s$ [95]. Therefore, the transverse magnetization of this component is negligible and, as consequence, the flip angle concept doesn't apply to it [95]. This leads to the extended definition of magnetization vector such that:

$$\vec{M} = \begin{bmatrix} M_{x,f} & M_{y,f} & M_{z,f} & M_{z,r} \end{bmatrix}^T \tag{6.1}$$

where, the subscripts f and r indicate parameters that relate respectively to the free and restricted magnetization pools. The temporal rate of change of the magnetization will be governed by:

$$A = \begin{bmatrix} -R_{2,f} & \delta B_0 & -\omega_{1y} & 0 \\ -\delta B_0 & -R_{2,f} & \omega_{1x} & 0 \\ \omega_{1y} & -\omega_{1x} & -R_{1,f} - k_f & k_r \\ 0 & 0 & k_f & -R_{1,r} - k_r - W(\Delta, t) \end{bmatrix} \tag{6.2}$$

where k_f is the exchange rate of magnetization that migrates from the free pool to the restricted pool and k_r is the exchange rate of magnetization that migrates from the restricted pool to the free pool. $W(\Delta, t)$ is the mean longitudinal magnetization saturation rate for the bound pool and is given by [87, 95]:

$$\left\langle W(\Delta) \right\rangle = \frac{\pi}{T_{RF}} \int_0^{T_{RF}} \omega_1^2(t) dt G(\Delta) \tag{6.3}$$

where $\omega_1(t)$ is the applied excitation field and $G(\Delta)$ is the absorption line shape, which for tissues is best approximated by the super-Lorentzian [7, 96, 97]:

$$G(\Delta) = \int_0^1 \sqrt{\frac{2}{\pi}} \frac{1}{R_{2_r}|3u^2-1|} e^{-2(\frac{2\pi\Delta}{R_{2,r}3u^2-1})^2} du \tag{6.4}$$

for which Δ is the off-resonance of the excitation pulse and $u = \cos\theta$ is a scaling factor which reflects an angular dependence of cell membrane bilayers with the external magnetic field [96, 97]. Other lineshapes such as Lorentzian, Gaussian and Kubo-Tomita have been used to characterize tissue samples [93], and discussion between the compromises of each one is still under investigation. At fixed on-resonance excitation ($\Delta = 0$) the absorption line shape can be assumed constant $G(\Delta \to 0) = G$. If one assumes constant amplitude non-selective excitation Equation 6.3 simplifies into:

$$\left\langle W \right\rangle = \pi\omega_1^2 G \tag{6.5}$$

showing that the amount of saturation depends on the square of the RF field applied. The final time evolution differential relationship will be described by [12, 98]:

$$\frac{d\vec{M}}{dt} = A\vec{M} + B, B = \begin{bmatrix} 0 & 0 & M_{0,f}R_{1,f} & M_{0,r}R_{1,r} \end{bmatrix}^T \tag{6.6}$$

The solution to Equation 6.6 is not trivial to obtain, however, following the approach suggested by Gloor et al. in [87], decoupling the exchange processes from the relaxation processes (the same principle applied when assuming relaxation is independent of excitation) can be achieved by assuming instantaneous exchange. In other words, throughout this section, excitation, relaxation and exchange are assumed decoupled and solutions for each regime are derived from the two-pool coupled Bloch Equations.

Relaxation

Assuming relaxation is independent of exchange and no excitation occurs, A (Equation 6.2) can be simplified into:

$$A_{Relaxation} = \begin{bmatrix} -R_{2,f} & \delta B_0 & 0 & 0 \\ \delta B_0 & -R_{2,f} & 0 & 0 \\ 0 & 0 & -R_{1,f} & 0 \\ 0 & 0 & 0 & -R_{1,r} \end{bmatrix} \tag{6.7}$$

where a solution can be obtained by applying the Laplace transform $\mathcal{L}$ to each term of Equation 6.6 and the system of differential equations becomes a system of linear equations that can be solved by:

$$\mathcal{L}\left(\frac{d\vec{M}(t)}{dt}\right) = s\vec{M}(s) - \vec{M}(t=0) = A\vec{M}(s) + s^{-1}B \tag{6.8}$$

$$\begin{aligned} s\vec{M}(s) - A\vec{M}(s) &= s^{-1}B + \vec{M}(t=0) \\ (sI - A)\vec{M}(s) &= s^{-1}B + \vec{M}(t=0) \\ \vec{M}(s) &= (sI - A)^{-1}(s^{-1}B + \vec{M}(t=0)) \\ \vec{M}(t) &= \mathcal{L}^{-1}(\vec{M}(s)) \\ \vec{M}(t) &= E(t, \delta B_0)\vec{M}(t=0) + E_b(t) \end{aligned} \tag{6.9}$$

such that:

$$E(t, \delta B_0) = \begin{bmatrix} E_{2,f}\cos\delta B_0 & E_{2,f}\sin\delta B_0 & 0 & 0 \\ -E_{2,f}\sin\delta B_0 & E_{2,f}\cos\delta B_0 & 0 & 0 \\ 0 & 0 & E_{1,f} & 0 \\ 0 & 0 & 0 & E_{1,r} \end{bmatrix} \tag{6.10}$$

and,

$$E_b(t) = \begin{bmatrix} 0 & 0 & M_{0,f}(1 - E_{1,f}) & M_{0,r}(1 - E_{1,r}) \end{bmatrix} \tag{6.11}$$

where $E_{1,f/r} = e^{-tR_{1,f/r}}$ and $E_{2,f/r} = e^{-tR_{2,f/r}}$. Compared to the single pool relaxation given the assumptions taken, the two-pool model relaxation operator only differs by the extra recovery of the restricted pool longitudinal magnetization.

Exchange

The same approach used to derive the effects of relaxation on the magnetization vector can be used to obtain a solution for the exchange between the free and restricted magnetization pools. Adapting A from Equation 6.2 under the conditions of no relaxation or excitation it follows that:

$$A_{Exchange} = \begin{bmatrix} 0 & 0 & 0 & 0 \\ 0 & 0 & 0 & 0 \\ 0 & 0 & -k_f & k_r \\ 0 & 0 & k_f & -k_r \end{bmatrix}, B = \vec{0} \tag{6.12}$$

and Equation 6.6 follows as:

$$\begin{aligned} \frac{d\vec{M}}{dt} &= A\vec{M} \\ \mathcal{L}\left(\frac{d\vec{M}(t)}{dt}\right) &= s\vec{M}(s) - \vec{M}(t=0) = A\vec{M}(s) \\ (sI - A)\vec{M}(s) &= \vec{M}(t=0) \\ \vec{M}(s) &= (sI - A)^{-1}\vec{M}(t=0) \\ \vec{M}(t) &= \mathcal{L}^{-1}(\vec{M}(s)) \\ \vec{M}(t) &= Ex(t)\vec{M}(t=0) \end{aligned} \tag{6.13}$$

where $Ex(t)$ is given by:

$$Ex(t) = \begin{bmatrix} 1 & 0 & 0 & 0 \\ 0 & 1 & 0 & 0 \\ 0 & 0 & \frac{1}{F+1} + \frac{Fe^{-tk_r(F+1)}}{F+1} & \frac{1}{F+1} - \frac{e^{-tk_r(F+1)}}{F+1} \\ 0 & 0 & \frac{F}{F+1} - \frac{Fe^{-tk_r(F+1)}}{F+1} & \frac{F}{F+1} + \frac{e^{-tk_r(F+1)}}{F+1} \end{bmatrix} \tag{6.14}$$

where to $F = M_{0,f}/M_{0,r}$ represents the fractional size between the two pools and by definition $F = k_f/k_r$ [87] concluding the derivation of the overall exchange within short repetitions times.

Excitation

During excitation, assuming neither relaxation or exchange occur for continuous non-selective excitations applied along the x axis Equation 6.2 simplifies into:

$$A_{Excitation} = \begin{bmatrix} 0 & 0 & 0 & 0 \\ 0 & 0 & \omega_{1x} & 0 \\ 0 & -\omega_{1x} & 0 & 0 \\ 0 & 0 & 0 & -\pi\omega_1^2 G \end{bmatrix} \tag{6.15}$$

which has the following solution:

$$R(T_{RF}) = \begin{bmatrix} 1 & 0 & 0 & 0 \\ 0 & \cos(\omega_1 T_{RF}) & \sin(\omega_1 T_{RF}) & 0 \\ 0 & -\sin(\omega_1 T_{RF}) & \cos(\omega_1 T_{RF}) & 0 \\ 0 & 0 & 0 & e^{-\pi\omega_1^2 G T_{RF}} \end{bmatrix} \tag{6.16}$$

which summarizes the effect of a continuous ω_1 field applied during a total duration T_{RF} on a two-pool system. As with relaxation, Equation 6.16 is built from the magnetization rotation of the free-pool magnetization with an additional saturation of the restricted-pool given by $e^{-\pi\omega_1^2 G T_{RF}}$.

SPGR and SSFP two-pool description

Once relaxation, exchange and excitation have been described it is possible to compute steady state descriptions of the magnetization following a matrix operation formalism [87]. Describing the magnetization immediately after the n^{th} RF pulse as M_n^+, M_n^- the magnetization preceding the pulse and the spoiling operator S such that:

$$S = \begin{bmatrix} 0 & 0 & 0 & 0 \\ 0 & 0 & 0 & 0 \\ 0 & 0 & 1 & 0 \\ 0 & 0 & 0 & 1 \end{bmatrix} \tag{6.17}$$

the SPGR steady-state can be computed as follows:

$$\begin{aligned} M_n^+ &= RM_n^- \\ M_{n+1}^- &= SE_{ex}EM_n^+ + SE_{ex}E_b \\ M_{n+1}^+ &= RSE_{ex}EM_n^+ + RSE_{ex}E_b \\ M_{SPGR}^{SS} &= RSE_{ex}EM_{SPGR}^{SS} + RSE_{ex}E_b \\ (I - RSE_{ex}E)M_{SPGR}^{SS} &= RSE_{ex}E_b \\ M_{SPGR}^{SS} &= (I - RSE_{ex}E)^{-1}RSE_{ex}E_b \end{aligned} \tag{6.18}$$

The SSFP steady state derivation follows the same procedure except the spoiling operator is not applied:

$$M_{SSFP}^{SS} = (I - RE_{ex}E)^{-1}RE_{ex}E_b \tag{6.19}$$

6.1.2 Constant Saturation MT (CSMT)

Tissue T_1 and T_2 are known to be dependent on the measurement technique applied [6], with T_1 in particular being influenced by MT and the RF conditions employed [85, 99, 100]. For a binary pool system, the observed T_1 depends on the saturation state of the background pool, which is directly dependent on the total energy of the RF pulses applied as measurement (operator $R(T_{RF})$ of Equation 6.16) and the timings used (operator $Ex(t)$ of Equation 6.14) in the sequences [85,95,101]. This is of special importance for steady-state VFA methods [55, 85, 101, 102] where a range of flip angles are deployed which, if care is not taken, may induce variable saturation of the background pool across different measurements. Unless this is taken into account, the measured relaxation properties are expected to vary with the measurement parameters [99,101,103]. With this in mind, it was hypothesised that, ensuring constant saturation of MT (CSMT) effects would allow single-pool model assumptions to be valid. In mathematical terms, we build on the two-pool coupled Bloch equations:

$$\begin{aligned}
\frac{dM_{xf}}{dt} &= -R_{2f}M_{xf} + \delta B_0 M_{y,f} - \omega_{1y}M_{zf} \\
\frac{dM_{yf}}{dt} &= -\delta B_0 M_{xf} - R_{2f}M_{yf} + \omega_{1x}M_{zf} \\
\frac{dM_{zf}}{dt} &= \omega_{1y}M_{xf} - \omega_{1x}M_{yf} - (R_{1f} + \kappa_f)M_{zf} + \kappa_r M_{zr} + R_{1f}M_{0f} \\
\frac{dM_{zr}}{dt} &= \kappa_f M_{zf} - (R_{1r} + \kappa_r + < W >)M_{zr} + R_{1r}M_{0r}
\end{aligned} \tag{6.20}$$

and construct the time evolution after the excitation is applied, enforcing CSMT conditions within one T_R can be approximated as setting $\frac{dM_{zr}}{dt} = 0$ and therefore, the coupled two-pool differential equation system becomes:

$$\begin{aligned}
\frac{dM_{xf}}{dt} &= -R_{2f}M_{xf} + \delta B_0 M_{y,f} \\
\frac{dM_{yf}}{dt} &= -\delta B_0 M_{xf} - R_{2f}M_{yf} \\
\frac{dM_{zf}}{dt} &= -(R_{1f} + \kappa_f)M_{zf} + \kappa_r M_{zr} + R_{1f}M_{0f} \\
0 &= \kappa_f M_{zf} - (R_{1r} + \kappa_r + < W > \frac{T_{RF}}{T_R})M_{zr} + R_{1r}M_{0r}
\end{aligned} \tag{6.21}$$

where, $< W >$ is scaled by the fraction of the time RF pulse in applied during a repetition period to take into account that the amount of saturation induced in the background pool longitudinal magnetization. The terms in the last equation of the system above can then be re-arranged such that an explicit expression for M_{zr} is

found

$$M_{zr} = \frac{\kappa_f M_{zf} + R_{1r} M_{0r}}{R_{1r} + \kappa_r + < W > \frac{T_{RF}}{T_R}}$$
$$M_{zr} = \frac{\kappa_f M_{zf}}{R_{1r} + \kappa_r + < W > \frac{T_{RF}}{T_R}} + \frac{R_{1r} M_{0r}}{R_{1r} + \kappa_r + < W > \frac{T_{RF}}{T_R}} \tag{6.22}$$

With this in mind the system of coupled equations becomes

$$\begin{aligned}
\frac{dM_{xf}}{dt} &= -R_{2f} M_{xf} + \delta B_0 M_{y,f} \\
\frac{dM_{yf}}{dt} &= -\delta B_0 M_{xf} - R_{2f} M_{yf} \\
\frac{dM_{zf}}{dt} &= -(R_{1f} + \kappa_f (1 - \frac{\kappa_r}{R_{1r} + \kappa_r + < W > \frac{T_{RF}}{T_R}})) M_{zf} \\
&\quad + R_{1f} M_{0f} + \frac{\kappa_r R_{1r} M_{0r}}{R_{1r} + \kappa_r + < W > \frac{T_{RF}}{T_R}}
\end{aligned} \tag{6.23}$$

which can be found to have the solution:

$$\begin{aligned}
M_{xf} &= E_{2f} \cos(T_R \delta B_0) M^0_{xf} + E_2 \sin(T_R \delta B_0) M^0_{yf} \\
M_{yf} &= -E_{2f} \sin(T_R \delta B_0) M^0_{xf} + E_2 \cos(T_R \delta B_0) M^0_{yf} \\
M_{zf} &= [M^0_{zf} - \frac{\lambda_2 + M_{0f} R_{1f}}{\lambda_1 + R_{1f}}] e^{-T_R (R_{1f} + \lambda_1)} + \frac{\lambda_2 + M_{0f} R_{1f}}{\lambda_1 + R_{1f}}
\end{aligned} \tag{6.24}$$

where M^0_{xf}, M^0_{yf} and M^0_{zf} are respectively the x, y and z components of the initial magnetization, $E_2 = e^{-T_R R_{2f}}$ and $\lambda_{1,2}$ are defined as:

$$\lambda_1 = \kappa_f (1 - \frac{\kappa_r}{R_{1r} + \kappa_r + < W > \frac{T_{RF}}{T_R}}) \tag{6.25}$$

$$\lambda_2 = \frac{\kappa_r R_{1r} M_{0r}}{R_{1r} + \kappa_r + < W > \frac{T_{RF}}{T_R}} \tag{6.26}$$

From Equations 6.24 to 6.26 two main conclusions can be inferred. Firstly, if M_{zr} can be assumed constant within T_R period, the two-pool magnetization effectively behaves as a single-pool with M_0^{app} and R_1^{app} defined as:

$$R_1^{app} = R_{1f} + \lambda_1 \tag{6.27}$$

$$M_0^{app} = \frac{\lambda_2 + M_{0f} R_{1f}}{R_1^{app}} \tag{6.28}$$

And M_{zf} is simply described as:

$$M_{zf} = [M^0_{zf} - M_0^{app}] e^{-T_R R_1^{app}} + M_0^{app} \tag{6.29}$$

Which is in line with the solution derived for the single pool model in Chapter 2 (Equation 2.14). The reader is invited to note, that in the limit of idealized saturation ($< W > \frac{T_{RF}}{T_R} \rightarrow \infty$) both Equation 6.27 and 6.28 converge to the idealized solution previously reported in [103].

$$
\begin{aligned}
R_1^{app}(< W > \frac{T_{RF}}{T_R} \rightarrow \infty) &= R_{1f} + \kappa_f \\
M_0^{app}(< W > \frac{T_{RF}}{T_R} \rightarrow \infty) &= M_{0f} \frac{R_{1f}}{R_{1f} + \kappa_f}
\end{aligned}
\tag{6.30}
$$

Secondly, given that for both M_0^{app} and R_1^{app} all parameters are tissue dependent, except for $< W > \frac{T_{RF}}{T_R}$, therefore, $< W >$, T_{RF} and T_R can be varied to keep single pool consistency as long as their ratio is kept fixed.

6.2 Methods

All simulations and off-line post-processing were performed using Matlab 2016a (The MathWorks Inc., Natick). All images were obtained on a 3 Tesla Philips Achieva-Tx (Philips Healthcare, Best, Netherlands) system with the manufacturer 32 channel receive only head coil and processed from k-space raw data using MRecon environment (Gyrotools LLC, Zurich, Switzerland). Scanner software was modified in order to allow control of the excitation pulse duration and shape for each measurement.

In order to emulate magnetization transfer effects observed in human brain, a dedicated in-house built phantom was created which consists of a 500mL spherical container filled with TRESemme (Unilever PLC, London, UK) hair conditioner. Hair conditioner was used as it is known to contain fatty alcohols in a lamellar structure that have similar MT properties of brain tissue was created [104].

6.2.1 CSMT Trough non-Selective Multi-Band Excitation

In this work, it is proposed to achieve CSMT conditions by ensuring $< W > \frac{T_{RF}}{T_R}$ is kept constant for all the sequences applied. Typically, saturation of the background pool of protons is induced by applying off-resonance excitation pulse in an MPRAGE-type timing structure of MR imaging. In order to experimentally control $< W >$ we define a non-selective multi-band (MB) pulse that balances changes in on-resonance ($\Delta = 0$) RF to achieve a required flip angle (α_{free}) with

a matched off-resonance contribution to keep total RF energy constant. Note that commonly, MB excitations are designed for simultaneous multi slice imaging applications. Although the concept of a non-selective shaped pulse might seem odd at first, here we make use of the multiple-frequency response of this type of excitation, not to accelerate imaging time, but instead maintain saturation of the background pool at each excitation. This is achieved by superimposing a sinc-gauss RF pulse scaled to produce a reference flip angle, $\alpha_{ref} = 2\pi\gamma \int_0^{T_{RF}} \omega_1^{ref}(t)dt$ with a 2-lobe cosine modulated MB excitation with symmetric bands at offset frequencies $\pm\Delta$. This is achieved by adding a scaled cosine modulated replica of the on-resonant pulse and enforcing a relative scaling of the two components:

$$\omega_1^{CSMT}(t) = 2\pi\gamma[\frac{\alpha_{free}}{\alpha_{ref}}\omega_1^{ref}(t) + \kappa\omega_1^{ref}(t)\cos(\Delta t)],$$
$$s.t. \int_0^{T_{RF}} (\omega_1^{CSMT}(t))^2 dt = \int_0^{T_{RF}} (\omega_1^{ref}(t))^2 dt \tag{6.31}$$

where κ is a scalar which is chosen in order to guarantee the equal power constraint relative to the α_{ref} and T_{RF} is the total duration of the pulse. As a rule of thumb, excitation bandwidth (BW) can be approximated by $T_{RF}^{-1} \propto BW_{RF}$ and is sought to be minimized to avoid direct saturation of the free-pool while maintaining a broad enough BW of the on-resonance lobe to avoid off-resonance excitation variations. Ideally, the background pool saturation should be independent (due to its broad absorption line-shape) of the balance between on- and off-resonance bands ($G(\Delta) \approx G$). However, since $G(\Delta)$ is not completely flat, Δ should be minimized without introducing direct on-resonant saturation of free water. In other words, we sought to minimize the distance between on- and off-resonance bands (in order to better approximate G as constant) while simultaneously avoiding a compromise of the free-pool induced rotation due to ringing of the superimposed off-resonance pulse. The CSMT pulse was therefore simulated and tested with $\alpha_{free} = 0$, variable Δ and increasing T_{RF} to find an operating point that minimised direct on resonance saturation when α_{free} equals 0, while providing efficient sequences. Experimental data were acquired on the in-house built phantom described above.

6.2.2 Numerical Validation

In this section it was sought to numerically verify our assumption that CSMT conditions allow a more robust estimation of single pool relaxometry parameters from two-pool model data. It is expected that, under a regime where single pool assumptions are valid, the accuracy of the estimation process is independent of the

parameter choices (e.g. FA's applied) and only precision will vary. Therefore, we obtain different estimates of M_0, T_1 and T_2 from different subsets of flip angle measurements under five different scenarios:

- **Single Pool:** Flip angle measurements assuming single-pool behaviour of the magnetization (We applied single pool JSR model defined in Chapter 5 with $\rho^r = M_{0f}$, $\rho^i = 0$, $T_1 = T_{1f}$, $T_2 = T_{2f}$ and $\Omega_0 = 0$);
- **Two Pool Varying RF:** Flip angle measurements obtained at fixed T_R and pulse width ($T_{RF} = 0.608ms$) but with variable RF amplitude;
- **Two Pool Varying T_R:** Flip angle measurements obtained with fixed $< W >$ ($T_{RF} = 3.0ms$), but different T_R between sequences such that $T_R^{SPGR} = 14.0ms$ and $T_R^{SSFP} = 3.5ms$;
- **Two Pool CSMT:** Flip angle measurements obtained with fixed $< W >$ ($T_{RF} = 3.0ms$) and $T_R^{SPGR} = T_R^{SSFP} = 7.0ms$;
- **Two Pool CSMT Varying T_R:** Flip angle measurements obtained with varying $< W >$ and T_R between sequences such that $< W > \frac{T_{RF}}{T_R}$ is maintained constant ($T_R^{SPGR} = 14.0ms$ and $T_R^{SSFP} = 3.5ms$).

Literature values of relaxation times for a two-pool model of frontal white matter, as summarised in Table 6.1 and extracted from both [7] and [72], were used to generate noiseless SPGR and SSFP signals based on Equations 6.18 and 6.19 respectively. Acquisition parameters were then simulated (unless stated other-

Frontal white matter					
M_{0f}	$k_f(s^{-1})$	F	$R_{1,f}(s^{-1})$	$T_{2,f}(ms)$	$T_{2,r}(\mu s)$
10.0	4.6	0.152	1.8	56.0	11.8

Table 6.1: Frontal White Matter Two-Pool model relaxation times. [7, 72]

wise) at fixed $T_R = 7.0$ and $T_E = 0.5T_R$ (see results section below) for a FA sweep of SPGR and SSFP measurements which are summarised in the first row of Table 6.2. Following the work of [87] we've defined $G(\Delta \to 0) = 1.4 \times 10^{-5}s$ and $R_{1,r} = R_{1,f}$. In order to highlight the differences between CSMT and conventional acquisition conditions, for each Subset of Table 6.2 (subsets highlighted as cyan entries), 10^5 noisy independent instances of single- and two-pool signals were generated with added Gaussian distributed noise $\sigma = 0.002M_{0f}$ to both real and imaginary components. To validate our assumption that noise will only affect estimation variance without modifying its bias, a noiseless evaluation of each

considered subset was also performed. Note that in Table 6.2 SSFP-0° measurements are used through all subsets to allow background field estimation. For all conditions involving a binary-spin system, excitation of on-resonance magnetization is computed based on a common reference FA $\alpha_{ref} = 68°$. T_{RF} is varied between CSMT and non-CSMT conditions in order to compare with experimental validation (see below). From the simulated data, apparent $\rho^r, \rho^i, T_1, T_2, \Omega_0$ values

	SPGR(°)						SSFP-180(°)						SSFP-0(°)	
All FA	6	8	10	12	14	16	15	25	35	45	55	65	25	55
Subset 1	6	8	10	12	14	16	15	25	35	45	55	65	25	55
Subset 2	6	8	10	12	14	16	15	25	35	45	55	65	25	55
Subset 3	6	8	10	12	14	16	15	25	35	45	55	65	25	55
Subset 4	6	8	10	12	14	16	15	25	35	45	55	65	25	55
Subset 5	6	8	10	12	14	16	15	25	35	45	55	65	25	55
Subset 6	6	8	10	12	14	16	15	25	35	45	55	65	25	55

Table 6.2: Summary of flip angle subsets explored in order to inspect stability of relaxometry estimation. Highlighted in cyan colour are flip angles used at its corresponding subset. SSFP-0° measurements are used through all subsets to allow background field estimation.

are estimated (see Chapter 5) for each subset considered and compared in order to evaluate robustness of the fit under CSMT conditions versus the previously adopted approach with fixed duration and varying power measurement.

6.2.3 Experimental Validation

In order to experimentally validate our assumptions of improved single pool estimation robustness by assuring CSMT, the measurements summarized in Table 6.2 were sampled under both conventional sampling conditions (non-CSMT) and the proposed CSMT framework. Both measurements were performed based on a reference FA of $68°$ ($T_{RF}^{non-CSMT} = 0.60ms$ and $T_{RF}^{CSMT} = 3.00ms$) and with $T_R/T_E = 7.0/3.5$ms. T_R was kept fixed for all acquisitions in order to allow the same amount of exchange effects between different sources of magnetization. The same acquisition parameters were applied in phantom and *in vivo*. All measurements were defined as 3D sagittal acquisition with a field of view of $250 \times 250 \times 250mm^3$ at $0.8mm^3$ isotropic resolution. Sampling bandwidth was kept

at $959Hz/pixel$ and SENSE acceleration factor of 2 in both Anterior-Posterior and Right-Left directions (phase encode directions). Correct transmit field knowledge was obtained via the AFI approach [45, 46] with $T_{R1}/T_{R2} = 40/200ms$ with maximum allowed gradient spoiling between each T_R [73]. AFI nominal flip angle was defined as an 80° hard pulse. FOV was kept the same as SPGR and SSFP measurements and the acquired voxel size was set at $4.46 \times 4.46 \times 4.46mm^3$ for a total acquisition time of 1 minute and 46 seconds. *in vivo* data was acquired on 3 Healthy Volunteers (ages 22-58 years) who gave informed consent according to local ethical guidelines.

One consequence of our assumption that CSMT conditions induce more robust estimation is that, depending on the amount of RF power applied, different apparent M_0's and T_1's will be obtained (respectively M_0^{app} and T_1^{app}). In order to both validate this corollary and demonstrate that this effect is present in other relaxometry methods which are not JSR, DESPOT1 measurements were acquired (SPGR measurements of Table 6.2) at increasing $\int_0^{T_{RF}} (\omega_1^{ref}(t))^2 dt$ values of 0.576, 2.304, 5.184, 9.126, 14.401, 20.738, 28.227 and 36.865 $\mu T^2 ms$.

6.3 Results

6.3.1 Non-Selective Multi-Band Excitation

The top graphs of Figure 6.1 demonstrate the time (left) and frequency (right) domain representation of the designed non-selective MB pulse, for the two extreme cases of $\alpha_{free} = 6^\circ$ (blue) and $\alpha_{free} = 68^\circ$ (orange). No off-resonance is present for $alpha_free = 68^\circ$ as all energy is applied on resonance. Bottom of Figure 6.1 demonstrates expected free-pool induced rotation when $\alpha_{free} = 0^\circ$ as a function of Δ. This undesired excitation is caused by the ripples of the off-resonance lobes and is sought to be minimized. Setting $\Delta = 6KHz$, T_{RF} was defined as 3.0ms as it minimizes the allowed T_R to be 7.0ms in our system and empirically induced a good compromise between excitation bandwidth and acquisition time. This operating point however, can be target of further exploration which is beyond the scope of the current chapter and left for future exploration. The applied echo time was maintained fixed at $T_E = 0.5T_R = 3.5ms$ to maintain the spin echo behaviour of the SSFP acquisition [30] and for consistency used in both SSFP and SPGR acquisitions.

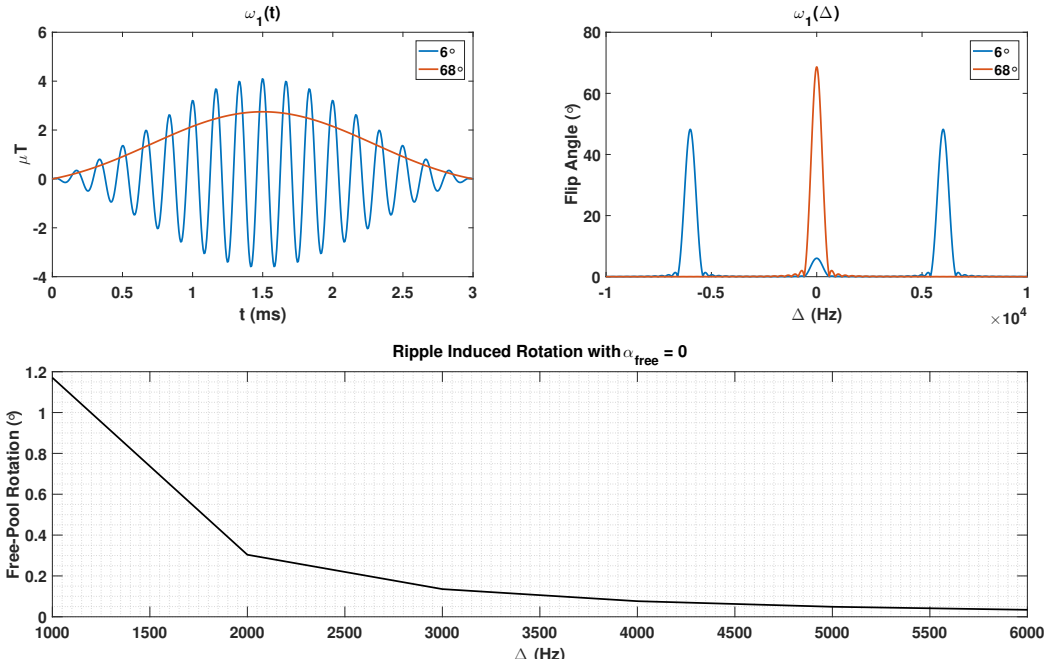

Figure 6.1: Top graphs demonstrate time (left) and frequency (right) representation of the proposed MB pulse for a representative free-pool induced flip angle of $6°$ (blue) and $68°$ (orange). Bottom graph demonstrates the expected free-pool ripple induced excitation when $\alpha_{free} = 0°$ as a function of Δ.

6.3.2 Numerical Validation

Figure 6.2 directly compares both SPGR (blue) and SSFP, with both π (orange) and 0 (yellow) excitation phase increment, signal evolutions as a function of FA (first row Table 6.2) for a fixed $T_R/T_E = 7.0/3.5ms$. Single-pool signal evolutions are represented as solid lines, two-pool model signals generated at fixed T_{RF} and varying RF amplitude are represented as dotted-line, while two-pool model signals under the assumption of CSMT conditions are demonstrated as dashed-line. Note that due to different T_{RF} (adopted so that comparison with experimental validation can be performed) between non-CSMT and CSMT, for a fixed $\alpha_1^{ref} = 68°$, CSMT SSFP signal is less saturated compared to non-CSMT conditions. For lower flip angles, as ω_1 is scaled down under non-CSMT conditions, the amount of induced saturation is reduced and therefore signal approximates single-pool behaviour.

Figure 6.3 summarizes Monte Carlo analysis obtained for the different subsets highlighted, in Table 6.2, and signals plotted in Figure 6.2 when estimating single-pool JSR rM_0 (top), T_1 (middle) and T_2 (bottom). iM_0 and $\Delta\Omega$ are ignored as they were both set to zero and no significant deviations were observed. Five different scenarios were considered:

(i) data simulated using single-pool model (black);

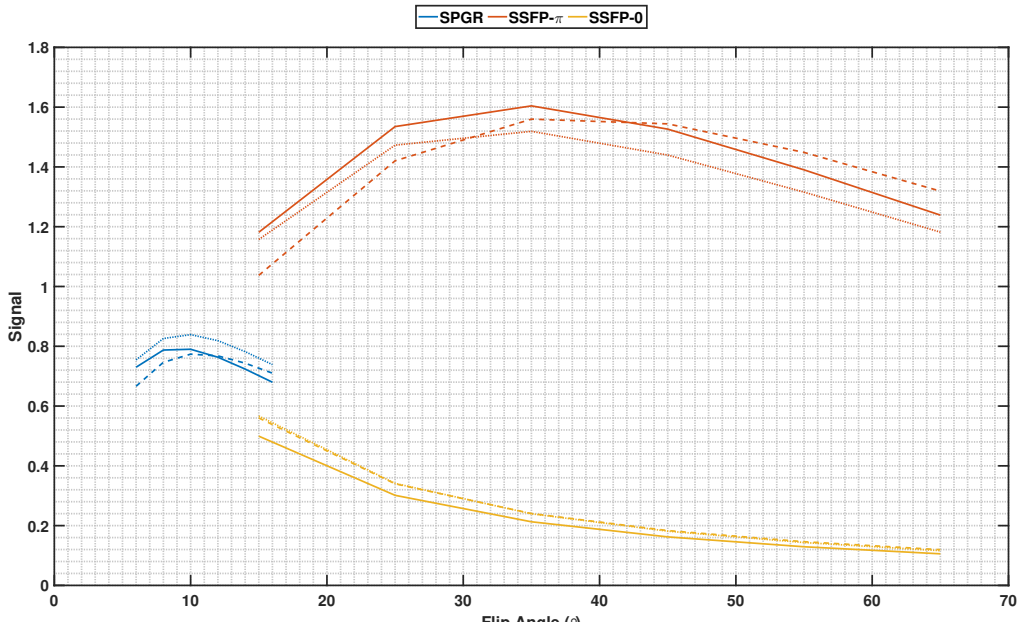

Figure 6.2: Direct comparison between SPGR (blue) and SSFP with π (orange) and 0 (yellow) RF phase increment at each T_R signal evolutions plotted as a function of flip angle for single-pool model (solid lines), two-pool model under varying RF power (dotted lines) and CSMT (dashed lines) conditions. Two-pool model's α_{free} were computed based on a reference flip angle of $\alpha_{ref} = 68°$ with $T_{RF}^{non-CSMT} = 0.6ms$ and $T_{RF}^{CSMT} = 3.0ms$.

(ii) data simulated from two-pool model with varying RF-power (red);

(iii) data simulated from two-pool model at fixed RF-power and different T_R between acquisitions (green);

(iv) data simulated from two-pool model under CSMT sampling conditions with $T_R^{SPGR} = T_R^{SSFP}$ (blue);

(v) data simulated from two-pool model under CSMT sampling conditions with $T_R^{SPGR} = 14.0ms$, $T_R^{SSFP} = 3.5ms$ and $< W >$ scaled accordingly (magenta);

For reference, results from estimation performed under no added noise are overlaid as open circles. As expected, the addition of complex Gaussian noise affects the estimation variance without modifying its bias which can be seen by the overlap between the circles highlighting noiseless estimation and the median of the estimation distribution (middle line of each box-plot). Inspection of Figure 6.3 demonstrates that assuming a single-pool model on two-pool data obtained under variable RF power is expected to have two main effects:

1) Induced fluctuations in the obtained apparent M_0, T_1 and T_2 which depend on measurement parameters;

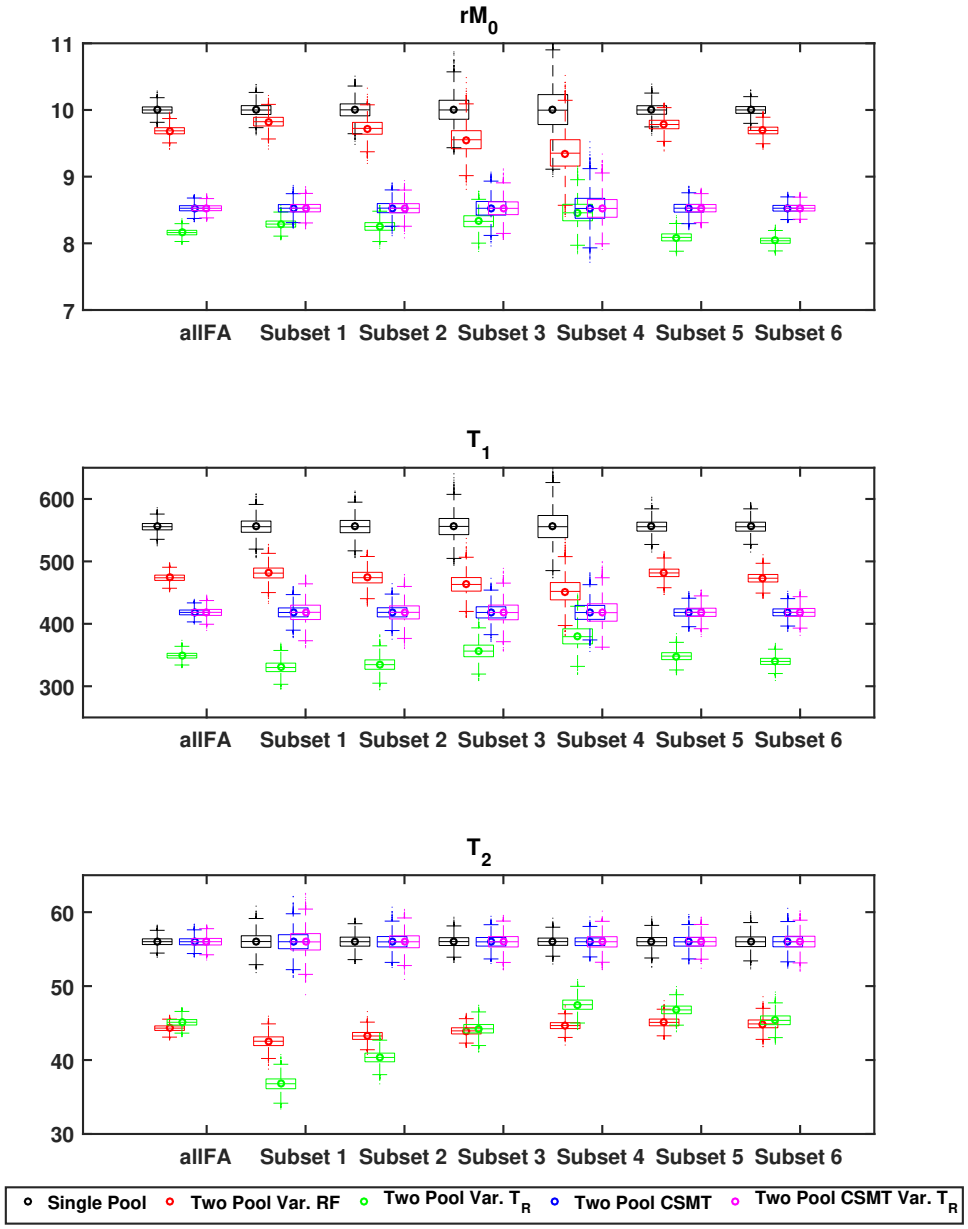

Figure 6.3: Comparison between the obtained apparent rM_0 (top), T_1 (middle) and T_2 (bottom) for the different subsets when estimating single-pool JSR parameters from simulated measurements using single-pool model (black), two-pool model with varying RF-power (red), two-pool model fixed power with $T_R^{SPGR} = 14.0ms$ and $T_R^{SSFP} = 3.5ms$ (green), CSMT with $T_R^{SPGR} = T_R^{SSFP}$ (blue) and CSMT with $T_R^{SPGR} = 14.0ms$ and $T_R^{SSFP} = 3.5ms$. Note that non-CSMT conditions are subject to systematic perturbations in distribution which depend on measurement parameters. This is removed under CSMT conditions.

2) Systematic underestimation of the estimated T_2;

Once obtained under CSMT conditions (blue and magenta distributions), it is

striking to see that single-pool model assumptions converge to apparent M_0^{app} and T_1^{app} values which, although systematically lower, remain constant independently of the subset used to calculate them. Also, the CSMT approach is expected to remove all traces of T_2 bias (as expected from Equations 6.24) as well as variations for different subsets of measurements. For both the single-pool model and the two-pool model under CSMT conditions variations in median of estimated M_0^{app}, T_1^{app} and T_2 for different subsets are $\leq 0.1ms$ giving confidence that under fixed CSMT sampling conditions, the two-pool model of magnetization effectively "behaves" as single-pool model with an apparent M_0^{app} and T_1^{app}.

6.3.3 Phantom Validation

Phantom validation aimed to evaluate, in a controlled and motion free environment, the consequences of CSMT sampling conditions. A similar comparison to the one preformed in the numerical validation section (Figure 6.3) is performed in phantom and summarised in Figure 6.4. A hand-drawn circular ROI ($\approx 10mL$

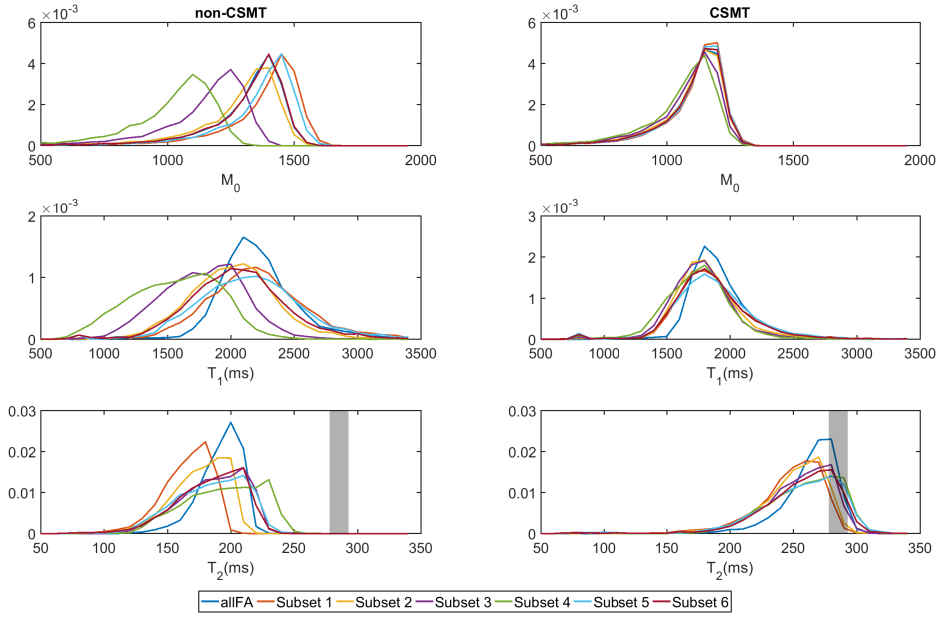

Figure 6.4: Comparison between the obtained apparent M_0 (top row), T_1 (middle row) and apparent T_2 (bottom row) distributions of JSR estimation with data obtained with conventional Block pulse excitation (left column) and proposed non-selective MB excitation (right column). Gray bar corresponds to mean $\pm$ 2 standard deviations of estimated T_2 using multi-echo Spin-Echo data (CPMG).

in volume) at the centre of the phantom (where B_1 and B_0 variations are expected to be mitigated) was defined and used to estimate frequency distributions of the relaxometry parameters obtained for data both under non-CSMT (left col-

umn) and CSMT (right column) sampling regimes. For all employed sequences a $T_R = 7.0ms$ was applied. Parameter estimates were then obtained using the JSR approach for all subsets of Table 6.2. Top, middle and bottom row correspond respectively to M_0, T_1 and T_2. Note that, as expected from Figure 6.3, CSMT conditions induce apparent M_0^{app} and T_1^{app} values which are systematically lower but consistent independent of the flip angles used to estimate the underlying relaxation times. This can be seen as M_0^{app} and T_1^{app} histograms are overlaid for all subsets when CSMT conditions are ensured. Furthermore, the expected shift of T_2 distribution towards longer values, which are more in accordance with spin-echo estimation (Gray bar in bottom graphs of Figure 6.4 corresponds to mean $\pm$ 2 standard deviations of estimated T_2 using multi-echo Spin-Echo approach as defined in the Methods section of Chapter 5), is also observed corroborating the observed behaviour of the numerical simulations performed.

Figure 6.5 demonstrates the signal evolution as a function of all flip angles (Table 6.2), for a representative voxel in the centre of the imaged phantom. The graph on the left corresponds to data sampled using conventional block pulse excitation while on the right data sampled using the proposed CSMT conditions can be seen. Measured data is represented as open circles and estimated model (obtained using all available data) as solid lines. Squared residuals at each flip angle are highlighted as black open circles. Visual comparison between both

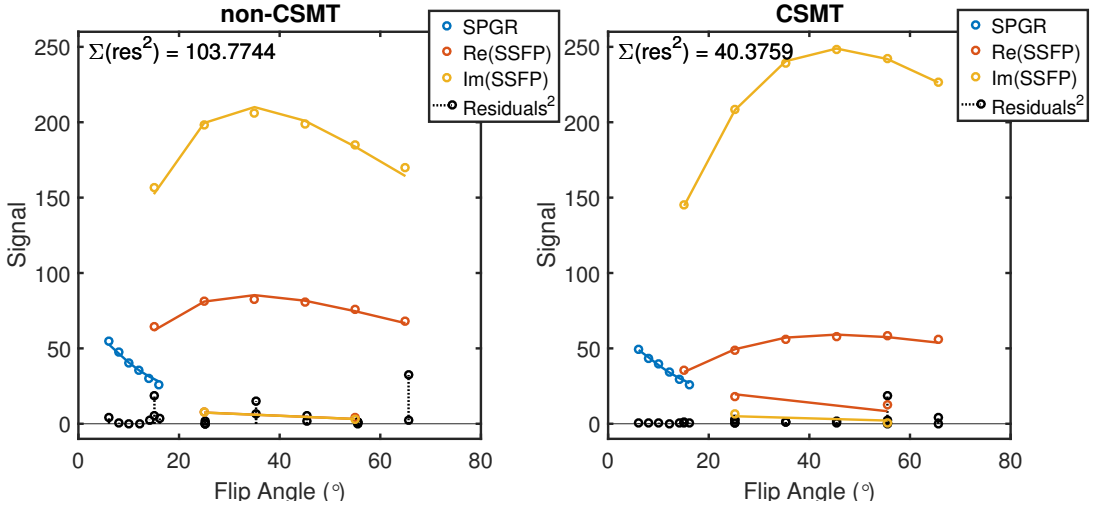

Figure 6.5: Comparison between data acquire (open circles) using conventional Block Pulse (left) and proposed MB excitation (right) as a function of flip angle. Overlaid solid lines represent obtained JSR fit with corresponding squared residuals represented shown as black circles. The total sum of the squared residuals is highlighted to demonstrate the difference in estimation performance.

plots highlights the fact that data sampled under CSMT conditions allows the fitting algorithm to obtain a solution that better explains all measured data. This

can be, as a first naive inspection, confirmed as overall the solid lines seem to less consistently overlay the measured data on the left graph (non-CSMT) when compared to the right graph (CSMT). This is further validated with an observed reduction in the spread of the squared residuals. In fact, for the considered voxel, the total sum of the squared residuals is reduced from 103.8 under non-CSMT conditions to 40.4 for CSMT scenario. Furthermore, taking a small patch of ≈ 100 voxels, the median value of the sum of squared residuals is reduced by 65% demonstrating that CSMT conditions improve estimation robustness.

Figure 6.6 represents a box-plot summary comparison of the change in M_0^{app} and T_1^{app} that can be obtained when sampling the SPGR flip angles of Table 6.2 using both conventional hard pulses with fixed duration and CSMT conditions at different RF-pulse powers. From Figure 6.6 it is evident, not only that there is an

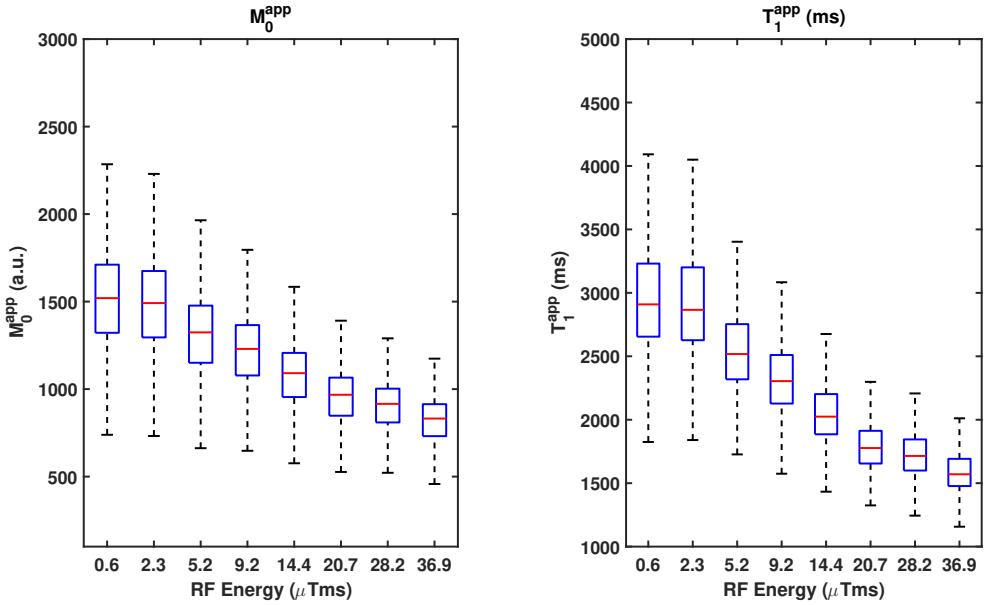

Figure 6.6: Box-plot comparison of DESPOT1 estimated M_0^{app} and T_1^{app} as a function of applied RF pulse power. Distribution parameters were obtained from a hand-drawn circular ROI in the centre of the used phantom. For the applied $T_R^{SPGR} = 7.0ms$ up to a 50% decrease in T_1^{app} can be obtained given the SAR constraints of our system.

apparent M_0^{app} and T_1^{app} which depends on the amount of RF energy applied, but also that the change seen in M_0^{app} and T_1^{app} is not solely a consequence of the considered JSR approach but can be induced in other methods of relaxometry such as DESPOT1.

6.3.4 *In Vivo* Validation

In vivo validation was sought by directly comparing the different subsets presented in Table 6.2 both under non-CSMT and CSMT conditions. For reference, exemplar estimation maps obtained using all measured data (top row of Table 6.2) are shown in Figure 6.7 (Note that $M_0 = \sqrt{(\rho^r)^2 + (\rho^i)^2}$). Here, direct visual comparison between the obtained M_0^{app} (top), T_1^{app} (middle) and T_2^{app} (bottom), under both conventional block pulse excitation (left) and CSMT (right), is presented. From Figure 6.7 it can be seen that, once under CSMT conditions (in this case the proposed MB excitation jointly with fixed T_R) M_0^{app} and T_1^{app} maps have overall lower values but, both present less of a "grainy" texture in the mid-brain regions (SNR is expected to be lower in this region due to the receive sensitivity properties of the head coil that was used) compared to conventional block pulse excitation procedure. Also T_2^{app} values are consistently higher when estimating data under CSMT. Both these effects are expected from Figure 6.3 and validate our initial hypothesis that CSMT conditions allow a more internally consistent estimation of relaxation times.

A key aspiration for the CSMT approach is that relaxation properties measured in vivo would be more stable and robust against incidental effects caused by changing the operating conditions (acquisition parameters). To explore this in vivo histograms were constructed for White-Matter specific M_0^{app}, T_1^{app} and T_2 values in the 3 Healthy-Volunteers that had been studied. WM is expected to be more sensitive to different MT sampling conditions compared to GM. Such histograms were extracted for all estimations performed using different data subsets and these are summarised in Figure 6.8 (non-CSMT on the left and CSMT on the right). There are separate pairs of columns for each Healthy Volunteer, with each row presenting histograms for M_0^{app} (top), T_1^{app} (middle) and T_2^{app} (bottom). All the histograms are colour colour-coded such that each colour represents a row entry of Table 6.2. Systematic offsets are evident in the apparent M_0^{app} and T_1 histograms when data is sampled using the conventional block pulse. These observed variations in M_0^{app} and T_1^{app} were removed under the proposed CSMT conditions resulting in all the histograms systematically overlapping each other. As expected from both numerical simulations (Figure 6.3) and phantom data (Figure 6.4), a shift in apparent T_2 estimation is also observed towards higher relaxation values when data is sampled under CSMT conditions. In fact, the reported shift in apparent T_2, induces results that are more consistent with previously published spin-echo data [72].

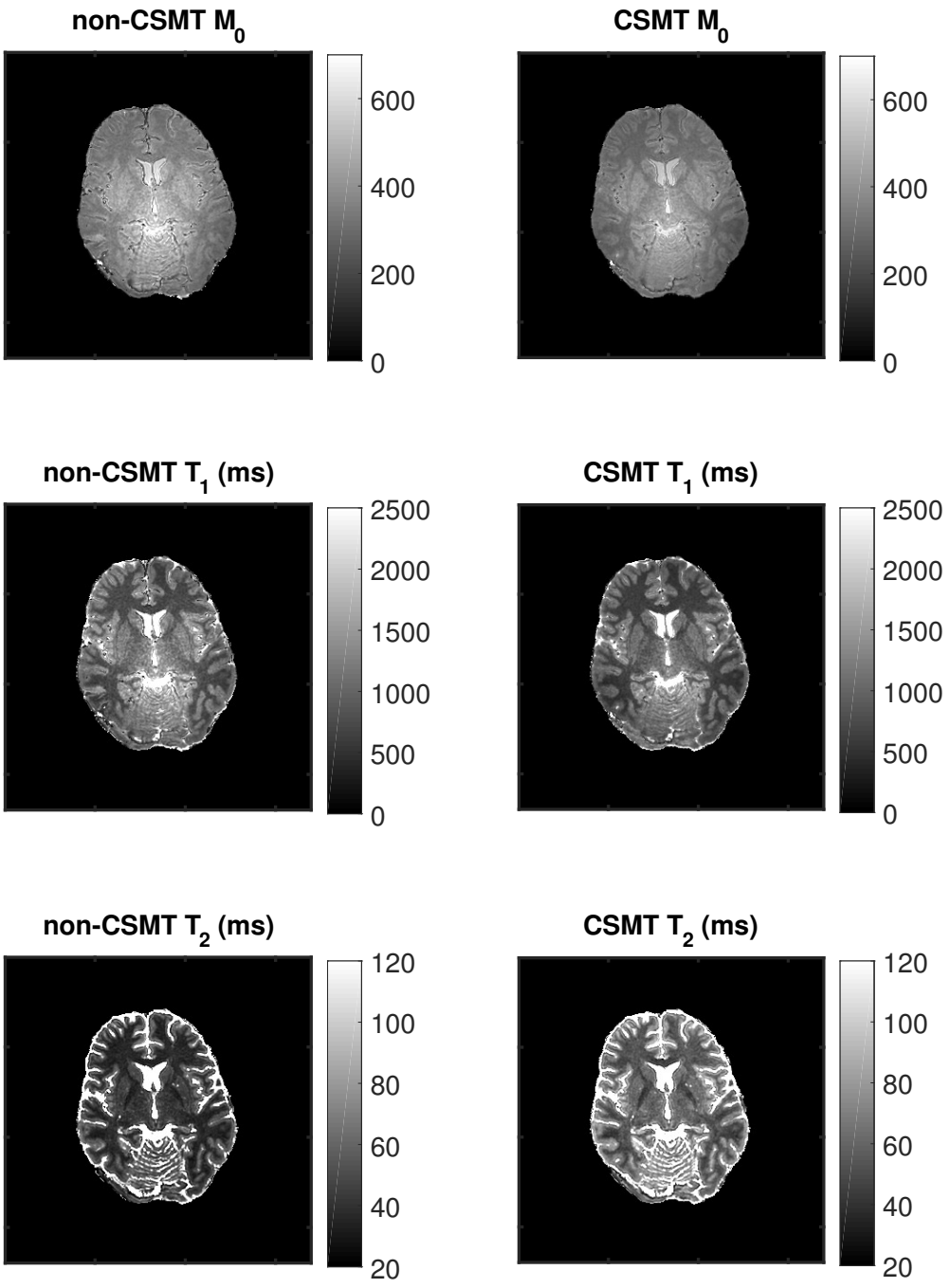

Figure 6.7: Visual comparison, on an exemplar axial slice, between the obtained M_0 (Top row), T_1 (Middle row) and T_2 (Bottom row) distributions of JSR estimation with data obtained with Block pulse excitation (left column) and proposed non-selective MB excitation (right column).

6.4 Discussion

The current chapter directly addresses the fact that biological tissues are not correctly characterized by single pool assumptions which might help explain why a

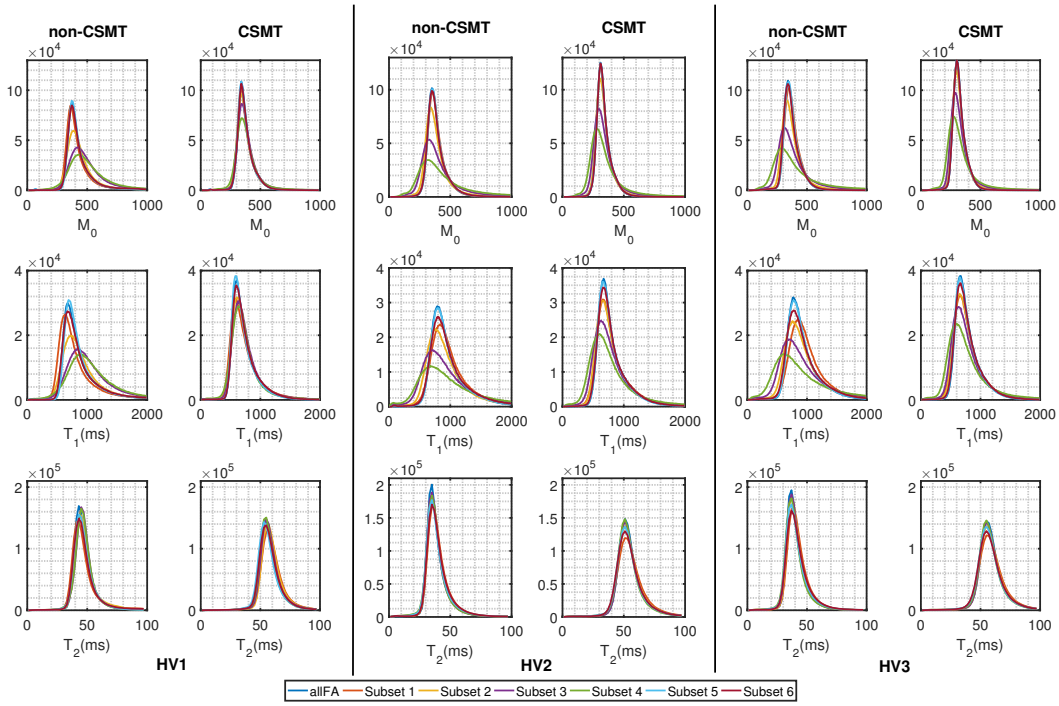

Figure 6.8: Comparison between the obtained T_1 and T_2 WM distributions of JSR estimation with data obtained with Block pulse excitation and proposed non-selective MB excitation.

consensus between different T_1 sampling strategies has still to be found [6]. In fact, this has already been reported at the introduction of MT weighting as a new source of imaging contrast in 1989 by S. Wolff and R. Balaban [100] and further explored by X. Ou and D. Gochberg in 2008 [99]. Their work noticed that T_1 of the free-pool cannot be assessed using conventional methods and only an apparent $T_1(T_R \rightarrow \infty)$ can be measured. The consequence of this, is that even the considered gold standard methods, don't report on the T_1 of the free pool but instead systematically converge to a solution which, although independent of the RF sampling conditions, still depends on exchange and relaxation times of the different pools (as long as $T_R \rightarrow \infty$). One approach to allow tissue complexity to be addressed involves characterizing the tissue response by multiple-pool system [7, 8, 87, 91–93, 103] of magnetization where each pool is characterized by its intrinsic recovery time and exchange is allowed between them. This approach however, increases the number of parameters to be estimated (and as a consequence the number of minimum measurements required) hindering clinical applicability. In the work here presented, instead of following an approach which aims to characterize the multi-compartment behaviour, it is hypothesised that single compartment M_0 and T_1 assumptions can be made valid in biological tissues as long as constant saturation of the background pool is ensured constant. A mathematical description of the binary-spin-model under constant

saturation of the background pool is derived (Equation 6.24) where it is identified that single-pool assumptions can be valid (governed by M_0^{app} and T_1^{app}) across different measurements as long as $< W > \frac{T_{RF}}{T_R}$ is maintained fixed. With this in mind it is then possible (given that CSMT conditions are ensured), to create a regime under which single-pool assumptions are robust and reproducible. To validate this, the work developed throughout this chapter aimed to both:

- Evaluate the effect of single-pool assumptions in signals generated using a two-pool magnetization model;and
- Propose the use of sampling conditions that ensure Constant Saturation of Magnetization Transfer (CSMT) effects and therefore allowing single pool assumptions to be valid;

Regarding the first point, we derive a two-pool SPGR and SSFP model (Equations 6.18 and 6.19 respectively) based on previous published work [7,87,101]. It was then conjectured that CSMT conditions can be attained by keeping the exponential terms of both excitation and exchange operators (respectively $R(T_{RF})$ and $Ex(t)$ of Equation 6.16 and 6.14) constant and we sought to numerically verify our assumption by applying JSR estimation of Chapter 5 in two-pool data generated based on Table 6.2. We've identified that constant saturation of the background pool is obtained as long as the ratio $< W > T_{RF}/T_R$ is maintained constant. With this in mind, a single-pool model (black distributions in Figure 6.3) was generated and fitted to itself to prove the self-consistency of our fitting approach. From the distributions of Figure 6.3 it can be inferred that additive noise contributes to the spread of estimation but doesn't bias the end result since the estimation median overlays the estimated value under an ideal noiseless scenario (open circles in Figure 6.3) for all datasets considered. Two-pool data was simulated with the constraint that $T_{1f} = T_{1r}$ [87]. Based on conventional non-CSMT sampling conditions (red distributions in Figure 6.3), it can be seen that final estimated M_0, T_1 and T_2 not only differ significantly from single-pool model but are inconsistent across different subsets (flip angle measurements). This is due the varying saturation of the restricted pool induced through the exponential term of Equation 6.16 which is different for each applied flip angle and therefore induces inconsistencies which can not be interpreted by the single-pool model. A similar effect is observed if RF energy is kept constant and T_R is varied between measurements (green distributions). Enabling CSMT conditions by fixing both $< W >$ and T_R for all employed sequences (blue distributions in Figure 6.3) induces apparent M_0 and T_1 which are independent of the subset used for relaxometry estimation. Furthermore, bias presented in T_2 estimation is expected to be completely removed once CSMT is ensured. From Equations 6.24, 6.28 and 6.27 it is deduced that,

under CSMT conditions, as long as $< W > \frac{T_{RF}}{T_R}$ is maintained fixed the same M_0^{app} and T_1^{app} are expected to be estimated. This is in fact demonstrated in the magenta distribution of Figure 6.3 where data was simulated with $T_R^{SPGR} = 14.0ms$, $T_R^{SSFP} = 3.5ms$ and $< W >$ scaled accordingly for each sequence. Not only is the result stable across different subsets of that data (even when different T_R are employed between sequences) but also, it converges to the same solution of CSMT with fixed T_R between measurements. The obtained CSMT estimated M_0^{app} and T_1^{app} also converge to the predicted values from equations 6.28 and 6.27 respectively validating our CSMT single pool model derivation.

The second part of this chapter focused on the experimental implementation and validation of CSMT conditions. Although constant exchange bias is promptly ensured by enforcing equal T_R between all sequences applied, to our knowledge, no work has been reported on ensuring equal $< W >$ between acquisitions. Although not necessary to ensure CSMT conditions as T_R can be balanced for different flip angles in order to ensure constant $< W > T_{RF}/T_R$ ratio, it was felt that this approach was too restrictive (as T_R allowed would be constrained by RF energy for the flip angle prescribed and vice-versa). To achieve this, we defined a non-selective multi-band excitation that balances the power applied on- and off-resonance ($\Delta = 0$ and $\Delta \neq 0$) to achieve the desired flip angle while maintaining the total RF energy constant. For ease of implementation, a three band pulse was designed (the applied cosine modulation allows the RF pulse envelope to be kept real) and the implications of using a single off-resonance band vs symmetrical double off-resonance bands remain to be explored [105–110]. Further exploration of optimal pulse design may prove to be beneficial but since this is a refinement rather than a core requirement for proof of principal demonstration it was considered outside the scope of the work presented here. To ensure a controlled and motion free environment, a first experimental validation was performed in the in-house built phantom defined in the Methods section. Figure 6.6 demonstrates not only that it is possible to vary M_0^{app} and T_1^{app} as a function of the RF power applied (given a fixed T_R) but also that this effect is observed on other relaxometry methods different from JSR. Figure 6.4 sought not only to validate our assumption that CSMT conditions induce robust estimation, but also that CSMT conditions can be achieved by enforcing equal RF power between all measurements. It is striking to see that, as expected from numerical simulations (Figure 6.3), under non-CSMT conditions M_0^{app}, T_1^{app} and T_2^{app} vary depending on the subset of flip angles chosen to estimate the data. Also, estimated T_2 is significantly shorter compared the estimation based on spin echo measurements. Once constant MT saturation conditions are assured, all histograms systematically overlap

independently of the subset used and the distribution of each histogram is narrower. On the other hand, a shift in the T_2 distribution towards values obtained through Spin Echo measurement is observed. A residual bias can still be observed in T_2 estimation which might be attributed to either imperfect finite RF pulse duration correction in the JSR model, or residual slice profile effects in the Spin Echo acquisition. Residual fluctuations can still be observed in M_0 and T_1 CSMT estimation which might be attributed to the fact that the background pool absorption line-shape is not completely flat. Although present, these variations are significantly smaller compared to the ones observed under non-CSMT conditions. In fact, guaranteeing CSMT conditions, although altering the expected flip angle response (different shape of SPGR and SSFP curves in Figure 6.2 and 6.5), allows single-pool assumptions to be valid as all measurements experience the same M_0^{app} and T_1^{app} effects. The robustness of these sampling conditions are further validated in Figure 6.5 where data and estimated models for a single voxel measured under non- and CSMT conditions are directly compared. Visual inspection clearly demonstrates that under non-CSMT conditions, although a solution is found which explains the measured data (displayed as coloured circles), the solid lines that represent the estimated model don't overlap most of the measured data. On the other hand, data sampled under CSMT conditions, allows a solution to be found where most of the sampled data is overlaid by the solid lines representing the estimated model. This is further validated when comparing the residual distributions between non- and CSMT conditions which are clearly smaller for the latter. In fact, the median value of the squared residuals distribution of ≈ 100 voxels demonstrated a 65% decrease when comparing CSMT vs. non-CSMT sampling conditions. *In vivo* validation aimed to reproduce the results obtained in phantom in three healthy human subjects. Figure 6.7 directly compares, in an exemplar axial slice, final estimated relaxation maps sampled under both conventional and CSMT conditions. As expected from the phantom experiment (where a more narrow M_0^{app} and T_1^{app} was observed), visual comparison clearly demonstrates lower estimation variance when CSMT is ensured. Also, a clear increase in overall T_2^{app} can be observed which is more in line with previously reported spin-echo values [72]. This is further confirmed in Figure 6.8 where the same behaviour is observed *in vivo*. Here, WM specific histograms for M_0^{app}, T_1^{app} and T_2^{app} of three different Healthy Volunteers with data acquired under both conventional and CSMT conditions are compared. Although, validated in numerical simulations, due to time constraints, it was not possible to experimentally validate that acquiring relaxometry measurements at different T_R and $< W >$ and fixed $< W > \frac{T_{RF}}{T_R}$ would induce the same estimation result. This is currently work in progress and it has implications not only for acquisition time constraints

(in Chapter 5 it was demonstrated that optimal acquisition protocol systematically converges to a situation where T_R^{SSFP} is minimized), but also, for new ways of tissue relaxometry such as MR Fingerprinting [89] where a wide range of repetition times and excitation angles are employed. Given the work here presented, MRF is expected to be sensitive to estimation fluctuations depending of sampling conditions which should be avoided by ensuring a CSMT framework is employed. Throughout this work, although flip angle corrections are employed for the rotation induced in the free pool, the spatial variation of B_1 will necessarily result in $< W >$ spatial dependency. Therefore, from Equations 6.27 and 6.28 it is expected there will be a residual spatial variation in the final estimated M_0^{app} and R_1^{app} maps due to this effect. This effect can be minimized at low field strength ($\leq 1.5T$) as spatial variations of transmit field are mitigated and my hinder the application of MR relaxometry at high field strengths ($\geq 3.0T$).

The proposed use of non-selective MB excitation might prove beneficial to probe new types of MT-weighted contrast. One can envision, for example, that a SPGR acquisitions acquired at different RF power levels might induce different WM/GM contrasts due to the different amount of MT observed for both tissues. Also, the change in M_0^{app} and T_1^{app} as a function of deposited RF power might prove to be a significant marker for MT effects by itself. Although developed for single pool relaxomtry, the CSMT framework has implications for two-pool model estimation. The flexibility of exchanging both RF energy and imaging timings to induce different MT effects in the observed signal of short T_R steady-state sequences may pave the way for more efficient ways to probe multi-compartment estimation.

6.5 Conclusion

The work here presented demonstrates that a classical description of a single M_0 and T_1 relaxation is not feasible in biological tissues as different amounts of RF power (commonly applied to vary the flip angles as needed for the sampling scheme adopted), induce unavoidable M_0^{app} and T_1^{app} variations across measurements which, if not taken into consideration, make measured data inconsistent with single-pool assumptions. This chapter explored the effects of single-pool relaxometry assumptions in data generated using a two-pool MT model description and proposed the use of a Constant Saturation of Magnetization Transfer (CSMT) framework in order to ensure single-pool assumptions can be valid in spite of the complex nature of biological tissues. A mathematical description was

then derived for the expected magnetization evolution given that the restricted pool magnetization is kept under constant conditions while the visible pool is directly manipulated. This makes clear the identification of observed M_0^{app} and T_1^{app} with the imposed MT conditions and emphasises that such measurements should be qualified by, perhaps even be defined by, the RF power ($< W > \frac{T_{RF}}{T_R}$) applied. Repetition time is easily controllable at the expense of acquisition time, and our non-selective MB excitation is shown to allow customization of the pulse energy $< W > T_{RF}$ giving full flexibility to design relaxometry protocols at fixed values of RF power. Relaxometry under CSMT conditions allows precise, accurate and reproducible M_0^{app}, T_1^{app} and T_2 estimation and is a framework that potential to bring a consensus to the panoply of reported relaxometry values throughout the literature [6]. Evidence to confirm this conjecture will require much more extensive future study.

Chapter 7

Conclusion

This chapter concludes the work presented throughout this thesis and discusses possible directions where the findings here demonstrated can lead to future work.

The initial goal of this work was to, given their time efficiency, develop a framework where relaxometry gradient echo methods such as DESPOT1 and DESPOT2 could be optimized for a specific range of relaxation times. This comes in line with the work developed in the Centre for the Developing Brain (CDB), where this research project was developed. As the research in the CDB heavily focuses in Neonatal imaging, the ability to efficiently characterize relaxation times becomes of interest. We focused primarily on single component methods due to previous exploration which demonstrated instability of multi-compartment approaches [10] and was corroborated by the work presented in [9]. Bases on this and the fact that Neonatal brain relaxation times are known to differ from the ones presented in adults [111] motivated the work presented in Chapter 4. In this Chapter, a mathematical framework was developed to allow tissue specific relaxometry protocols to be developed. This was validated by numerical, Phantom and *in vivo* studies and good agreement was found between theory and practice (expect for systematic biases which we attribute mainly to MT effects). It was felt however, that the stepwise DESPOT1-DESPOT2 approach to estimate relaxation times was inefficient as T_1 information present in SSFP acquisitions was being ignored. With this in mind, a big effort was applied in guaranteeing equal sampling conditions between SPGR and SSFP acquisitions in order to develop the Joint System Relaxometry (JSR) framework presented in Chapter 5. This work has been peer-reviewed and published in [11]. Here,the immediate effect of jointly evaluating SPGR and SSFP acquisitions, in the proposed JSR framework, was shown to outperform conventional DESPOT1/2 in order to produce

relaxation maps with improved precision given the same acquisition data. The CRLB framework presented in Chapter 4 was also applied not only linking the work between the two chapters but demonstrating that it is a robust an flexible approach that can be easily adapted to different relaxometry scenarios. The proposed framework enhances both precision and efficiency making it an appealing candidate for clinical use as sub-millimetre relaxation maps are achievable in an acquisition time ≤ 11 minutes. Although the JSR approach proved to be reliable and precise, systematic fluctuations were still observed for different acquisition parameters employed. These variations motivated the exploration of the work developed throughout Chapter 6. In this final work chapter, it was hypothesised that observed estimation fluctuations were due to MT induced inconsistencies that invalidated single pool assumptions. This is shown both numerically and experimentally. It was then hypothesised, and mathematically described, that if constant saturation of the background pool is ensured, effectively, a two-pool magnetization system behaves as a single-pool system with M_0^{app} and R_1^{app} (Equation 6.24) that depend both on tissue parameters and total RF energy deposited per T_R ($< W > \frac{T_{RF}}{T_R}$). It was shown that pulse energy can be controlled by means of non-selective multi-band excitation. This approach to RF excitation, although not conventional, allows direct control of all parameters of the $< W > \frac{T_{RF}}{T_R}$ ratio. It is therefore suggested and shown that, in complex samples, the applied RF energy per excitation time must be reported, specially in relaxometry measurements in multi-centre studies where an absolute reported value that characterizes the measured object is sought.

7.1 Future Work

The work presented summarizes a flow of developments where incremental steps lead from a summary of some of the current relaxometry gradient echo approaches in Chapter 3 to the original work presented throughout Chapters 4 to 6. Special interest arises from the work presented in Chapter 6 where the results presented provide support for the suggestion that the tools to probe complex biological tissues at fixed RF powers can pave the way for a new relaxometry paradigm. Some interesting research questions still remain open, and a small list of the ones more relevant to my current research interests are summarized below:

(i) **Multi-site, multi-vender testing of the CSMT approach:** The work presented in this thesis showed that the CSMT approach can stabilise Variable Flip Angle (VFA) based relaxometry methods. This shows promise for

helping to achieve more reliable and robust quantitative MRI performance for clinical use and for clinical trials and other studies. That promise really requires to be tested by performing pilot studies across centres and on different scanner platforms. Also a standardised labelling system will need to be developed so that matched conditions can be prescribed and identified as having been achieved.

(ii) **JSR + B1:** in Chapter 5 it was mentioned that a small extension of JSR framework was explored where MPRAGE was employed to allow B_1 estimation discarding the need for an external calibration map. Although feasible through numerical simulation, this approach was proven to be unreliable in experiments as different inversion timings for the MPRAGE induced systematic offsets which were attributed to MT effects. Under CSMT conditions however, the observed inconsistencies in the estimated maps are expected to disappear allowing the development of a robust, self-calibrated framework for single-pool relaxometry where M_0^{app}, T_1^{app}, T_2, B_0 and B_1 maps are estimated in a 10 to 15 minutes scanning session at sub-millimetre spatial resolution;

(iii) **MRF under CSMT conditions:** A different and interesting line of investigation, given the wide interest demonstrated by the MR community, is the evaluation of the effects of non-CSMT vs CSMT conditions in MR Fingerprinting. It is expected that the currently employed non-CSMT conditions will induce estimation fluctuations which will depend on the acquisition scheme. This is expected to be mitigated under a MRF-CSMT regime;

(iv) **MRF vs. JSR:** MRF has been presented as a fast and reliable way to obtain accurate parametric maps. This is precisely the goal of the developed JSR approach and a robust comparison between MRF and JSR time efficiency will also be of interest;

(v) **qMT: Two-Pool Estimation under CSMT regime:** Although steady state methods have been employed to characterize two-pool model estimation parameters, they have mainly made use of off-resonance preparation pulses (to induce MT weighting) which not only interrupt the steady state making the scan time inefficient but also make the analytical solutions more complex. In the work presented here the CSMT framework was deployed to achieve constant saturation conditions in order to make VFA data self consistent. However, the same approach could be deployed to deliberately vary the bound pool saturation in a controlled way from acquisition to acquisition. This may enable the design of a robust and reliable way to have steady-state

methods used to probe exchange rates between macro-molecular pools and free water;

(vi) **Revisiting MT Ratio imaging:** Current MT ratio (MTR) imaging employs MPRAGE-type time structure where an off-resonance preparation pulse is applied between small tip-angle pulses that sample the required data. The proposed non-selective MB pulse might prove to more time efficient as a Steady-State time structure can be employed at different RF-powers that will induce MT weighting. Also when calibrated using the CSMT-JSR approach, perhaps a more stable and consistent MTR framework could be achieved with more reproducible values achieved between scanning centres and across manufacturers;

7.2 Final Remarks

The family of short T_R relaxometry methods, which include VFA, DESPOT (and its various sub-variants that was the starting point for this work), Magnetic Resonance Finger printing, Multi Parametric Mapping and others, have the very great virtue of providing high resolution 3D T1 and T2 maps in examination times that are eminently feasible to be applied to wide classes of clinical studies. In this work we have tried to explore some limiting features of this type of approaches and to, most specifically, improve on their estimation precision, accuracy and reproducibility. The dynamic nature of short T_R methods makes them specially susceptible to experimental settings. We therefore hope that, by redefining relaxometry under a new measurement regime where careful control of not only the imaging timings but also deposited energy, it becomes possible to not only bring a consensus between different relaxometry methods but also move away from classic qualitative evaluation of MR images and accurately characterize the brain with quantitative measures.

Bibliography

[1] M. D. Meadowcroft, N. J. Mutic, D. C. Bigler, J.-L. Wang, Z. Simmons, J. R. Connor, and Q. X. Yang, "Histological-MRI correlation in the primary motor cortex of patients with amyotrophic lateral sclerosis.," *Journal of magnetic resonance imaging : JMRI*, vol. 00, pp. 1–11, 3 2014.

[2] H. Kitzler, J. Su, M. Zeineh, and C. Harper-Little, "Deficient MWF mapping in multiple sclerosis using 3D whole-brain multi-component relaxation MRI," *NeuroImage*, vol. 59, pp. 2670–2677, 2 2012.

[3] G. Helms, H. Dathe, N. Weiskopf, and P. Dechent, "Identification of signal bias in the variable flip angle method by linear display of the algebraic ernst equation," *Magnetic Resonance in Medicine*, vol. 66, no. 3, pp. 669–677, 2011.

[4] S. C. L. Deoni, B. K. Rutt, and T. M. Peters, "Rapid combined T1 and T2 mapping using gradient recalled acquisition in the steady state," *Magnetic Resonance in Medicine*, vol. 49, no. 3, pp. 515–526, 2003.

[5] N. Weiskopf, J. Suckling, G. Williams, M. M. Correia M., B. Inkster, R. Tait, C. Ooi, E. T. Bullmore T., and A. Lutti, "Quantitative multi-parameter mapping of R1, PD*, MT, and R2* at 3T: A multi-center validation," *Frontiers in Neuroscience*, no. 7 JUN, 2013.

[6] N. Stikov, M. Boudreau, I. R. Levesque, C. L. Tardif, J. K. Barral, and G. B. Pike, "On the accuracy of T1 mapping: Searching for common ground," *Magnetic Resonance in Medicine*, vol. 73, pp. 514–522, 2 2015.

[7] J. G. Sled and G. B. Pike, "Quantitative imaging of magnetization transfer exchange and relaxation properties in vivo using MRI.," *Magnetic resonance in medicine : official journal of the Society of Magnetic Resonance in Medicine / Society of Magnetic Resonance in Medicine*, vol. 46, no. 5, pp. 923–31, 2001.

[8] S. C. L. Deoni, L. Matthews, and S. H. Kolind, "One component? Two components? Three? the effect of including a nonexchanging "free" water

component in multicomponent driven equilibrium single pulse observation of T1 and T2," *Magnetic Resonance in Medicine*, vol. 70, pp. 147–154, 7 2013.

[9] C. Lankford and M. Does, "On the inherent precision of mcDESPOT," *Magnetic Resonance in Medicine*, vol. 69, no. 1, p. 127136, 2013.

[10] R. P. A. G. Teixeira, *Advanced Brain Imaging : From Adult to Neonates (MSc thesis)*. 2013.

[11] R. P. A. G. Teixeira, S. J. Malik, and J. V. Hajnal, "Joint system relaxometry (JSR) and Cramer-Rao lower bound optimization of sequence parameters: A framework for enhanced precision of DESPOT T1 and T2 estimation," *Magnetic Resonance in Medicine*, vol. 00, 2017.

[12] E. Haacke, R. Brown, M. Thompson, and R. Venkatesan, "Magnetic resonance imaging: physical principles and sequence design. 1999," *New York: A John Wiley and Sons*, 6 1999.

[13] D. I. Hoult and N. S. Ginsberg, "The quantum origins of the free induction decay signal and spin noise.," *Journal of magnetic resonance (San Diego, Calif. : 1997)*, vol. 148, no. 1, pp. 182–199, 2001.

[14] D. J. Siminovitch, "Rotations in NMR: Part II. Applications of the Euler-Rodrigues parameters," *Concepts in Magnetic Resonance*, vol. 9, no. 4, pp. 211–225, 1997.

[15] D. McRobbie, *MRI from Picture to Proton*. Cambridge University Press, 2 ed., 2 2007.

[16] M. Vlaardingerbroek and J. Boer, *Magnetic Resonance Imaging: Theory and Practice*. Springer-Verlag, 1999.

[17] M. Bernstein, K. King, and X. Zhou, *Handbook of MRI pulse sequences*. Elsevier, 9 2004.

[18] E. Hahn, "Spin echoes," *Physical Review*, vol. 297, no. 1946, 1950.

[19] M. Weigel, "Extended phase graphs: Dephasing, RF pulses, and echoes - Pure and simple," *Journal of Magnetic Resonance Imaging*, vol. 41, pp. 266–295, 4 2015.

[20] J. Hennig, "Echoes-how to generate, recognize, use or avoid them in MR-imaging sequences. Part I: Fundamental and not so fundamental properties

of spin echoes," *Concepts in Magnetic Resonance*, vol. 3, no. 3, p. 125143, 1991.

[21] E. Haacke, A. Hopkins, and S. Lai, "2D and 3D high resolution gradient echo functional imaging of the brain: venous contributions to signal in motor cortex studies," *NMR in Biomedicine*, vol. 7, no. 1-2, p. 5462, 1994.

[22] J. Hennig, "Echoes-how to generate, recognize, use or avoid them in MR-imaging sequences. Part II: Echoes in imaging sequences," *Concepts in Magnetic Resonance*, vol. 3, no. 4, p. 179192, 1991.

[23] J. Hennig, M. Weigel, and K. Scheffler, "angles for echo trains with predefined amplitudes with the extended phase graph (EPG) algorithm: Principles and applications to hyperecho and TRAPS sequences," *Magnetic Resonance in Medicine*, vol. 51, no. 1, p. 6880, 2004.

[24] K. Scheffler, "A pictorial description of steady-states in rapid magnetic resonance imaging," *Concepts in Magnetic Resonance*, vol. 11, no. 5, p. 291304, 1999.

[25] Y. Zur, M. L. Wood, and L. J. Neuringer, "Spoiling of transverse magnetization in steady-state sequences.," *Magnetic Resonance in Medicine*, vol. 21, pp. 251–63, 10 1991.

[26] A. T. Hess and M. D. Robson, "Hexagonal gradient scheme with RF spoiling improves spoiling performance for high-flip-angle fast gradient echo imaging," 2016.

[27] C. Ganter, "Steady state of gradient echo sequences with radiofrequency phase cycling: Analytical solution, contrast enhancement with partial spoiling," *Magnetic Resonance in Medicine*, vol. 55, no. 1, pp. 98–107, 2006.

[28] J. Homer and M. Beevers, "Driven-equilibrium single-pulse observation of T1 relaxation. A reevaluation of a rapid "new" method for determining NMR spin-lattice relaxation," *Journal of Magnetic Resonance*, vol. 63, pp. 287–297, 6 1985.

[29] R. Spencer and K. Fishbein, "concentrations in systems with chemical exchange using the one-pulse sequence: breakdown of the Ernst model for partial saturation in nuclear magnetic resonance," *Journal of Magnetic Resonance*, vol. 142, pp. 120–135, 1 2000.

[30] K. Scheffler and S. Lehnhardt, "Principles and applications of balanced SSFP techniques," *European radiology*, vol. 13, pp. 2409–2418, 11 2003.

[31] K. Scheffler and J. Hennig, “Is TrueFISP a gradient-echo or a spin-echo sequence?,” *Magnetic Resonance in Medicine*, vol. 49, no. 2, pp. 395–397, 2003.

[32] S. C. Deoni, S. C. Williams, P. Jezzard, J. Suckling, D. G. Murphy, and D. K. Jones, “Standardized structural magnetic resonance imaging in multicentre studies using quantitative T1 and T2 imaging at 1.5T,” *NeuroImage*, vol. 40, pp. 662–671, 4 2008.

[33] M. F. Callaghan, S. Mohammadi, and N. Weiskopf, “Synthetic quantitative MRI through relaxometry modelling,” *NMR in Biomedicine*, vol. 29, no. 12, pp. 1729–1738, 2016.

[34] A. Mezer, J. D. Yeatman, N. Stikov, K. N. Kay, N.-J. Cho, R. F. Dougherty, M. L. Perry, J. Parvizi, L. H. Hua, K. Butts-Pauly, and B. A. Wandell, “Quantifying the local tissue volume and composition in individual brains with magnetic resonance imaging.,” *Nature medicine*, vol. 19, no. 12, pp. 1667–72, 2013.

[35] G. S. Pell, R. S. Briellmann, A. B. Waites, D. F. Abbott, D. P. Lewis, and G. D. Jackson, “Optimized clinical T2 relaxometry with a standard CPMG sequence,” *Journal of Magnetic Resonance Imaging*, vol. 23, no. 2, pp. 248–252, 2006.

[36] K. C. McPhee and A. H. Wilman, “T2 quantification from only proton density and T2-weighted MRI by modelling actual refocusing angles,” *NeuroImage*, vol. 118, pp. 642–650, 2015.

[37] M. N. Uddin, R. Marc Lebel, and A. H. Wilman, “Transverse relaxometry with reduced echo train lengths via stimulated echo compensation,” *Magnetic Resonance in Medicine*, vol. 70, no. 5, pp. 1340–1346, 2013.

[38] H.-L. M. Cheng and G. a. Wright, “Rapid high-resolution T(1) mapping by variable flip angles: accurate and precise measurements in the presence of radiofrequency field inhomogeneity.,” *Magnetic resonance in medicine : official journal of the Society of Magnetic Resonance in Medicine / Society of Magnetic Resonance in Medicine*, vol. 55, pp. 566–74, 3 2006.

[39] H. L. Margaret Cheng, N. Stikov, N. R. Ghugre, and G. A. Wright, “Practical medical applications of quantitative MR relaxometry,” *Journal of Magnetic Resonance Imaging*, vol. 36, no. 4, pp. 805–824, 2012.

[40] R. Heule, C. Ganter, and O. Bieri, “Variable flip angle T1 mapping in the human brain with reduced t2 sensitivity using fast radiofrequency-spoiled gradient echo imaging,” *Magnetic Resonance in Medicine*, vol. 75, no. 4, pp. 1413–1422, 2016.

[41] S. Deoni, T. Peters, and B. Rutt, “Determination of optimal angles for variable nutation proton magnetic spin-lattice, T1, and spin-spin, T2, relaxation times measurement,” *Magnetic Resonance in Medicine*, vol. 51, no. 1, p. 194199, 2004.

[42] S. Baudrexel, S. C. Reitz, S. Hof, R. M. Gracien, V. Fleischer, H. Zimmermann, A. Droby, J. C. Klein, and R. Deichmann, “Quantitative T1 and proton density mapping with direct calculation of radiofrequency coil transmit and receive profiles from two-point variable flip angle data,” 2016.

[43] G. Helms, H. Dathe, K. Kallenberg, and P. Dechent, “High-resolution maps of magnetization transfer with inherent correction for RF inhomogeneity and T1 relaxation obtained from 3D FLASH MRI,” *Magnetic Resonance in Medicine*, vol. 60, no. 6, pp. 1396–1407, 2008.

[44] C. Preibisch and R. Deichmann, “Influence of RF spoiling on the stability and accuracy of T1 mapping based on spoiled FLASH with varying flip angles,” *Magnetic Resonance in Medicine*, vol. 61, pp. 125–135, 1 2009.

[45] V. L. Yarnykh, “Actual flip-angle imaging in the pulsed steady state: A method for rapid three-dimensional mapping of the transmitted radiofrequency field,” *Magnetic Resonance in Medicine*, vol. 57, pp. 192–200, 1 2007.

[46] V. L. Yarnykh, “Optimal radiofrequency and gradient spoiling for improved accuracy of T1 and B1 measurements using fast steady-state techniques,” *Magnetic Resonance in Medicine*, vol. 63, pp. 1610–1626, 6 2010.

[47] C. H. Cunningham, J. M. Pauly, and K. S. Nayak, “Saturated double-angle method for rapid B1+ mapping,” *Magnetic Resonance in Medicine*, vol. 55, no. 6, pp. 1326–1333, 2006.

[48] K. Nehrke and P. Börnert, “DREAM-a novel approach for robust, ultrafast, multislice B1 mapping,” *Magnetic Resonance in Medicine*, vol. 68, no. 5, pp. 1517–1526, 2012.

[49] S. C. L. Deoni, “High-resolution T1 mapping of the brain at 3T with driven equilibrium single pulse observation of T1 with high-speed incorporation

of RF field inhomogeneities (DESPOT1-HIFI)," *Journal of Magnetic Resonance Imaging*, vol. 26, no. 4, pp. 1106–1111, 2007.

[50] K. Nkongchu and G. Santyr, "An improved 3-D Look-Locker imaging method for T1 parameter estimation," *Magnetic Resonance Imaging*, vol. 23, no. 7, pp. 801–807, 2005.

[51] S. A. Hurley, V. L. Yarnykh, K. M. Johnson, A. S. Field, A. L. Alexander, and A. A. Samsonov, "Simultaneous variable flip angle - Actual flip angle imaging method for improved accuracy and precision of three-dimensional T 1 and B 1 measurements," *Magnetic Resonance in Medicine*, vol. 68, no. 1, pp. 54–64, 2012.

[52] N. Weiskopf, A. Lutti, G. Helms, M. Novak, J. Ashburner, and C. Hutton, "Unified segmentation based correction of R1 brain maps for RF transmit field inhomogeneities (UNICORT)," *NeuroImage*, vol. 54, no. 3, pp. 2116–2124, 2011.

[53] S. Deoni and H. Ward, "Rapid T2 estimation with phase-cycled variable nutation steady-state free precession," *Magnetic Resonance in Medicine*, vol. 52, no. 2, p. 435439, 2004.

[54] S. Deoni, "Transverse relaxation time (T2) mapping in the brain with offresonance correction using phase-cycled steadystate free precession imaging," *Journal of Magnetic Resonance Imaging*, vol. 30, no. 2, p. 411417, 2009.

[55] J. D. Jutras, K. Wachowicz, and N. De Zanche, "Analytical corrections of banding artifacts in driven equilibrium single pulse observation of T2 (DESPOT2)," 2016.

[56] O. Bieri, "An analytical description of balanced steady-state free precession with finite radio-frequency excitation," *Magnetic Resonance in Medicine*, vol. 65, no. 2, pp. 422–431, 2011.

[57] O. Bieri and K. Scheffler, "SSFP signal with finite RF pulses," *Magnetic Resonance in Medicine*, vol. 62, no. 5, pp. 1232–1241, 2009.

[58] N. Boulant, "T1 and T2 effects during radio-frequency pulses in spoiled gradient echo sequences," *Journal of Magnetic Resonance*, vol. 197, no. 2, pp. 213–218, 2009.

[59] R. Heule, C. Ganter, and O. Bieri, "Variable flip angle T1 mapping in the human brain with reduced t2 sensitivity using fast radiofrequency-spoiled gra-

dient echo imaging," *Magnetic Resonance in Medicine*, vol. 75, pp. 1413–1422, 4 2016.

[60] a. P. Crawley, M. L. Wood, and R. M. Henkelman, "Elimination of transverse coherences in FLASH MRI.," *Magnetic resonance in medicine : official journal of the Society of Magnetic Resonance in Medicine / Society of Magnetic Resonance in Medicine*, vol. 8, no. 3, pp. 248–260, 1988.

[61] J. D. Trzasko, P. M. Mostardi, S. J. Riederer, A. Manduca, J. D. Trzasko, P. M. Mostardi, S. J. Riederer, A. Manduca, J. D. Trzasko, P. M. Mostardi, S. J. Riederer, and A. Manduca, "Estimating T1 from Multichannel Variable Flip Angle SPGR Sequences," *Magnetic Resonance in Medicine*, vol. 69, no. 6, pp. 1–14, 2014.

[62] M. Bydder, D. J. Larkman, and J. V. Hajnal, "Combination of signals from array coils using image-based estimation of coil sensitivity profiles," *Magnetic Resonance in Medicine*, vol. 47, no. 3, pp. 539–548, 2002.

[63] K. P. Pruessmann, M. Weiger, M. B. Scheidegger, and P. Boesiger, "SENSE: Sensitivity encoding for fast MRI," *Magnetic Resonance in Medicine*, vol. 42, no. 5, pp. 952–962, 1999.

[64] M. A. Griswold, P. M. Jakob, R. M. Heidemann, M. Nittka, V. Jellus, J. Wang, B. Kiefer, and A. Haase, "Generalized Autocalibrating Partially Parallel Acquisitions (GRAPPA)," *Magnetic Resonance in Medicine*, vol. 47, no. 6, pp. 1202–1210, 2002.

[65] O. Brihuega-Moreno, "Optimization of diffusion measurements using Crámer Rao lower bound theory and its application to articular cartilage," *Magnetic Resonance in Medicine*, vol. 50, no. 5, p. 10691076, 2003.

[66] M. Cercignani and D. C. Alexander, "Optimal acquisition schemes for in vivo quantitative magnetization transfer MRI," *Magnetic Resonance in Medicine*, vol. 56, no. 4, pp. 803–810, 2006.

[67] D. Alexander, "A general framework for experiment design in diffusion MRI and its application in measuring direct tissue microstructure features," *Magnetic Resonance in Medicine*, vol. 60, no. 2, p. 439448, 2008.

[68] A. R. Pineda, S. B. Reeder, Z. Wen, and N. J. Pelc, "Cramér-Rao bounds for three-point decomposition of water and fat.," *Magnetic resonance in medicine : official journal of the Society of Magnetic Resonance in Medicine / Society of Magnetic Resonance in Medicine*, vol. 54, pp. 625–35, 9 2005.

[69] P. WH, T. SA, V. WT, and F. BP, *Numerical Recipes in C: the art of scientific computing, second edition*, vol. 2. Cambridge University Press, 1997.

[70] H. Gudbjartsson and S. Patz, "The Rician distribution of noisy MRI data," *Magnetic Resonance in Medicine*, vol. 34, pp. 910–914, 12 1995.

[71] A. Barrau and S. Bonnabel, "A note on the intrinsic Cramer-Rao bound," *Lecture Notes in Computer Science (including subseries Lecture Notes in Artificial Intelligence and Lecture Notes in Bioinformatics)*, vol. 8085 LNCS, pp. 377–386, 2013.

[72] G. J. Stanisz, E. E. Odrobina, J. Pun, M. Escaravage, S. J. Graham, M. J. Bronskill, and R. M. Henkelman, "T1, T2 relaxation and magnetization transfer in tissue at 3T," *Magnetic Resonance in Medicine*, vol. 54, no. 3, pp. 507–512, 2005.

[73] K. Nehrke, "On the steady-state properties of actual flip angle imaging (AFI)," *Magnetic Resonance in Medicine*, vol. 61, pp. 84–92, 1 2009.

[74] M. Jenkinson, C. F. Beckmann, T. E. J. Behrens, M. W. Woolrich, and S. M. Smith, "Fsl," *NeuroImage*, vol. 62, no. 2, pp. 782–790, 2012.

[75] T. C. Wood, "Improved formulas for the two optimum VFA flip-angles," *Magnetic Resonance in Medicine*, vol. 74, no. 1, pp. 1–3, 2015.

[76] S. Deoni, B. Rutt, and D. Jones, "Investigating exchange and multicomponent relaxation in fullybalanced steadystate free precession imaging," *... Magnetic Resonance Imaging*, vol. 27, no. 6, p. 14211429, 2008.

[77] S. C. Deoni and S. H. Kolind, "Investigating the stability of mcDESPOT myelin water fraction values derived using a stochastic region contraction approach," *Magnetic Resonance in Medicine*, vol. 73, pp. 161–169, 1 2015.

[78] J. Zhang, S. H. Kolind, C. Laule, and A. L. Mackay, "Comparison of myelin water fraction from multiecho T2 decay curve and steady-state methods," *Magnetic Resonance in Medicine*, vol. 73, no. 1, pp. 223–232, 2015.

[79] H. J. A. Crooijmans, K. Scheffler, and O. Bieri, "Finite RF pulse correction on DESPOT2," *Magnetic Resonance in Medicine*, vol. 65, no. 3, pp. 858–862, 2011.

[80] N. Gelman, J. M. Gorell, P. B. Barker, R. M. Savage, E. M. Spickler, J. P. Windham, and R. a. Knight, "MR imaging of human brain at 3.0 T: preliminary report on transverse relaxation rates and relation to estimated iron content.," *Radiology*, vol. 210, pp. 759–67, 3 1999.

[81] M. W. Woolrich, S. Jbabdi, B. Patenaude, M. Chappell, S. Makni, T. Behrens, C. Beckmann, M. Jenkinson, and S. M. Smith, "Bayesian analysis of neuroimaging data in FSL.," *NeuroImage*, vol. 45, no. 1 Suppl, pp. S173–S186, 2009.

[82] S. M. Smith, M. Jenkinson, M. W. Woolrich, C. F. Beckmann, T. E. J. Behrens, H. Johansen-Berg, P. R. Bannister, M. De Luca, I. Drobnjak, D. E. Flitney, R. K. Niazy, J. Saunders, J. Vickers, Y. Zhang, N. De Stefano, J. M. Brady, and P. M. Matthews, "Advances in functional and structural MR image analysis and implementation as FSL," *NeuroImage*, vol. 23, no. SUPPL. 1, pp. 208–219, 2004.

[83] S. C. L. Deoni, B. K. Rutt, and D. K. Jones, "Investigating the effect of exchange and multicomponent T1 relaxation on the short repetition time spoiled steady-state signal and the DESPOT1 T1 quantification method," *Journal of Magnetic Resonance Imaging*, vol. 25, no. 3, pp. 570–578, 2007.

[84] A. Lutti and N. Weiskopf, "Optimizing the Accuracy of T1 Mapping Accounting for RF Non-Linearities and Spoiling Characteristics in FLASH Imaging," in *Internation Society for Magnetic Resonance in Medicine*, p. 2478, 2013.

[85] O. Bieri and K. Scheffler, "On the origin of apparent low tissue signals in balanced SSFP," *Magnetic Resonance in Medicine*, vol. 56, pp. 1067–1074, 2006.

[86] O. Bieri and K. Scheffler, "Optimized balanced steady-state free precession magnetization transfer imaging.," *Magnetic resonance in medicine : official journal of the Society of Magnetic Resonance in Medicine / Society of Magnetic Resonance in Medicine*, vol. 58, no. 3, pp. 511–518, 2007.

[87] M. Gloor, K. Scheffler, and O. Bieri, "Quantitative magnetization transfer imaging using balanced SSFP.," *Magnetic Resonance in Medicine*, vol. 60, no. 3, pp. 691–700, 2008.

[88] N. Ben-Eliezer, D. K. Sodickson, and K. T. Block, "Rapid and accurate T2 mapping from multi-spin-echo data using bloch-simulation-based reconstruction," *Magnetic Resonance in Medicine*, vol. 73, no. 2, pp. 809–817, 2015.

[89] D. Ma, V. Gulani, N. Seiberlich, K. Liu, J. L. Sunshine, J. L. Duerk, and M. A. Griswold, "Magnetic resonance fingerprinting," *Nature*, vol. 495, pp. 187–192, 3 2013.

[90] D. Ma, J. Hamilton, Y. Jiang, N. Seiberlich, and M. Griswold, “Fast 3D Magnetic Resonance Fingerprinting (MRF) For Whole Brain Coverage in Less Than 3 Minutes,” in *Internation Society for Magnetic Resonance in Medicine*, 2016.

[91] S. Deoni and B. Rutt, “Gleaning multicomponent T1 and T2 information from steady state imaging data,” *Magnetic Resonance in Medicine*, vol. 60, no. 6, p. 13721387, 2008.

[92] R. M. Henkelman, G. J. Stanisz, and S. J. Graham, “Magnetization transfer in MRI: A review,” *NMR in Biomedicine*, vol. 14, no. 2, pp. 57–64, 2001.

[93] L. Calucci and C. Forte, “Proton longitudinal relaxation coupling in dynamically heterogeneous soft systems,” *Progress in Nuclear Magnetic Resonance Spectroscopy*, vol. 55, no. 4, pp. 296–323, 2009.

[94] R. M. Henkelman, X. Huang, Q.-S. Xiang, G. Stanisz, S. Swanson, and M. Bronskill, “Quantitative interpretation of magnetization transfer,” *Magnetic Resonance in Medicine*, vol. 29, no. 6, pp. 759–766, 1993.

[95] S. J. Graham and R. M. Henkelman, “Understanding pulsed magnetization transfer,” *Journal of Magnetic Resonance Imaging*, vol. 7, no. 5, pp. 903–912, 1997.

[96] C. Morrison and R. Mark Henkelman, “A Model for Magnetization Transfer in Tissues,” *Magnetic Resonance in Medicine*, vol. 33, no. 4, pp. 475–482, 1995.

[97] C. Morrison, G. Stanisz, and R. M. Henkelman, “Modeling magnetization transfer for biological-like systems using a semi-solid pool with a super-Lorentzian lineshape and dipolar reservoir,” 1995.

[98] D. K. Müller, A. Pampel, and H. E. Möller, “Matrix-algebra-based calculations of the time evolution of the binary spin-bath model for magnetization transfer,” *Journal of Magnetic Resonance*, vol. 230, pp. 88–97, 2013.

[99] X. Ou and D. F. Gochberg, “MT effects and T1 quantification in single-slice spoiled gradient echo imaging,” *Magnetic Resonance in Medicine*, vol. 59, no. 4, pp. 835–845, 2008.

[100] S. D. Wolff and R. S. Balaban, “Magnetization transfer contrast (MTC) and tissue water proton relaxation in vivo,” *Magnetic Resonance in Medicine*, vol. 10, no. 1, pp. 135–144, 1989.

[101] M. Gloor, K. Scheffler, and O. Bieri, "Nonbalanced SSFP-based quantitative magnetization transfer imaging," *Magnetic Resonance in Medicine*, vol. 64, no. 1, pp. 149–156, 2010.

[102] Y. Al-Abasse and G. Helms, "Influence of pulse length and shape on variable flip angle T1 mapping of the human brain," in *Internation Society for Magnetic Resonance in Medicine*, 2016.

[103] G. B. Pike, "Pulsed magnetization transfer contrast in gradient echo imaging: a two-pool analytic description of signal response.," *Magnetic Resonance in Medicine*, vol. 36, no. 1, pp. 95–103, 1996.

[104] G. Varma, G. Duhamel, C. De Bazelaire, and D. C. Alsop, "Magnetization transfer from inhomogeneously broadened lines: A potential marker for myelin," *Magnetic Resonance in Medicine*, vol. 73, no. 2, pp. 614–622, 2015.

[105] G. Varma, S. F. Pedersen, M. Taupitz, R. M. Botnar, H. Dahnke, S. F. Keevil, and T. Schaeffter, "Utilizing different methods for visualizing susceptibility from a single multi-gradient echo dataset," *Magnetic Resonance Materials in Physics, Biology and Medicine*, vol. 22, pp. 297–308, 10 2009.

[106] V. H. Prevost, O. M. Girard, S. Mchinda, G. Varma, D. C. Alsop, and G. Duhamel, "Optimization of inhomogeneous magnetization transfer (ihMT) MRI contrast for preclinical studies using dipolar relaxation time (T1D) filtering," *NMR in Biomedicine*, no. October 2016, p. e3706, 2017.

[107] G. Varma, O. M. Girard, V. H. Prevost, A. K. Grant, G. Duhamel, and D. C. Alsop, "In vivo measurement of a new source of contrast, the dipolar relaxation time, T1D, using a modified inhomogeneous magnetization transfer (ihMT) sequence," *Magnetic Resonance in Medicine*, vol. 00, pp. 1–11, 2016.

[108] A. Gupta, T. Stait-Gardner, M. J. Moghaddam, and W. S. Price, "Dipolar relaxation revisited: A complete derivation for the two spin case," *Concepts in Magnetic Resonance Part A: Bridging Education and Research*, vol. 44, pp. 74–113, 3 2015.

[109] G. Varma, O. M. Girard, V. H. Prevost, A. K. Grant, G. Duhamel, and D. C. Alsop, "Interpretation of magnetization transfer from inhomogeneously broadened lines (ihMT) in tissues as a dipolar order effect within motion restricted molecules," *Journal of Magnetic Resonance*, vol. 260, pp. 67–76, 2015.

[110] S. D. Swanson, D. I. Malyarenko, M. L. Fabiilli, R. C. Welsh, J. F. Nielsen, and A. Srinivasan, “Molecular, dynamic, and structural origin of inhomogeneous magnetization transfer in lipid membranes,” *Magnetic Resonance in Medicine*, vol. 77, no. 3, pp. 1318–1328, 2017.

[111] R. Thompson, “Neonatal brain: regional variability of in vivo MR imaging relaxation rates at 3.0 T-initial experience,” *Radiology*, vol. 235, pp. 595–603, 5 2005.